1-1-2000

Low mass stars and the structure of the Pleiades cluster.

Joseph David Adams
University of Massachusetts Amherst

LOW MASS STARS AND THE STRUCTURE OF THE PLEIADES CLUSTER

A Dissertation Presented

by

JOSEPH DAVID ADAMS

Submitted to the Graduate School of the
University of Massachusetts Amherst in partial fulfillment
of the requirements for the degree of

DOCTOR OF PHILOSOPHY

September 2000

Astronomy

LOW MASS STARS AND THE STRUCTURE OF THE PLEIADES CLUSTER

A Dissertation Presented

by

JOSEPH DAVID ADAMS

Approved as to style and content by:

Michael F. Skrutskie, Chair

John R. Stauffer, Member

Martin D. Weinberg, Member

John Kwan, Member

Mark Tuominen, Member

Ronald Snell, Department Head
Astronomy

To Beverly, my loving and loyal wife who always gives the most her heart has to offer under all circumstances.

ACKNOWLEDGMENTS

I would like to thank Mike Skrutskie for his guidance through my graduate school years, especially in the laboratory where his mentoring has made a difference in my approach to electronics and instrumentation. Mike is one of the few who can make lab work seem fun and exciting. I look forward to carrying this experience to my next job as a postdoc at Boston University.

I owe equally much gratitude to John Stauffer, who supervised my Pleiades work during the last two years of graduate school. John always made time for me, even when SWAS and SIRTF things at CfA were crazy, as they were most of the time. I hope that at least some of his careful, conservative approach to doing science has influenced mine.

My collaborators were Chas Beichman at IPAC and Dave Monet at USNO Flagstaff. Chas was a key figure in getting this work started, and spent time reviewing it with me during a visit to UMASS in October, 1999. I owe Dave a debt of gratitude for providing his digitized POSS data not only for the Pleiades, but also for Praesepe. Dave began processing the Pleiades field after being up all night observing, and gave me the processed data a few days later despite the burden of his normal workload.

My thesis committee members, Martin Weinberg, John Kwan, and Mark Tuominen, were approachable, pleasant, and eager to help. Their questions and suggestions were important additions to the original thesis draft.

Dick White independently read a draft for this thesis very carefully, and offered many detailed comments. I enjoyed talking with him about the Pleiades during respites from student questions in Astronomy 224 class.

Classes are often painful for students, but good teachers can alleviate the pain and connect the coursework to a meaningful, larger picture. The many professors with which I had the priviledge to study include David Van Blerkom, Judy Young, Martin Weinberg, John Kwan, Nuria Calvet, Mike Skrutskie, Andy Harris, Steve Schneider, Steve Strom, Ed Chang, Rory Miskimen, and Ed Hartouni.

In addition, Mike Skrutskie, Andy Harris, Mark Heyer, and Steve Schneider all did a fine job serving on my second year project committee and evaluating my work on the effects of the near-infrared airglow on the 2MASS project.

I frequently interrupted many folks around the department for innumerable questions: John Gizis, Meg Thacher, Eric Howard, Sergei Nikolaev, Shashi Kanbur, Jessica Rosenberg, Brooks Rownd, Daisuke Iono, Rafael Millan-Gabet, and probably several others that have eluded my short memory.

I thank Rae Steining for several periods of support working on the 2MASS project, and Roc Cutri at IPAC for always responding to my questions and grabbing the data that I needed to complete this thesis.

The astronomy staff has been very good to me here at UMASS. I would like to thank Terri Grzybowski, Barb Keyworth, Sally Rule, Denise Sallee, Sandy Ostrowski, Jane Knapp, and Ron Zissell for all their help through the years.

Mike Meyer nearly bent over backwards to set up my journal club talk at Steward Observatory while I was passing through Tucson on the way to Kitt Peak. Mike was a gracious host and I found the time spent at Steward to be worthwhile and enjoyable, despite my fear of giving a talk outside the cozy confines of UMASS. I had excellent support at Kitt Peak from Di Harmer and Wendy Shook. I would like to thank Wayne Peters and Ted Groner for their help on Mt. Hopkins at both the 2MASS telescope facility and the 48" scope, although results from the latter run never made it into this thesis.

I thank my parents, Marcia and Dave Adams, for their support through the years and for putting up with what became an irritable son during the completion of this thesis.

This thesis makes use of data products from the Two Micron All Sky Survey, which is a joint project of the University of Massachusetts and the Infrared Processing and Analysis Center, funded by the National Aeronautics and Space Administration and the National Science Foundation. The National Geographic Society-Palomar Observatory Sky Atlas (POSS I) was made by the California Institute of Technology with grants from the National Geographic Society. The Second Palomar Observatory Sky Survey (POSS II) was made by the California Institute of Technology with funds from the National Science Foundation, the National Geographic Society, the Sloan Foundation, the Samuel Oschin Foundation, and the Eastman Kodak Corporation. This research made use of the Digitized Sky Survey. The Digitized Sky Survey was produced at the Space Telescope Science Institute under US government grant NAGW-2166. The images of these surveys are based on photographic data obtained using the Oschin Schmidt Telescope on Palomar Mountain and the UK Schmidt Telescope. The plates were processed into the present compressed digital form with the permission of these institutions.

ABSTRACT

LOW MASS STARS AND THE STRUCTURE OF THE PLEIADES CLUSTER

SEPTEMBER 2000

JOSEPH DAVID ADAMS, B.A., THE COLLEGE OF WILLIAM AND MARY

M.S., SYRACUSE UNIVERSITY

Ph.D., UNIVERSITY OF MASSACHUSETTS AMHERST

Directed by: Professor Michael F. Skrutskie and Dr. John R. Stauffer

This thesis presents a large scale search for new low mass members of the Pleiades cluster using near-infrared photometry from the Two Micron All Sky Survey and proper motions derived from digitized Palomar Observatory Sky Survey photographic plates. The search extends to a 10° radius around the cluster, well beyond the presumed tidal radius, and to a limiting magnitude of $R \sim 20$, corresponding to a lower mass limit of ~ 0.07 $M_{\odot}$ at the distance and age of the Pleiades. Photometric and proper motion selection has identified roughly 1200 probable cluster members, including several hundred new candidates, from nearly 10^6 stars in the field. Multi-object spectroscopy for 528 candidates verifies that the search was extremely effective at detecting cluster stars in the 1 - 0.1 $M_{\odot}$ mass range using the distribution of Hα emission strengths as an estimate of sample contamination by field stars.

When combined with previously identified, higher mass stars, this search provides a sensitive measurement of the stellar mass function and dynamical structure of the Pleiades. The cluster halo is substantially more elongated than expected from standard N body simulation results, although the elongation does lie nearly parallel to

the Galactic plane as a static tidal model predicts. While the high mass stars are clearly centrally concentrated with respect to low mass stars, stars with mass less than ~ 1 $M_{\odot}$ share a similar radial distribution, indicating that they share a similar velocity dispersion. The mass function becomes flat near 0.1 $M_{\odot}$ which implies that objects more massive than those near the hydrogen burning mass limit dominate the total mass. The total stellar mass contains ~ 790 $M_{\odot}$. These results are discussed in the context of past studies of low mass objects in the Pleiades.

TABLE OF CONTENTS

LIST OF TABLES

LIST OF FIGURES

CHAPTER 1

INTRODUCTION

1.1 A Brief Overview of Star Clusters and their Evolution

Star clusters that we observe today share a common age, distance, chemical composition and group velocity, making them valuable objects with which to probe the formation and evolution of stars, the distribution of mass contained in stars, and the structure, kinematics and chemical evolution of the Milky Way and other galaxies. Star clusters also allow the determination of fundamental distances in the universe using either the apparent brightness of the main sequence and giant branches, or individual standard candles such as pulsating variable stars. Thus, they are important objects for astronomical study.

Present star formation in the Milky Way occurs in clouds of molecular gas and is enhanced in the spiral arms by density compression. Evidence suggests that most stars form in clusters (Lada, Strom & Myers 1993) from the fragmented collapse of an initially cold gas cloud in relatively short timescales (eg. Shu 1977; Tereby, Shu & Cassen 1984; Shu, Adams & Lizano 1987). While the physical details of this process are still unclear, the formation of stars and the eventual dissipation of the ambient gas happens in less than $\sim 10^7$ yr. Clusters older than this typically contain little or no ambient gas. As clusters continue to orbit the galaxy in the disk, they dynamically evolve due to internal stellar interactions and external forces from the Galactic gravitational field. Cluster members become unbound gradually due to evaporation or impulsively from a critical interaction with a massive object, such as a giant molecular cloud. Once dispersed, former cluster members freely orbit the

Galaxy within the disk. The dissolution process occurs over a time scale $10^7 - 10^9$ yr depending on richness.

The question of how clusters of stars form and become dissociated from their prenatal gas clouds is beyond the scope of this work. This thesis presents observational constraints on models that describe the evolution of star clusters from a young age to inevitable tidal dispersal using a snapshot analysis of one key template cluster, the Pleiades. First, I will briefly provide the background context relevant to this work in §1.2 and §1.3, review observational progress in this field to date in §1.4, discuss low mass stars as mass tracers in open clusters in §1.5, and then specify a motivation and outline for this thesis in §1.6.

1.2 Theoretical background

A star cluster is a gravitationally bound system of stars. Since stellar radii are typically several orders of magnitude smaller than the average distance between cluster stars, a Newtonian treatment of stars as point masses is usually sufficient except when modelling the cores of dense globular clusters. In recent years computational power has evolved sufficiently to solve Newtonian equations for clusters of a few thousand stars or less, the approximate richness of most open clusters. However, equations of motion for rich globular clusters usually contain a large number of terms and thus must be solved using a mathematical approximation, such as the Fokker-Plank equation.

The most important constraint on open cluster dynamical theories has been the age distribution of open clusters with respect to the age of field stars in the Galactic disk and halo shown in Figure 1.1 (Wielen 1971). Most open clusters are younger than 500 Myr, substantially younger than the age of the Galaxy, while only a few are older than 1 Gyr. From their young ages, we conclude that open clusters are transient objects. They are not isolated systems but are easily dominated by external forces,

most notably the Galactic gravitational field, that contribute to their rapid evolution and dispersal. Open clusters are more confined to the Galactic disk than globular clusters where the effects of the disk tidal force shorten their lifetimes (Murali & Weinberg 1997). Expected cluster lifetimes in the Galactic disk depend on the tidal field, richness, and radius (Wielen 1975).

The relaxation time for a stellar system represents the time scale in which orbits become altered by cumulative encounters among stars, resulting in the loss of the effects of initial conditions. Open clusters have relatively short relaxation times (King 1967)

$$t_{relax} = \frac{N}{31 \ln(N/2)} t_{cr}$$

where t_{cr} is the crossing time for a typical star in a cluster. For $N \approx 1000$ clusters such as the Pleiades, $t_{cr} \sim 10$ Myr and $t_{relax} \sim 5t_{cr}$ or 50 Myr. The relaxation time is comparable to the crossing time for clusters poorer than the Pleiades.

Spitzer & Hart (1971) derive a more precise measure of the relaxtion time, the median relaxation time:

$$t_{rh} = \frac{0.14N}{\ln(0.4N)} \sqrt{\frac{r_h^3}{GM}}$$

or

$$t_{rh} = \frac{6.5 \times 10^8 \text{ yr}}{\ln(0.4N)} \left(\frac{M}{10^5 \text{ M}_\odot}\right)^{\frac{1}{2}} \left(\frac{1 \text{ M}_\odot}{m}\right) \left(\frac{r_h}{1 \text{ pc}}\right)^{\frac{3}{2}}$$

where r_h is the median radius (the radius containg half the total mass), and m is the median stellar mass. For the Pleiades, $M \approx 800$ M$_\odot$, $m \approx 0.4$, and $r_h \approx 5$ pc, the median relaxation time is ~ 25 Myr.

Since open clusters are relaxed systems, they cannot be treated as collisionless systems. In other words, the evolution of open clusters can only be modelled with a time dependent term that includes encounters (King 1980). Mathematically, this means fully solving the Boltzmann equation without invoking a collisionless approximation:

$$\frac{\partial f}{\partial t} + \mathbf{v} \cdot \nabla \mathbf{f} - \nabla \mathbf{\Phi} \cdot \frac{\partial \mathbf{f}}{\partial \mathbf{v}} = \left(\frac{\partial \mathrm{f}}{\partial \mathrm{t}}\right)_{\text{encount}}$$

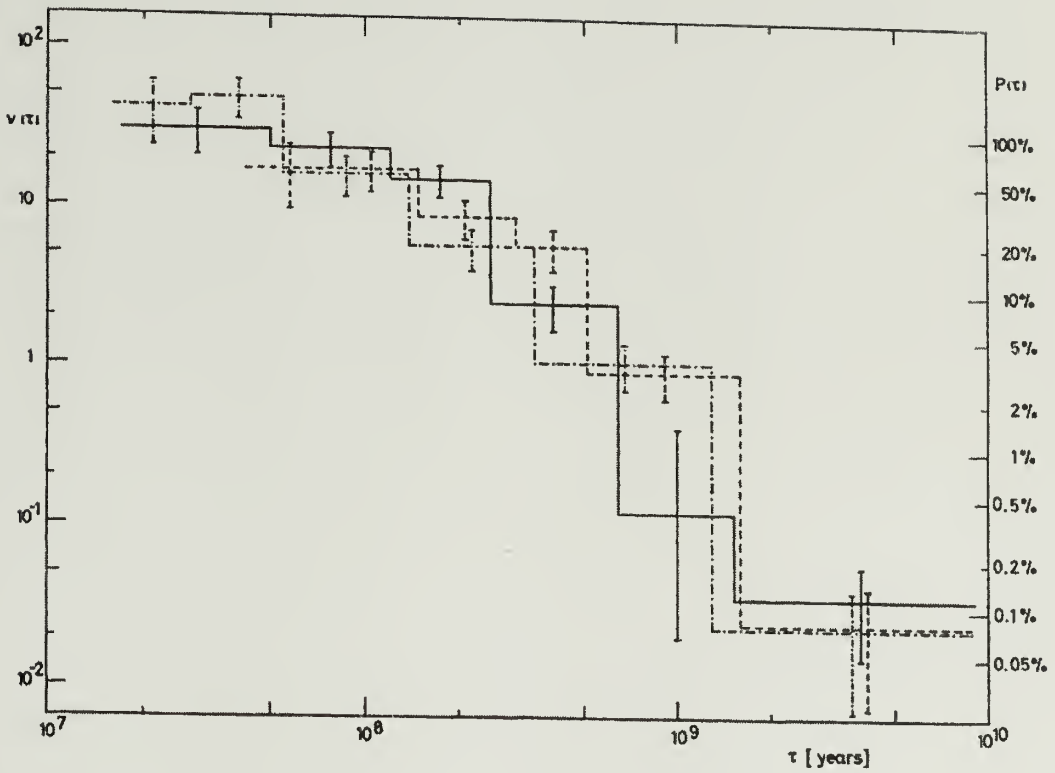

Fig. 1.1.— Age distribution of open star clusters from Wielen (1971). The plot shows the cumulative fraction of observed clusters *vs.* age in years. Data for this plot come from Becker & Fenkhart (1971) (solid); Lindoff (1968) (dot-dashed); and Barbaro, Dallaporta & Fabris (1969) (dashed).

where $f(\mathbf{x}, \mathbf{v})$ is the phase space distribution function in position and velocity and Φ is the potential. Typically, approximation techniques are used to solve this equation.

Encounters and relaxation cause kinetic energy equipartition in star clusters. Evaluation of the diffusion coefficients that describe the change in velocities per time due to large numbers of encounters yield $v^2 \propto m^{-1}$ in equilibrium (Binney & Tremaine 1987). This means that on average more massive stars lose velocity from encounters and preferentially sink to the center of the potential. Lower mass stars aquire higher velocities which correspond to larger, more radial orbits. The result is the development of structure over a relaxation time, where the higher mass stars form a tight core and lower mass stars form an extended halo. The extent of the halo and spatial distribution of escaping stars ultimately depend on the tidal field.

Stars in the halo can aquire enough velocity to escape the cluster entirely, carrying mass, energy, and angular momentum out of the system. Spitzer & Thuan (1972) have shown that the evaporation time is on the order $\sim 100 t_{relax}$ for an isolated cluster. An external tidal field will expedite evaporation by heating the halo stars and by lowering the escape barrier (Spitzer & Chevalier 1973; Mathieu 1985). Evaporation times for $N = 500$ show that collisions with interstellar clouds were only important for clusters with the median radius > 2 pc (not necessarily the most massive clusters). Clusters surviving the longest have a median radius of $\sim 0.5 - 1$ pc Wielen (1975).

The formation and evolution of binary systems can play an important role in cluster evolution. Close, star-star interactions in the core can form binaries and also eject stars out of the cluster at high velocity (Hut & Bahcall 1983). Indeed, this is a favored mechanism to prevent the cluster core from collapsing into a massive central object, especially in dense globular cluster cores. In open clusters, however, gradual evaporation enhanced by the Galactic tidal field plays the major role in dispersal.

1.3 N Body Review

Fortunately, in the past decade or two, computational power has become adequate to directly solve the equations of motion for small N systems such as open clusters without resorting to approximation techniques. The most convenient aspect of this method has been the inclusion of a continuous spectrum of masses in a cluster, which is difficult to theoretically treat in detail (Spitzer & Shull 1975). To computationally simulate a system of stars, the equations that must be solved or approximated numerically are simply the individual Newtonian internal and external forces:

$$F_i = \sum_{i=1, i \neq j}^{N} \frac{G m_i m_j}{r_{ij}^2} + F_{ext,i}$$

To date N body simulations of open clusters in the literature have taken F_{ext} as the force derived from the effective potential of a cluster in circular orbit around the Galactic center with zero orbital inclination. F_{ext} may occasionally contain a term for external objects, such as giant molecular clouds, which would tidally heat a cluster or disrupt it impulsively. Numerous internal factors are typically included in the simulations, such as gravitational softening term to dampen close star-star encounters, an initial mass function, mass loss due to stellar evolution, and a range of cluster richness and total mass.

Aarseth (1999) broadly outlines the advancement of his N body code from NBODY1 to NBODY6. The features of this code contain standard techniques and applications thereof are too numerous to list here, with the important exception of the work of Terlevich (1987) described below and throughout Chapter 6. Wielen (eg. 1975) studied the expected lifetimes of clusters in a static tidal field and with collisions with interstellar clouds. He found good agreement between the lifetime of his $N = 500$ models with theoretical calculations of open cluster lifetimes, as well as the gross effects of mass segregation found in many clusters where the most massive stars are centrally concentrated.

The most comprehensive open cluster N body study to date has been done by Terlevich (1987) using a modified version of Aarseth's NBODY code. Input parameters were typically $N = 250 - 1000$, mean radius $\bar{R} = 2 - 3$ pc, a power law mass function of the form

$$\Psi(m) = m^{-\alpha}$$

where $\Psi(m) = dN/dm$ represents the number of stars in a mass bin $[m, m + dm]$, and $\alpha = 2.35 - 2.75$, similar to the Salpeter value (Salpeter 1955). Average stellar masses were typically $\bar{m} = 0.5$ $M_{\odot}$. Mass loss due to stellar evolution were input as instantaneous events resulting in a 0.7 $M_{\odot}$ white dwarfs or a 1.5 $M_{\odot}$ neutron star depending on the initial stellar mass. Terlevich makes many detailed predictions. Energy equipartition not only produces mass segregation in the core, but appears to continue far into the halo among stars between stars higher and lower than the average stellar mass respectively. The halo becomes flattened due to the tidal field, where the orbits become elongated and more radial parallel to the Galactic plane, especially in the direction of the Galactic center. This flattening is depicted in Figure 1.2. Aarseth (1973) has computed the effective ellipticity of the flattening to be 2:1.4:1 in the X:Y:Z directions respectively where X increases away from the Galactic center, Y increases along the direction of cluster revolution around the Galaxy, and Z increases above the Galactic disk. Terlevich finds that stars escape at small angles to the Galactic plane. Stars can be trapped between 1 – 2 tidal radii for some period of time before escaping through the Lagrangian points on the equipotential surface. For rich, $N = 1000$ clusters, the depletion rates show preferential escape of stars below average mass, which may flatten the observed luminosty function at the faint end.

The escape mechanism and distribution of escapers in the static tidal model has been analyzed in detail by Portegies Zwart (eg. 2000) using N body simulations. Nearly all stars escape through the Lagrangian points along the $\pm X$ directions with a well-defined velocity distribution that depends on dynamical age. As in the Terlevich

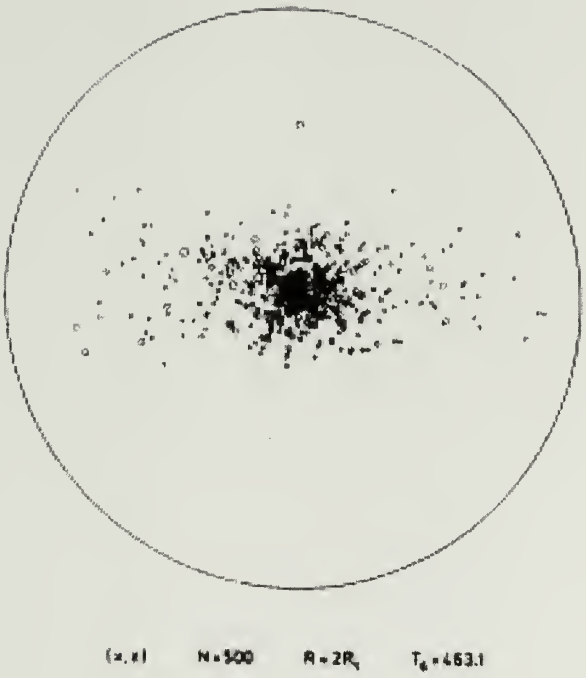

Fig. 1.2.— Tidal flattening in the XZ plane for a $N = 500$ cluster in mid-life from Terlevich (1987). The field size is 2 tidal radii.

models, escaping stars stay confined to the Galactic plane throughout the cluster lifetime. This a direct consequence of a zero inclination, circular cluster orbit in the disk. Portegies Zwart has also introduced effects of detailed stellar evolution and close stellar encounters, including velocity kicks for neutron star formation, star-star tidal interactions, and general relativistic effects. Neutron stars escape with high velocity early in a cluster's life. Mass loss from stellar evolution can shorten cluster lifetime. In general these results agree with the work of Terlevich, which should be expected since her models use a similar tidal field.

N body theorists have not yet modified the tidal field for open clusters to include vertical oscillations through the Galactic disk and radial variations due to orbit eccentricity, as in the case of globular clusters (Murali & Weinberg 1997; Combes, Leon & Maylan 1999). In the Pleiades, a time dependent tidal field would be more accurate than the static tidal field since the cluster is located 50 pc below the Galactic plane and contains a vertical space velocity away from the plane of a few km/s (Robichon et al. 1999).

Other recent numerical work has focused on the effects of the initial mass function and the role of binary formation and evolution. de la Fuente Marcos (1995; 1996a; 1996b) studied the effects of different mass functions on cluster lifetimes using power law mass functions with exponent α ranging from 1.3 to 2.35 and Miller-Scalo (Miller & Scalo 1979) log-normal mass functions. Poor clusters ($N = 100$) were affected by the initial mass function in the sense that the steeper mass functions resulted in more rapid evolution due to the short time needed to develop a halo and for evaporation to occur. The evolution of rich clusters ($N = 750$) were less dependent on the inital mass function and could be described in one model with three stages: the formation of the halo; the escape of halo stars due to close encounters at pericenter; and evaporation due to cumulative distant encounters. Mass loss due to stellar evolution will slow down the evolution with a dependence on the initial mass function,

particularly in the Salpeter power law case. Kroupa (1995) studied the evolution of $N = 400$ clusters containing single stars and binaries. The results clearly indicated that mass segregation increases throughout the lifetime of cluster but more slowly if many systems are binaries rather than single stars.

1.4 Observational progress

Some dynamical structure has been found in open clusters. For example, mass segregation between the highest mass stars and low mass stars is well established in clusters. Proper motion work has found evidence for mass segregation in several clusters such as the Pleiades (van Leeuwen 1983), the Hyades (Pels, Oort & Pels-Kluyver 1975; Reid 1992), and and Praesepe (Hambly et al. 1995). M67 shows mass segregation and a luminosity function depleted of faint stars from evaporated members (Prata 1971; Montgomery, Marschall & Janes 1993). M11 also shows detailed mass segregation structure (Mathieu 1984). Interestingly, Hillenbrand & Hartmann (1998) claim to have found mass segregation in the Trapezium cluster, a cluster too young to have dynamically evolved, raising the possibility that high mass stars form in, rather than dynamically migrate to, the center (Bonnell & Davies 1998). Any difference in radial distribution between average and below average mass stars has not been published at the time of this work.

In general both theoretical and numerical work has agreed well with the expected lifetimes of open clusters inferred from Figure 1.1. However, the details of cluster evolution presented by eg. Terlevich (1987) have not been extensively tested by observations. Since the tidal field is responsible for determining the outer structure of cluster halos as well as the detailed escape mechanism, observations of cluster halos would illuminate the whether or not clusters dissolve into the Galactic disk in the manner predicted by the static tidal model. Unfortunately, there are few observations and little agreement regarding the structure of cluster halos. Oort (1979) and

Perryman et al. (1998) have found some evidence for a flattened or prolate structure to the Hyades; van Leeuwen (1983) and Raboud & Mermilliod (1998a) have detected a small degree of flattening at the center of the Pleiades using high and intermediate mass stars; Prosser (1992) claims to have detected substantial flattening in Alpha Persei. On the other hand, M67 and Praesepe show little or no flattening (Mathieu 1983; Raboud & Mermilliod 1998b). This could mean that our understanding of the tidal field is inadequate or that environmental effects play a significant role in shaping the halo. In the latter case, clusters of age $\sim$ 100 Myr or younger would serve as better laboratories for studying the effects of the tidal field. Since halo flattening is intricately related to escape rates, further mapping of halos could identify escape mechanisms in open clusters.

An additional observational impediment to understanding open cluster dynamics is their relatively small internal velocity dispersion, $\sim$ 1 km s^{-1} or less. Even the largest telescopes currently available can barely detect a radial velocity this small for faint stars. Jones (1970; 1971) used high precision proper motions to measure velocity distributions for a small number of stars in the Pleiades and Praesepe, and found the velocity dispersions to agree with virial expectations. Good data for internal velocities will become available during the upcoming generation of astrometry satellites that will reach microarcsecond precision.

1.5 Low Mass Stars: Dynamical Tracers in Open Clusters

Since low mass stars dominate the mass function and dynamical mass of star clusters, our success in testing theory with observations relies on our ability to detect them and determine their masses. Here I briefly discuss their properties as astronomical objects.

Low mass stars have characteristic spectral types late K and M, masses $\sim$ 1 – 0.08 $M_\odot$, and effective temperatures of $\sim$ 5000 – 2800 K depending on particular

mass and age. Due to their cool temperatures, the atmospheres of low mass stars allow the condensation of molecules and dust grains. Spectral features of M dwarfs include TiO, CaH, CaOH, and VO in the optical and H_2 and H_2O in the infrared. These molecules prohibit a strict blackbody approximation to the spectral energy distribution in the optical and infrared regime, and re-distribute the luminosity so that even broad band colors appear unlike those of a blackbody. For example, a star of effective temperature 3000 K will have a spectral energy distribution with a luminosity deficit in the near-infrared due to H_2 collision induced absorption and a peak shortward of 1 μm with a luminosity excess at optical wavelengths (Saumon et al. 1994). For early to intermediate type M dwarfs, this backwarming effect increases at cooler temperatures thus shifting near-infrared colors blueward of blackbody colors.

The interiors of low mass stars are highly convective and fully convective for stars below $\sim$ 0.4 $M_\odot$. The equations of state for interiors typically uses both temperature and pressure ionization for hydrogen and helium. The condensation of molecules make accurate model atmosphere opacities difficult to construct. Recent models include Chabrier & Baraffe (1997); Baraffe et al. (1997, 1998); and Burrows et al. (1997). Current model atmospheres contain non-grey opacities, dust grain absorption, and updated line lists for TiO and H_2O and other important molecules. Effective temperatures, surface gravities, and luminosties have been computed over a variety of metallicities and ages. Transformation onto the observational plane via filter convolution over standard passbands is performed during the modelling.

Low mass stellar models have been extended into the brown dwarf regime. Brown dwarfs differ from stars in several important regards as reviewed by Oppenheimer, Kulkarni & Stauffer (1999). Although brown dwarfs and stars share a similar cloud collapse formation mechanism, stars are massive enough to sustain fusion temperatures in their cores, providing a long term source of luminosity. Stars cool slightly as they age but soon reach a stable temperature and luminosity that persists during

the main sequence lifetime. Objects below the hydrogen burning mass limit, about 0.075 $M_{\odot}$, undergo transient hydrogen or deuterium burning, but otherwise radiatively cool yielding a luminosity that is age dependent. Cooling curves (Burrows et al. 1997) predict a decline in luminosity by several orders of magnitude during the first Gyr. The interiors of brown dwarfs are supported by electron degeneracy pressure which leads to a small variation in radius with mass. The spectra of "warm" brown dwarf atmospheres ($T \sim 1300 - 2500$ K) are characterized by metallic hydride (CrH, FeH, CaH) and atomic alkali lines (Li, Na, K, Rb, Cs) (Kirkpatrick et al. 1999). In cooler brown dwarfs ($T \sim 900 - 1300$ K), dust grains rain out and CH_4 condenses as a major opacity source in the optical and near-infrared (Burgasser et al. 1999; Burrows & Sharp 1999).

The models of low mass stars allow a conversion of observed luminosity to mass. Stars in an open cluster presumably have similar age, lie at similar distance, and have similar metallicity. Thus, open clusters represent an ideal laboratory for testing models of low mass stars. Mass-luminosity relations are best determined using dynamical masses measured in binary orbits. However, luminosity is age dependent and low mass binary systems can be studied in detail only in very nearby multiple systems which are likely to be older than most open clusters. With proper calibration, stellar models can be used to infer approximate masses for cluster stars without having to detect and monitor binary systems.

The mass function is fundamentally interesting in astronomy because it determines the total mass contained in stars and identifies which stars are dynamically important. For example, it is well known that the velocities of stars trace a large amount of dark matter in disks and halos of galaxies. The stellar mass function is an estimate of the contribution of stellar matter to the Galactic mass budget. Low mass stars are intrinsically faint and their overall abundance determined by the mass function may constitute some fraction of the dark matter. Since stars form in clusters, open clusters

offer a chance to study the initial mass function, or the inherent distribution of mass in stellar systems. Furthermore, due to their large numbers and susceptibility to form a halo, low mass stars trace the phase space structure and dynamical age of clusters.

The mass function in the field and in clusters is still poorly determined at low mass. Bouvier et al. (1998) claimed to find a rising mass function in the Pleiades with slope $\alpha = 0.6$ in the range 0.3 – 0.06 $M_\odot$, while Hillenbrand & Carpenter (2000) assert a turnover in the mass function at 0.15 $M_\odot$ using observations in the Trapezium cluster. Using nearby stars, Reid & Gizis (1997) estimates $\alpha \approx 1$, while Gould, Bahcall & Flynn (1997) claims to detect a break in the power law exponent at 0.6 $M_\odot$ from Salpeter ($\alpha = 2.35$) to $\alpha = 0.6$ down to the hydrogen burning mass limit (~ 0.08 $M_\odot$).

1.6 Purpose and Scope of this Work

The dispersal of open clusters into the Galactic disk has been modelled. Although the models can generally reproduce the expected lifetimes of clusters, a lack of observations prevents a detailed study of the *process* of their dissolution. Which mass groups are segregated? What is the structure of the cluster halos? Are they tidally deformed? Is the mass function still rising at low mass? Does is resemble the mass function in the field? Which stars are dynamically important? How do stars escape? Which mass groups are most likely to escape?

Addressing these questions has traditionally been difficult due to the scarcity of observations in the outer parts of clusters where critical dynamics occur. Few or no low mass stars have been studied in the outer parts of the halos. Firm observational determination of the structure of open clusters is stymied by the diffuse surface density of low mass cluster stars projected onto the much richer density of Galactic stars. The intrinsic faintness of low mass stars allows their detection and detailed study only in clusters with distances less than a few hundred parsecs, which occupy a large area on

the sky and are thus difficult to fully study. Previous observations of faint stars in clusters typically have covered only the cores.

Modern digital sky surveys offer an opportunity to contribute to the dearth of observable properties of open cluster structure. Photometric and astrometric information from digital sky surveys can detect faint cluster members uniformly over large areas of sky. With a reliable sample of cluster members, the halo structure and mass function can be studied in much more detail than in the past. Specifically, this thesis uses data from current sky surveys to address the above issues using a well-known cluster, the Pleiades.

The best approach begins with a study of a key cluster such as the Pleiades to assess the feasibility of extracting cluster members over large regions of sky. This work will use the Pleiades cluster as a laboratory for demonstrating the feasibility of using the current wealth of photometric and astrometric data for studying the dynamical properties of suitable open clusters. I chose to study the Pleiades because (1) its low mass constituents are bright enough to be detectable due to their youth and proximity; (2) it has a relatively large proper motion being located roughly perpendicular to the sun's orbital motion; (3) it lies at intermediate Galactic latitude in terms of field star surface density; and (4) previous faint proper motion searches have been successful over small regions of sky (eg. Hambly, Hawkins, & Jameson 1993). The structure of the Pleiades will constrain the dynamical models mentioned in this chapter.

The outline for this dissertation is sketched as follows. Chapter 2, presents the technique for measuring cluster membership probabilities for stars with proper motions, including Monte Carlo simulations of realistic data sets to assess the feasibility of extracting cluster members from data that consists primarily of field stars. Chapter 3 briefly summarizes the primary source of sky survey data used in this research, namely the Two Micron All Sky Survey (2MASS) and the photographic Palomar Observatory Sky Surveys, POSS I and POSS II which have been scanned and digitized

at the U. S. Naval Observatory. In Chapter 4 presents the results of a photometric and proper motion search for low mass stars in the Pleiades; a spectroscopic study of several hundred Pleiades candidates is presented separately in Chapter 5. The spectroscopic study contains discussions on cluster membership and chromospheric, surface gravity, and near-infrared photometric properties of low mass stars in the Pleiades using a sample of highly probable members. The results discussed in Chapters 4 and 5 are the basis for the culmination of this work, a discussion of the mass distribution and and structure of the Pleiades in the context of published theoretical predictions and previous studies (Chapter 6). The radial distribution of low mass stars, the cluster mass function and inferred total mass including a correction for binary systems, and halo structure are addressed in detail. Chapter 7 summarizes this research and previews future observations that will contribute substantially to this field.

CHAPTER 2

METHOD

2.1 Introduction

This chapter describes the technical methods used in this thesis research to identify cluster members in the sky as determining cluster membership is the first step towards accomplishing the science goals outlined in Chapter 1. §2.2 describes basic astronomical measurements relevant to this work, such as photometry, stellar colors, and proper motion. §2.3 outlines the method employed to select cluster candidates based on their proper motion distribution. §2.4 presents the results of Monte Carlo simulations of the method used to extract sources in a hypothetical nearby cluster. The simulations are intended to assess the numerical error of the method and the distortion of statistical parameters as a function of field characteristics, namely field star surface density. §2.5 summarizes the conclusions of this chapter.

2.2 Fundamentals

Astronomical surveys are a powerful tool for studying nearby open clusters because they quickly and efficiently cover large areas of sky. The surveys used in this work employ broadband photometry. This allows a quick, strong detection of faint sources over large areas of sky using one or more small, relatively inexpensive telescopes. Broadband photometry aims to measure the apparent brightness of a source by integrating its flux over a wavelength or frequency interval. Stellar flux in a given wavelength or frequency interval is defined as the quantity of energy received from the star per unit collecting area per unit time; each photon of frequency ν carries

an energy $E = h\nu$ where h is the Planck constant. The common linear units of measurement for flux density are ergs s^{-1} cm^{-2} Hz^{-1}. In photometry, observers more commonly use logarithmic units embodied in the magnitude system. The apparent magnitude of a star in a wavelength band with central wavelength λ_0, m_λ, is a dimensionless quantity which depends on the flux F_0 of a standard reference star at λ with a defined magnitude $M_{\lambda,0}$, or zero point:

$$m_\lambda - M_{\lambda,0} = -2.5\log\left(\frac{\mathrm{f_{star,\lambda}}}{\mathrm{F_{0,\lambda}}}\right) \tag{2.1}$$

Some common broadband filters used in optical-infrared photometry are given in Table 2.1; the central wavelengths λ_0 are approximate as they vary with filter system and the filter widths are roughly on the order of ~ 0.1 μm, the longer wavelength filters being slightly wider. These wavelengths together typically cover the bulk of the spectral energy distributions emitted by most stars assuming a simple blackbody approximation at typical stellar temperatures.

Table 2.1: Standard filter passbands with approximate central wavelengths λ_0 (Budding 1993; Mihalas & Binney 1981).

	U	B	V	R	I	J	H	K
λ_0 (μm)	0.35	0.44	0.55	0.69	0.88	1.2	1.6	2.2

Most sky surveys are taken through at least two filters for the purposes of deriving a first-order measurement of spectral type. The blackbody approximation to stellar flux yields a mathematically unique ratio of fluxes at two given wavelengths for a given effective temperature. Therefore, a measurement of flux at two or more different wavelengths, or "color index," provides a means of estimating effective temperature. Observationally, stellar color indices are defined as a flux ratio or magnitude difference at two wavelengths $\lambda 1$ and $\lambda 2$:

$$m_{\lambda 1} - m_{\lambda 2} = -2.5\log\left(\frac{\mathrm{f_{\lambda 1}}}{\mathrm{f_{\lambda 2}}}\right) \tag{2.2}$$

Usually the "sign" of the color is such that a larger color value indicates a "redder" color, or relatively more flux emitted at the longer wavelength. The main sequence for a cluster shows a distinct location in color-magnitude space. This property allows an initial selection of cluster candidates based on their expected apparent magnitude and color.

The apparent magnitude of a star says nothing about its distance unless we known its intrinsic luminosity based on its spectral energy distribution, absorption line broadening, color, or other temperature-dependent measurement. It is useful to employ a quantity which yields a distance – magnitude relation. In the absence of general relativistic effects (more than a good approximation for the local portion of the Galaxy!) stellar flux decreases as d^{-2}, thus the distance modulus is

$$m - M_0 = 5\log d_{\rm pc} - 5 \tag{2.3}$$

where m is the apparent magnitude, $d_{\rm pc}$ is the distance in parsecs, and M_0 is the absolute magnitude, or apparent magnitude at $d_{pc} = 10$.

Reliably positioned telescopes equipped with CCD detectors (or in the past, photographic plates), can measure the positions of stars very accurately. The space motion of the Sun and its neighbors in orbit around the galaxy can induce a measurable shift in the position of a star over time compared to the more distant, "fixed" stars used as a reference grid. Proper motion is defined as this apparent shift in position on the plane of the sky, and is usually measured in units of angular distance per time, such as "/century or mas/year. The proper motion vector consists of two components corresponding to angular speed and direction, often expressed in angular motion along each right ascension direction α and declination direction δ.

The internal velocity dispersion of stars in typical open clusters is usually less than $\sim$ 1 km/s (eg. Jones 1970). Since this is much smaller than the differential motion between the Sun and the cluster, members of a cluster share similar proper motion and a common "convergent point" or projected point on the sky to which the

cluster appears to be moving based on the proper motion of its members. The internal motions, distance, relative velocity, and convergent point of a cluster determine the overall dispersion in proper motion of its members. With the exception of the Hyades, the proper motion dispersion in an open cluster is usually much smaller than the cluster's mean motion and thus is difficult to measure. Table 2.2 lists a few open clusters with mean proper motions derived from bright star measurements with the *Hipparcos* satellite. Ground-based proper motions can detect all these clusters, but the Pleiades and Praesepe are the easiest ones to detect due to their intermediate latitiudes. IC 2391 and IC 2602 are the most difficult to study due to their proximity to the Galactic plane and a shorter time baseline in the southern hemisphere, spanning only from 1980 to the present.

Table 2.2: *HIPPARCOS* proper motions for some clusters within 300 pc (Robichon et al. 1999).

Cluster	$\mu_{\alpha \cos \delta}$ (mas/yr)	μ_{δ} (mas/yr)
Coma Ber	-11.38 ± 0.23	-9.05 ± 0.12
Pleiades	19.15 ± 0.23	-45.72 ± 0.18
IC 2391	-25.06 ± 0.25	22.73 ± 0.22
IC 2602	-17.31 ± 0.16	11.05 ± 0.15
Praesepe	-36.24 ± 0.35	-12.88 ± 0.24
Alpha Per	22.93 ± 0.15	-25.56 ± 0.17
Blanco 1	19.15 ± 0.50	3.21 ± 0.27

2.3 Extracting cluster members in proper motion space

2.3.1 Introduction

This section describes the statistical technique used in this thesis research for modelling data in proper motion space and deriving rigorous cluster membership probabilities for individual stars.

2.3.2 The distribution function

For the clusters presented in 2.2, measurement error dominates the proper motion dispersion. An excellent technique to model the cluster error and field distribution was presented by Sanders (1971). The technique can easily be adapted and modified to suit the particular characteristics of each cluster. For a suitable number of stars, the distribution of proper motion measurements for the field stars can be adequately modelled with a distribution function Φ_f, and the cluster stars can be modelled with a separate distribution function Φ_c. The best forms for Φ_f and Φ_c are empircally determined. Φ_c is usually of the form

$$\Phi_c = \frac{N_c}{2\pi\sigma_{x,c}\sigma_{y,c}} \exp\left\{-\frac{1}{2}\left[\left(\frac{\mu_x - \bar{\mu}_{x,c}}{\sigma_{x,c}}\right)^2 + \left(\frac{\mu_y - \bar{\mu}_{y,c}}{\sigma_{y,c}}\right)^2\right]\right\} \tag{2.4}$$

where N_c is the number of cluster stars, $\sigma_{x,c}$ and $\sigma_{y,c}$ represent the dispersions in the x- and y-directions respectively, and the bracketed quantities the mean motion in those directions. Here the x-direction refers to the direction along the vector of the cluster's mean motion; the y-direction lies orthogonal to x.

The field distribution function may be analogous to equation 2.4 but for clusters with large proper motion is more appropriately described with an exponential term in the x-direction referenced at point μ_1 (Jones & Stauffer 1991):

$$\Phi_f = \frac{N_f C_0}{\sqrt{2\pi}\sigma_{y,f}} \exp\left\{-\left[\frac{\mu_x - \mu_1}{\tau} + \frac{1}{2}\left(\frac{\mu_y - \bar{\mu}_{y,f}}{\sigma_{y,f}}\right)^2\right]\right\} \tag{2.5}$$

where N_f is the number of field stars. The empirical justification for this form will become apparent in §4.3. In order to determine the normalization constant C_0 one must integrate the μ_x component of Φ_f over appropriately chosen limits μ_1 and μ_2:

$$\int_{\mu_1}^{\mu_2} C_0 \exp\left\{\frac{-(\mu_x - \mu_1)}{\tau}\right\} d\mu_x = 1 \tag{2.6}$$

yielding

$$C_0 = \frac{1}{\tau\left[1 - e^{\frac{-(\mu_2 - \mu_1)}{\tau}}\right]} \tag{2.7}$$

where μ_1 and μ_2 represent suitable limits that straddle the cluster distribution in μ_x.

2.3.3 Membership probability

Based on reliable distribution functions, the probability of cluster membership for an individual star with proper motion μ_x and μ_y is

$$p = \frac{\Phi_c}{\Phi} \tag{2.8}$$

where $\Phi = \Phi_c + \Phi_f$. A spatial distribution parameter could be included to account for the exponential drop in surface density with radial distance (Jones & Stauffer 1991). However, a primary goal of this thesis is to derive an unbiased measurement of open cluster radial structure. Thus, this work will utilize a distribution function that depends only on proper motion.

2.3.4 Fitting the distribution function to a data set: a maximum likelihood application

Before calculating p for each star in a data set, the parameters of the distributions in eqs. 2.4 and 2.5 must be determined. Here I follow the maximum likelihood technique presented by Sanders (1971). A parameter u_j in a set of M parameters is best fit by N data samples when the log distribution function is minimized:

$$\sum_{i=1}^{N} \frac{\partial \ln \Phi(\mu_x^i, \mu_y^i)}{\partial u_j} = 0, j = 1, 2, 3, ..., M \tag{2.9}$$

In the case of distribution functions 2.4 and 2.5, I must solve 8 equations for the parameters $N_f, \bar{\mu}_{y,f}, \bar{\mu}_{x,c}, \bar{\mu}_{y,c}, \tau, \sigma_{y,f}, \sigma_{x,c}$, and $\sigma_{y,c}$. The total number of stars is $N = N_f + N_c$. To simplify, I define the following:

$$\alpha \equiv \exp\left\{-\left[\frac{\mu_x^i - \mu_1}{\tau} + \frac{1}{2}\left(\frac{\mu_y^i - \bar{\mu}_{y,f}}{\sigma_{y,f}}\right)^2\right]\right\} \tag{2.10}$$

$$\beta \equiv \exp\left\{-\frac{1}{2}\left[\left(\frac{\mu_x^i - \bar{\mu}_{x,c}}{\sigma_{x,c}}\right)^2 + \left(\frac{\mu_y^i - \bar{\mu}_{y,c}}{\sigma_{y,c}}\right)^2\right]\right\} \tag{2.11}$$

$$\gamma \equiv 1 - e^{\frac{-(\mu_2 - \mu_1)}{\tau}} \tag{2.12}$$

so the equation set becomes

$$N_f: \quad \sum_{i=1}^{N} \frac{1}{\Phi}\left[\frac{\alpha}{\sqrt{2\pi}\sigma_{y,f}\tau\gamma} - \frac{\beta}{2\pi\sigma_{x,c}\sigma_{y,c}}\right] = 0 \tag{2.13}$$

$$\bar{\mu}_{y,f}: \quad \sum_{i=1}^{N} \frac{\alpha}{\Phi}(\mu_x^i - \bar{\mu}_{y,f}) = 0 \tag{2.14}$$

$$\bar{\mu}_{x,c}: \quad \sum_{i=1}^{N} \frac{\beta}{\Phi}(\mu_x^i - \bar{\mu}_{x,c}) = 0 \tag{2.15}$$

$$\bar{\mu}_{y,c}: \quad \sum_{i=1}^{N} \frac{\beta}{\Phi}(\mu_y^i - \bar{\mu}_{y,c}) = 0 \tag{2.16}$$

$$\sigma_{y,f}: \quad \sum_{i=1}^{N} \frac{\alpha}{\Phi}\left[\left(\frac{\mu_y^i - \bar{\mu}_{y,f}}{\sigma_{y,f}}\right)^2 - 1\right] = 0 \tag{2.17}$$

$$\tau: \quad \sum_{i=1}^{N} \frac{\alpha}{\Phi}\left[\frac{\mu_x^i - \mu_1}{\tau} + \frac{(\mu_2 - \mu_1)(1-\gamma)}{\tau\gamma} - 1\right] = 0 \tag{2.18}$$

$$\sigma_{x,c}: \quad \sum_{i=1}^{N} \frac{\beta}{\Phi}\left[\left(\frac{\mu_x^i - \mu_{x,c}}{\sigma_{x,c}}\right)^2 - 1\right] = 0 \tag{2.19}$$

$$\sigma_{y,c}: \quad \sum_{i=1}^{N} \frac{\beta}{\Phi}\left[\left(\frac{\mu_y^i - \mu_{y,c}}{\sigma_{y,c}}\right)^2 - 1\right] = 0 \tag{2.20}$$

The equations are readily soluble numerically by iteration. First, a reasonable guess to the parameter values was inserted into the equations. For each equation, the relevant parameter was varied while holding the others constant until the equation was best satisifed. A bisection routine similar to the one found in Press et al. (1992) (hereafter *Numerical Recipes*) was used to find N_f in eq. 2.13 while for the others a local minimum was found over a grid of reasonable values for each parameter. The procedure was continually iterated over the entire set of equations until the parameter values converged to a steady value. Convergence after several iterations typically took less than a few minutes on a 150 MHz Pentium PC for a sample of several thousand stars. The final, best fit parameters were then inserted into eq. 2.8 to determine the membership probability for each star based on its μ_x and μ_y.

2.4 Validation: Monte Carlo simulations

2.4.1 Introduction

This section describes a numerical experiment using the methods outlined in the previous section. The experiment consists of repeated Monte Carlo simulations of a hypothetical proper motion data set for a cluster sample and field background. The purpose of the experiment is threefold. First, the simulations will globally validate the method by using it to recover the parameters of a known distribution. Second, repeated simulations can quantify any numerical error or bias introduced by the method. Finally, the simulations determine the effects of varying field star densities on the resulting sample of membership probabilties.

Monte Carlo simulations are used in a wide variety of physical problems and have become a standard computational tool during the past several decades. In such a simulation, one attempts to create artificial data sets which represent a well-defined distribution function. The distribution functions are used to determine statistical deviates (used as "data points") from an original random value of uniform probability. Such a tool allows one to compute the distribution of parameter values and thus the error of a fitted parameter with respect to the "true" value of the parameter. The confidence of fitted parameters from a real data set can then be determined.

2.4.2 Description of Simulations

In the context of this experiment, the strategy is to use the Monte Carlo method to generate artifical fields and clusters based on proper motion distribution functions with known parameters. The "true" parameters are assigned realistic values, ones close to those fitted from a real data set. Based on procedures in *Numerical Recipies* two random numbers rn_1 and rn_2 in the uniformly probable range [0,1] were converted into gaussian deviates y_1 and y_2 for the gaussian components in eqs. 2.4 and 2.5:

$$y_1 = \sqrt{-2 \ln rn_1} \cos 2\pi rn_2 \tag{2.21}$$

$$y_2 = \sqrt{-2 \ln rn_1} \sin 2\pi rn_2 \tag{2.22}$$

or an exponential deviate for the field x-direction case:

$$\mu_x = -\tau \log rn + \mu_1 \tag{2.23}$$

The trigonometric functions in eqs. 2.21 and 2.21 were replaced by choosing random coordinates v_1 and v_2 within the unit circle such that $R^2 = v_1^2 + v_2^2$ is a uniform deviate. The gaussian deviates were then calculated using the expressions $v_1\sqrt{-2 \ln R^2/R^2}$ and $v_2\sqrt{-2 \ln R^2/R^2}$ for y_1 and y_2 respectively.

The values assigned to the distribution function parameters are given in Table 2.3. The proper motion vectors have been rotated and translated such that the cluster mean motion lies at (0,0) "/century in the $\mu_x - \mu_y$ plane and the peak of the field distribution lies near (-4.5,0) "/century. In addition to the x-direction limits μ_1 and μ_2 I imposed limits in the y-direction of (-2.5,2.5) "/century to effectively create a box in the $\mu_x - \mu_y$ plane which excluded all outside data points. Figure 2.1 shows a proper motion vector point diagram (VPD) for an example artificial field containing 2500 stars with $f = 0.8$ where $f = N_f/(N_f + N_c)$ is the fraction of field stars in the sample. Figure 2.2 illustrates that the resulting data set does represent the superposition of the original distribution functions.

The simulations used three different values $f = 0.5, 0.8, 0.9$, corresponding to $N_f = 500, 2000, 4500$ superimposed on a "cluster" of $N_c = 500$ stars. For each f, the simulation was run 100 times each time using a different seed in the random number generator. Each simulation generates an artificial cluster and field sample, which is then considered to be a data set by the maximum likelihood estimator embodied in eqs. 2.13-2.20 to recover the distribution function parameters and assign membership probabilities to each star in the data set. The results will illustrate the dispersion of parameter values to the original values used to generate the "data," study the

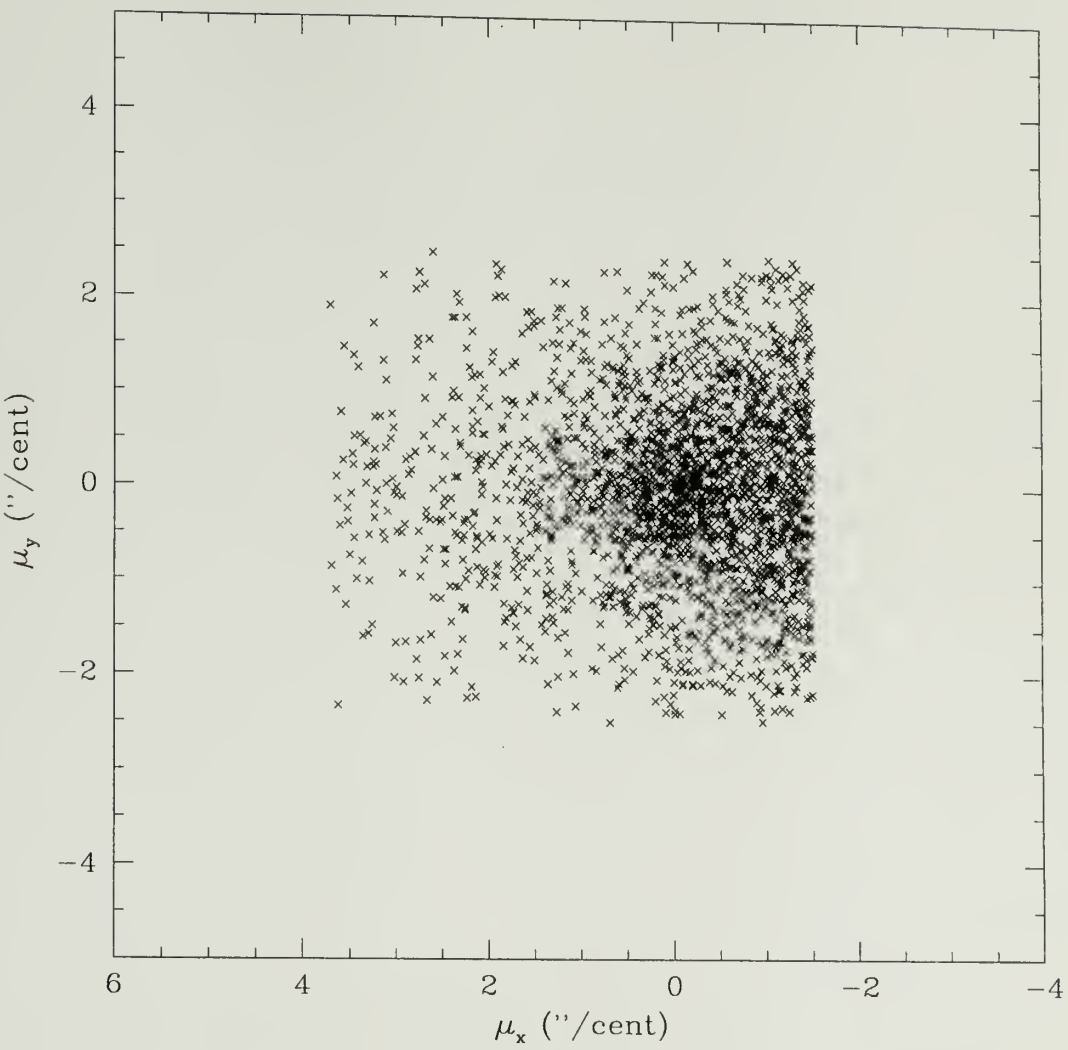

Fig. 2.1.— VPD for a simulated cluster of $N_c = 500$ and $N_f = 2000$ generated from the parameters listed in Table 2.3. The cluster is clearly visible near (0,0) "/century, as well as the tail of the field distribution.

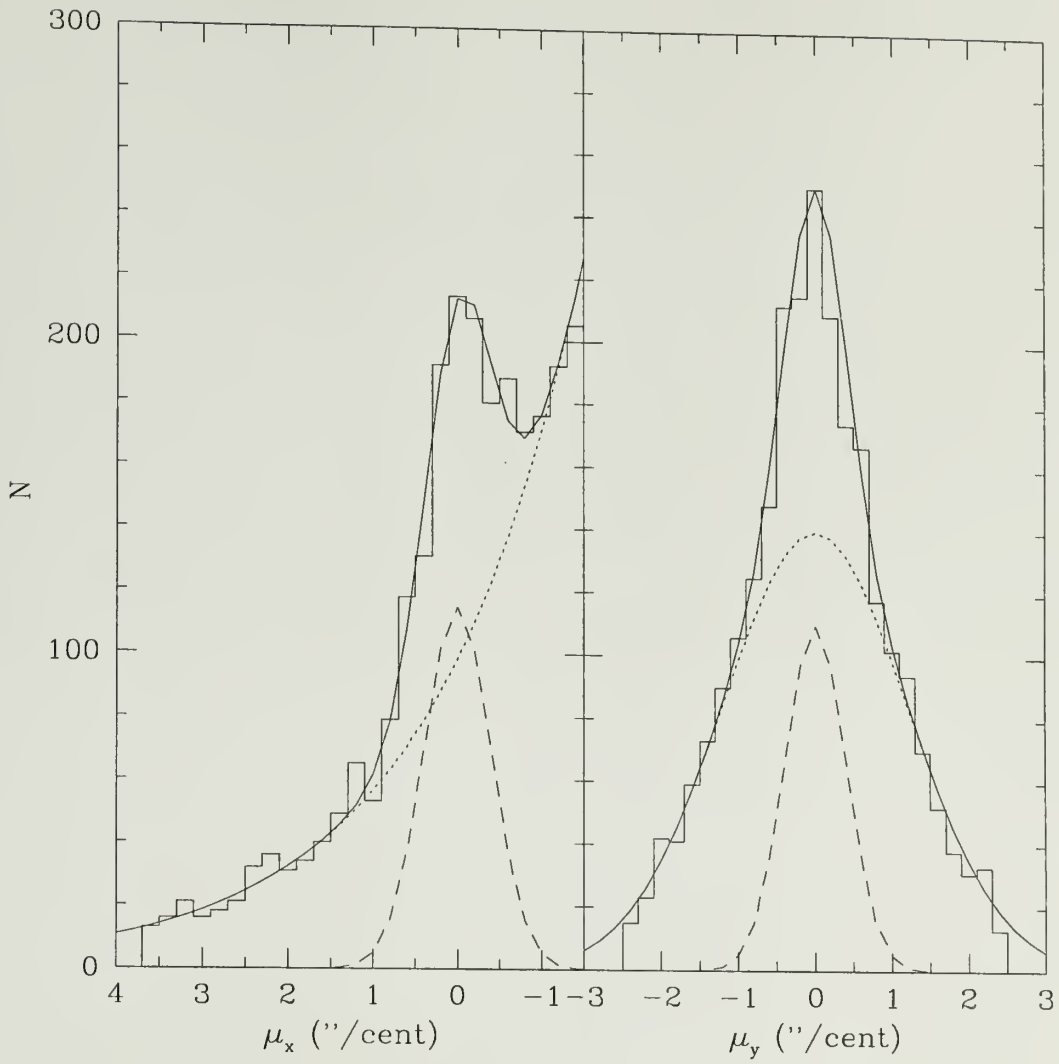

Fig. 2.2.— Histograms for the μ_x, μ_y data points shown in Figure 2.1. The dotted lines represent the field distribution functions, the dashed lines represent the cluster distribution functions, and the solid line represents the overall distribution. The lines have been vertically adjusted by eye to match the histogram binning.

membership probabilities of the cluster members, and identify a relationship between a probability threshold for membership and completeness of cluster recovery.

2.4.3 Results

Does the maximum likelihood estimator recover the simulation input parameters? Table 2.3 reports the mean best fit parameters and standard deviations for 100 simulations for each f. The results show a reliable recovery of parameters in all cases with no systematic bias within a standard deviation, with the exception of $\sigma_{x,c}$ and $\sigma_{y,c}$ which appear to be slightly underestimated in the $f = 0.5$ case. Note that larger f cases result in an increased error in N_c.

Table 2.3: Mean best fit parameters and standard deviations for 100 simulations using "true" parameters. Units are stars for N_c and N_f and "/century for the other parameters.

Parameter	true	$f = 0.5$	$f = 0.8$	$f = 0.9$
N_f	$fN_c/(1-f)$	506 ± 17	2008 ± 33	4515 ± 46
N_c	500	494 ± 17	492 ± 33	485 ± 46
$\bar{\mu}_{y,f}$	0.00	0.00 ± 0.06	0.00 ± 0.03	0.00 ± 0.02
$\bar{\mu}_{x,c}$	0.00	0.00 ± 0.02	0.00 ± 0.03	0.00 ± 0.04
$\bar{\mu}_{y,c}$	0.00	0.00 ± 0.02	0.00 ± 0.03	0.01 ± 0.04
τ	1.80	1.81 ± 0.12	1.80 ± 0.06	1.79 ± 0.04
$\sigma_{y,f}$	1.20	1.20 ± 0.04	1.20 ± 0.02	1.20 ± 0.01
$\sigma_{x,c}$	0.40	0.35 ± 0.02	0.40 ± 0.03	0.39 ± 0.04
$\sigma_{y,c}$	0.40	0.35 ± 0.02	0.39 ± 0.03	0.39 ± 0.04
μ_1	-1.50	...	...	...
μ_2	3.70	...	...	...

Membership probability recovery also had similar success. Figure 2.3 shows the average fraction of real cluster members in a given probability bin p. The plot shows a robust agreement between real membership probabilities and those calculated by eq. 2.8. Furthermore, this result suggests that in a real data set it may be possible to weight cluster candidates by p in analyzing a sample as large as several hundred

candidates, which may prove useful in deriving a mass function or cluster spatial density.

A probability threshold imposes other effects. A sample with a high probability threshold can be considered relatively pure but may exclude many genuine cluster members with lower probabilities, affecting sample completeness, while a sample with low probability threshold may be complete, but with additional field star contamination which lowers the confidence of the overall sample. Figure 2.4 illustrates this trade-off, and shows that sample completeness depends on f.

2.4.4 Limitations

Although the results of the previous subsection appear promising, there are pitfalls when applying this method to real data. First, a large fraction of field stars in a sample makes it difficult to statistically identify the cluster stars in proper motion space. In a N *vs.* $\log p$ histogram (Figure 2.5), the cluster is easily seen at low f, but as f becomes as large as 0.9, more candidates are distributed into the lower p bins due to this mathematical effect. This result suggests that f should be as low as possible, and cluster extraction will likely require an additional filter, such as color or spectral type, to eliminate as many field stars as possible from the sample before the fitting procedure.

Second, the distribution function parameters are functions of magnitude. Unfortunately, faint stars have poor photometry and positional accuracy. This means that the faintest stars will have large proper motion dispersions, ultimately diluting their probabilities and introducing more field star contamination. To make matters worse, a degradation in completeness of objects detected at the faint end reduces the number of cluster stars in the sample, which weakens the statistical fit and disperses candidates to lower p as discussed in the previous paragraph. The faintest stars may even fail to form any resemblance to a gaussian, consequently making membership probablities unreliable.

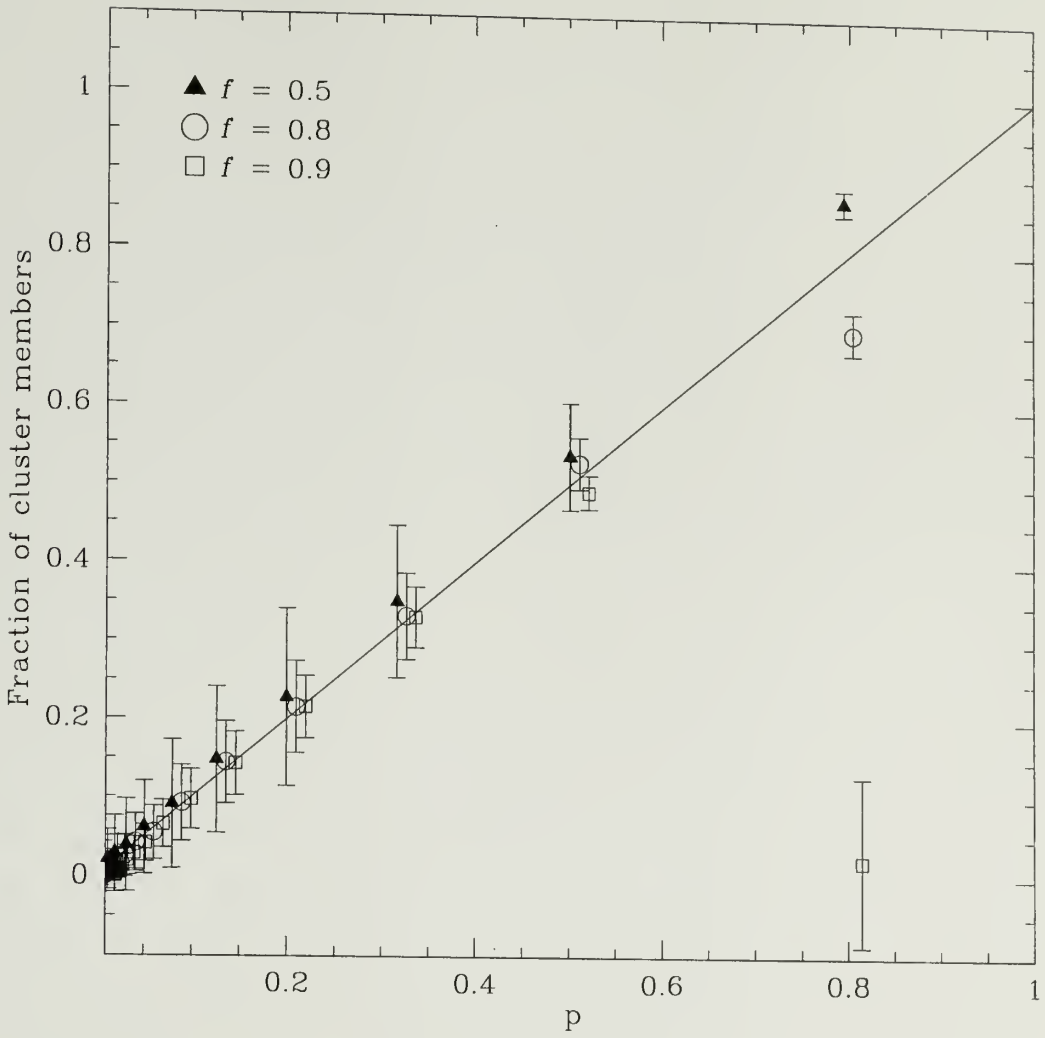

Fig. 2.3.— Fraction of simulated stars in a probability bin p that are real cluster members. The solid line represents a direct linear relationship. Data points are logarithmically spaced. The poor fits for $p = 0.8$ are result from small numbers of stars in that bin.

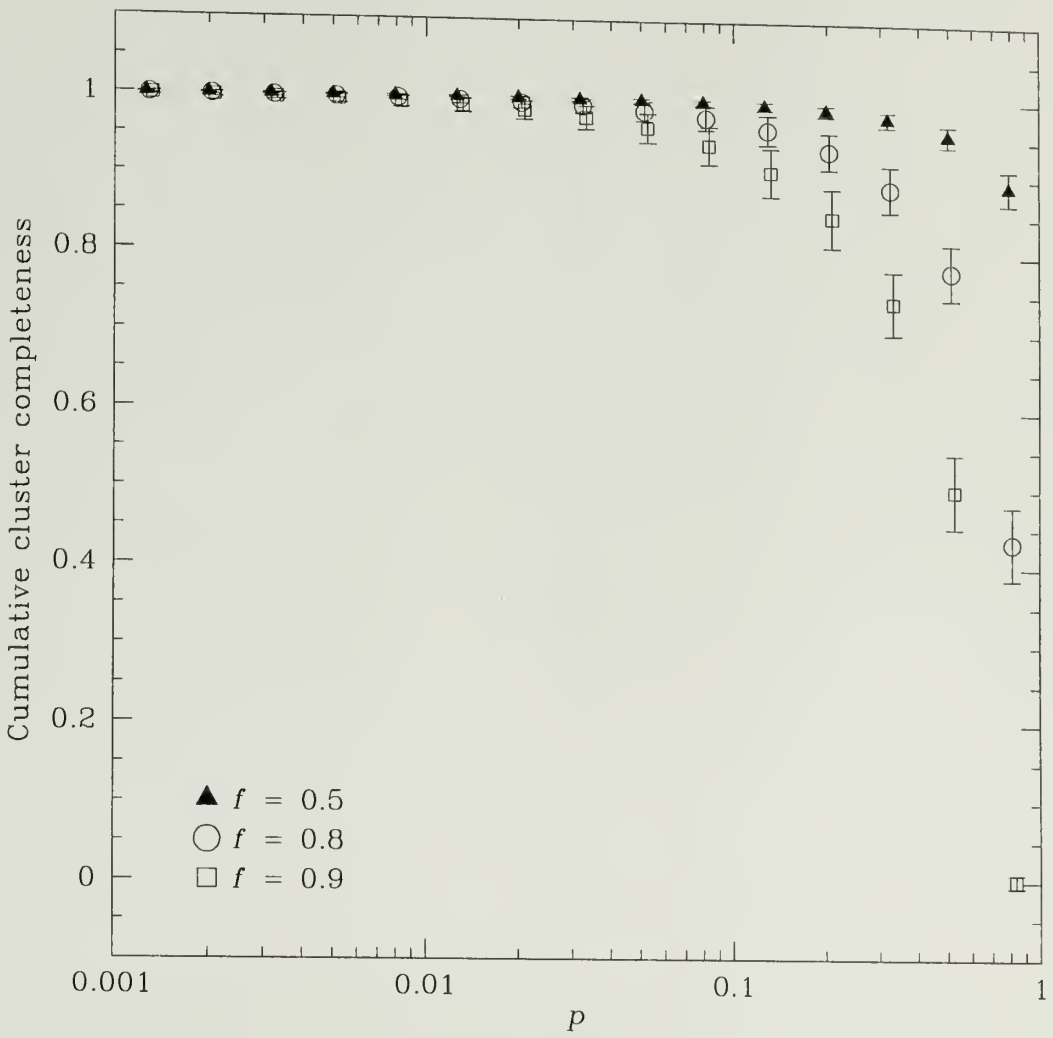

Fig. 2.4.— Cumulative recovery completeness of cluster based on probability threshold. Field contamination at higher f causes a lower completeness at a given p.

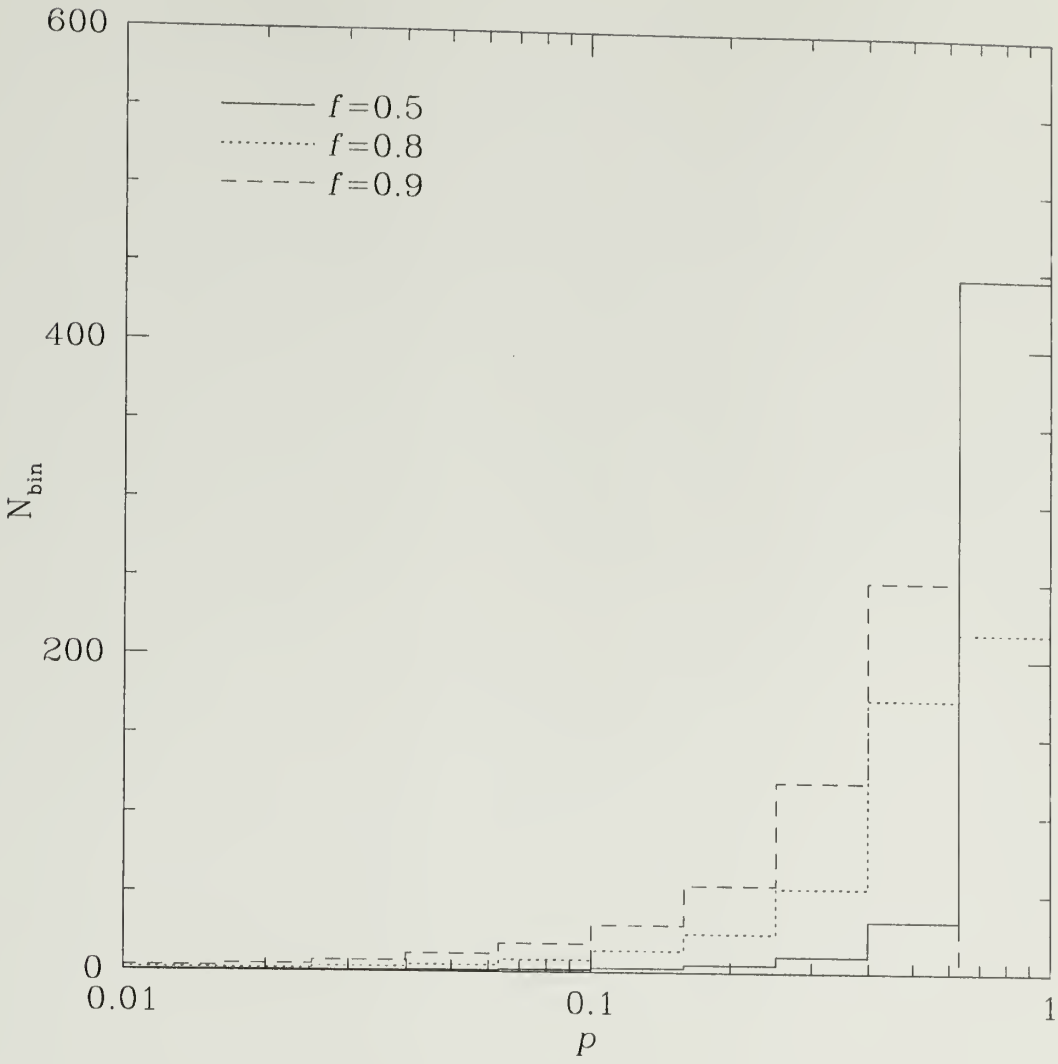

Fig. 2.5.— Mean histograms of membership probabilities for the artificial cluster members. The solid histogram corresponds to $f = 0.5$; the dotted histogram corresponds to $f = 0.8$; the dashed histogram corresponds to $f = 0.9$. Higher f values redistribute otherwise high probability candidates into lower probability bins, making membership selection more difficult.

2.5 Summary

I have proposed to use the photometry and astrometry from sky survey data to extract the members of a suitable open cluster, the Pleiades, in order to assess its dynamical structure compared with theoretical predictions. Members of the cluster will exhibit a distinct, well-defined proper motion relative to the bulk of the background field stars. This chapter specifically described a method to assign a cluster membership probability to every star in the field of interest.

A statistically rigorous method for evaluating the proper motion distribution of field and cluster stars was presented. The form of the distribution function of stars in proper motion space is determined empirically. Maximum likelihood fitting of the distribution function parameters allows the calculation of individual proper motion membership probabilities. Monte Carlo simulated data sets proved the success and reliability of the method under ideal circumstances by recovering the properties of an artificial cluster with accurately known distribution function parameters. The method breaks down under circumstances such as high concentration of field stars or a large dispersion of proper motion values for cluster stars, both of which will occur for a real sample of faint stars near the detection sensitivity limit.

CHAPTER 3

SKY SURVEY DATA

3.1 Introduction

This chapter describes the primary sources of data used in this thesis research. To achieve the science goals specified in Chapter 1 for the Pleiades cluster, this research will use photometry covering a variety of wavelengths in the optical and near-infrared, and positional measurements spanning two epochs of sufficient timescale for proper motion detection over the entire Pleiades field.

3.2 2MASS

3.2.1 Hardware and mapping strategy

The Two Micron All Sky Survey (2MASS) is presently mapping the sky with northern and southern telescope facilities: identical 1.3 m aperature telescopes with 3-channel cameras containing optics and liquid nitrogen-cooled 256×256 pixel NICMOS3 arrays capable of simultaneously imaging at J (1.2 μm), H (1.6 μm), and K_s (2.2 μm) with 2" spatial resolution. Each image frame represents a $\sim 8.5' \times 8.5'$ field of view. The surveying technique involves scanning roughly 6° in declination at constant right ascension, using declination steps which provide about 5/6 frame-to-frame overlap in declination, to build integration time, filter out bad pixel responses, and smooth the undersampled pixels. The mechanical feasibility of this technique is due to the scanning secondary mirror, which keeps a field locked on the telescope focal plane for the total exposure time while the primary mirror scans at a constant rate in declination. In addition, each field is imaged using a 52 ms exposure ("Read 1") and

then a 1.3 s exposure ("Read 2 – Read 1") to provide an extended dynamic range ($\sim 4-16$ mag in K_s). Calibration scans are performed several times throughout each night to repeatedly observe standard fields containing hundreds of reference stars. Using $8.5' \times 6°$ strips, the 2MASS telescopes each survey tens of square degrees per night and will thus cover virtually the entire sky by 2001.

3.2.2 Sensitivity and statistical accuracy

The sensitivity of 2MASS in all 3 bands is limited by Poisson photon noise due to atmospheric flux from OH emission in the airglow layer at roughly 100 km, and additionally due to thermal emission in the K_s band. Corresponding magnitudes to exceed signal-to-noise ratio (SNR) of 10 are given by the Level 1 Science Objectives and Specifications document: 15.8, 15.1, and 14.3 for J, H, and K_s respectively. For regions outside the galactic plane where confusion is not prominent, reliability is ≥ 0.9995 and completeness is ≥ 0.99 for SNR ≥ 10. The positional accuracy of 2MASS is specified as better than 0.5", with 0.2" accuracy currently achieved, and 0.1" ultimately possible.

3.2.3 Data processing and catalog content

Data taken at the telescope facilities are stored on magnetic tape and then shipped to the Infrared Processing and Analysis Center (IPAC) for processing. IPAC has developed an automated data reduction pipeline to process the raw images into single coadded $8.5' \times 17'$ image frames; perform astrometric analysis; extract point source and extended source brightnesses and positions; calibrate to a globally self-consistent internal photometric system (within 1%); and output an image atlas, a point source catalog, and an extended source catalog. In short, the point source catalog contains all necessary information for performing stellar astronomy analysis, such as source positions, magnitudes, uncertainties, confusion effects, and probabilities of photometric contamination from mechanical artifacts such filter glints, diffraction spikes,

and persistence images from bright stars. Additionally, the point source database contains correlated sources from (1) the Tycho catalog for bright stars ($K_s \leq\sim 9$); and (2) the USNO-A catalog (described below) including positional offsets, blue and red magnitudes, and the number of 2MASS-optical association matches for each source.

3.3 USNO-A

The USNO-A catalog (now in its second version) contains sources extracted from digital images of the first epoch Palomar Sky Survey (POSS I) the POSS I O (blue) and E (red) plates for DEC $> -35°$. The POSS photographic plates were digitized using the Precision Measuring Machine (PMM) (Monet 1998) at the U. S. Naval Observatory (USNO). The catalog requires a blue-red match with a correlation radius of 2". Typical positional errors are $\sim$ 0.1". The catalog goes as deep as B_O = 21 and R_E = 20. For declinations $< -35°$, similar sources were extracted from digitized European Southern Observatory (ESO) R (red) survey plates and Southern Research Council (SRC) J (blue) plates, but these cannot be used for proper motion measurements due to an insufficient time baseline.

POSS I was completed roughly 40 years prior to 2MASS, thus positional accuracies of 2MASS and USNO-A provide a strong detection of proper motions for several of the clusters listed in Table 2.2. Since USNO-A is correlated with 2MASS during pipeline processing, the 2MASS database directly provides a proper motion measurement via the relative positional offsets.

3.4 Additional Plate Material

Although 2MASS-USNO-A provides a convenient source of proper motion information, it is limited by POSS I blue which reduces sensitivity by 0.5 - 1.0 R for faint, low mass stars which are intrinsically red in color. To perform a more sensitive search in the Pleiades cluster, Monet (1999, priv. comm.) produced (1) a new POSS I E

source list in the Pleiades region that eliminated the O detection requirement and (2) a source list from second generation Palomar Observatory Sky Survey (POSS II) (Reid et al. 1991) in the F (red) band. The POSS I red - POSS II red source lists provide data for a slightly more sensitive proper motion search in the Pleiades than 2MASS and USNO-A[1].

[1]Since the time this Pleiades data was produced, the positional specifications of 2MASS have been demonstrated to exceed nominal accuracies of 0.5" (2MASS Level 1 Specifications Document) to meet or surpass the 0.1" accuracy of the PMM detections, and thus a proper motion search using POSS I red plates and 2MASS would potentially improve proper motion measurements by 10% or so over the longer time baseline than POSS I - POSS II.

CHAPTER 4

FAINT PROPER MOTION SEARCH FOR LOW MASS MEMBERS OF THE PLEIADES CLUSTER

4.1 Introduction

4.1.1 Previous work

The Pleiades cluster represents an appropriate laboratory for stellar dynamics – bright and rich in stars, but old enough to be dynamically evolved. Surveys of the Pleiades date back to Trumpler (1921) and Hertzsprung (1947) (HII). More recent work includes those of Jones (1981), Haro, Chavira, & Gonzalez (1982) (HCG), van Leeuwen (1983), Stauffer et al. (1991) (SK), and Schilbach et al. (1995). The last large, faint proper motion survey was that of Hambly, Hawkins, & Jameson (1993) (HHJ) which revealed 440 probable members out to several degrees from the cluster center. Although the HHJ survey discovered many low mass cluster members, it was spatially incomplete, and the authors predicted that a larger survey would be fruitful. The last decade has seen many deep photometric searches for brown dwarfs in small fields aimed at studying the substellar mass function, such as Stauffer et al. (1989); Stauffer, Hamilton, & Probst (1994); Zapatero Osorio, Rebolo, & Martín (1997), Festin (1998), and Bouvier et al. (1998). Most have concluded that brown dwarfs are abundant in the Pleiades, but not numerous enough to contribute significantly to the total cluster mass. Observations of lithium absorption in brown dwarfs has lead to a precise age measurement for the Pleiades of 120 Myr (Stauffer, Schultz, & Kirkpatrick 1998), a result which has interesting implications for the dynamical state of the cluster as well as stellar structure astrophysics.

4.1.2 Motivation

Despite a rich history of vigorous research in the Pleiades, the spatial incompleteness of previous surveys leaves some basic but critical properties of the cluster poorly constrained, such as its overall extent, structure, mass function and total mass. For example, the mass function slope below 0.5 $M_{\odot}$ could be rising (Bouvier et al. 1998) or more flattened (Hillenbrand 1997). Even a rising mass function suggests that substellar objects contribute no more than about 5% of the total Pleiades mass. However, confirming this result from an independently measured dynamical mass has been difficult. For example, measurements of the dynamical mass based on internal velocity dispersion suggest a mass of 460 – 690 $M_{\odot}$ (Jones 1970). van Leeuwen (1983) found a larger dynamical mass also using high precision proper motions. Estimates of the dynamical mass based on an estimated tidal radius are more scattered, spanning 530 – 8000 $M_{\odot}$ (Raboud & Mermilliod 1998a). Even with wide-field observations, measuring the Pleiades tidal radius is problematic as it lies predominately along the line of sight and the cluster's axes are expected to be tidally distorted. A reliable mass function would provide a precise estimate of both the dynamical mass and the tidal radius towards the Galactic center, and would thus bring previously discrepant results into agreement.

The internal dynamical state of the Pleiades is traced by its radial structure which on average indicates the distribution of internal velocities. Thus its mass function should be spatially dependent. The Pleiades at an age of 120 Myr is expected to exhibit mass segregation, but the edge of the cluster has not yet been detected. A complete measurement of the Pleiades mass function thus requires detection of stars in the outer reaches of the cluster. Although previous searches have made some progress towards unveiling the Pleiades, a more precise, definitive treatment of these issues requires a faint proper motion search that covers the whole cluster.

This chapter describes a search for low mass members of the Pleiades cluster. The primary scientific goals of this search are to (1) characterize its fundamental structure; (2) characterize mass segregation in the cluster; and (3) precisely measure the mass function in the $1 - 0.1 M_{\odot}$ regime. Other goals include searching for Pleiades brown dwarf candidates, particularly any new objects strattling the lithium depletion boundary (Stauffer, Schultz, & Kirkpatrick 1998), and providing reliable empirical data to test theoretical isochrones in optical-infrared colors down to the hydrogen burning limit. This chapter focuses on the derivation of the Pleiades sample. The search is supplemented with spectroscopic observations extensive enough to compromise a subsequent chapter (Chapter 5). I discuss the ultimate scientific results in Chapter 6.

4.2 Selection procedure and criteria

4.2.1 POSS data

All POSS plates were scanned by the PMM prior to this investigation. Monet (1999, priv. comm.) has processed the POSS data into a catalog that contains positions and instrumental photographic magnitudes for POSS I E and POSS II F point source detections. Monet performed a tangent plane projection in the Pleiades field of the form (eg. Birney 1991)

$$\xi = \frac{\cot\delta \sin(\alpha - \alpha_c)}{\sin\delta_c + \cos\delta_c \cot\delta \cos(\alpha - \alpha_c)} \tag{4.1}$$

$$\eta = \frac{\cos\delta_c - \cot\delta \sin\delta_c \cos(\alpha - \alpha_c)}{\sin\delta_c + \cot\delta \cos\delta_c \cos(\alpha - \alpha_c)} \tag{4.2}$$

where α_c and δ_c are the decimal right ascension and declination values for the nominal center of the cluster located at RA = $3^{\rm h}47^{\rm m}$, DEC = $24°7'$ (Lyngå 1987). Monet correlated the POSS I E detections with POSS II F detections in a 10° radius around the Pleiades nominal center. The correlation radius was 1". The correlations provided a transformation between the POSS I and POSS II coordinate systems given by

$$\xi_I = A_\xi + B_\xi \xi_{II} + C_\xi \eta_{II} \tag{4.3}$$

$$\eta_I = A_\eta + B_\eta \xi_{II} + C_\eta \eta_{II} \tag{4.4}$$

Results are listed in Table 4.1 in units of 0.01 μm where 1500×0.01 μm corresponds to about 1". Overall 1.5×10^6 correlations were found in the field, many of which are spurious sources or artifacts, and unpaired sources, ie. detections with no correlation less than 1"), which number about 2.1×10^6 for each POSS I and POSS II field, were sorted into separate lists. The 40 year baseline between POSS I and POSS II will yield a positional shift of greater than 1" for Pleiades members based on the mean Pleiades motion from previous surveys. Thus Pleiades members were to be located in the lists of unpaired detections.

Table 4.1: Coefficients for astrometric transformation given in eq. 4.3 between POSS I and POSS II tangent plane coordinates in units of 0.01 μm.

Coeff.	ξ	η	ξ error	η error
A	3.48568291E+00	4.07704484E+00	4.46362262E-03	4.81523199E-03
B	1.00000124E+00	-2.37408999E-06	1.66435662E-08	1.79546165E-08
C	1.99358342E-07	1.00000673E+00	1.72123167E-08	1.85681688E-08

A correlation of the lists of unpaired detections using a 5" search radius resulted in 5.0×10^5 correlations. Before computing proper motions, I attempted a first-order correction for systematic dispersion of the POSS I - POSS II positional offsets over large plate areas and across plate boundaries. Using the stars in the best dynamic range, ie. those brighter than $R_E = 18$ according Figure 4.1, the mean positional offsets were computed for 10 arcmin $\times$ 10 armin boxes throughout the Pleiades field and then each individual positional offset was "zeroed" according to the mean of its corresponding box. Figures 4.2 and 4.3 and display images derived from the mean ξ and η offsets for each box. Ultimately, the dispersion in positional offsets for both the

mean field and cluster and have been tightened as demonstrated by Fig 4.4. However, the technique does not eliminate outliers.

The positional offsets for each correlation were converted into proper motions simply by re-converting each tangent plane positional offset into an angular motion scaled by the time differential between the relevant POSS I and POSS II plate observations, typically 35-40 years.

4.2.2 Correlating POSS data with 2MASS

The list of POSS I - POSS II proper motions is too large and too contaminated in itself to be useful in extracting cluster members. A straightforward solution to this problem is to filter out field stars according to their colors. Field stars with colors obviously different from those of previously known cluster stars can be eliminated from the overall sample. Thus it is helpful to first correlate the POSS sample with 2MASS photometry to derive $R_E - K_s$ and $J - K_s$ colors. 2MASS provides accurate near-infrared photometry of cool stars that emit most of their luminosity in the infrared wavelength region. The broad wavelength coverage from 0.6 – 2.2 μm is sensitive to the surface temperature of cool stars and thus helps to distinguish faint, red sources that belong to the Pleiades. Furthermore, each star in the sample is a correlated $EFJHK_s$ detection consequently eliminating spurious detections and artifacts such as diffraction spikes present in both POSS and 2MASS databases.

More than 96% of the $\sim$ 775,000 JHK_s 2MASS detections in the field had POSS counterparts. Most of the 2MASS sources without POSS correlations were in regions at the outer edge of field where the POSS plates terminated within the 2MASS aperture (for example see lower left of Figure 4.2). The correlations effectively constituted a database of positions, $EFJHK_s$ magnitudes, and proper motions.

Duplicate sources from overlap regions needed to be removed from the sample. 2MASS scan-to-scan overlap stars could easily be identified based on their positions (usually only a few tenths of arcsec apart, but anything within 2" was considered

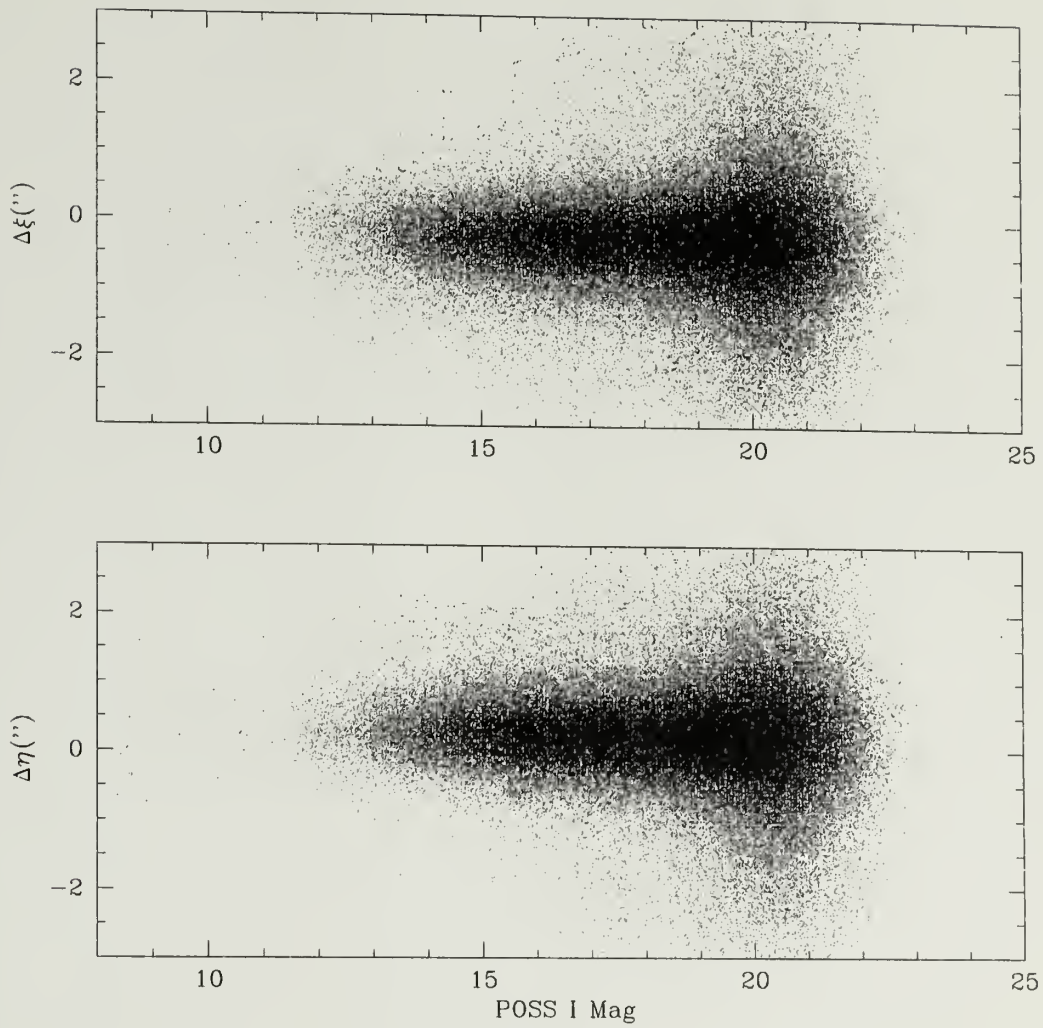

Fig. 4.1.— ξ and η offsets as a function of POSS I (red) magnitude for a sample of stars in the Pleiades field. Note the increase in POSS positional dispersion with decreasing brightness. The units of ξ and η have been converted into arcsec.

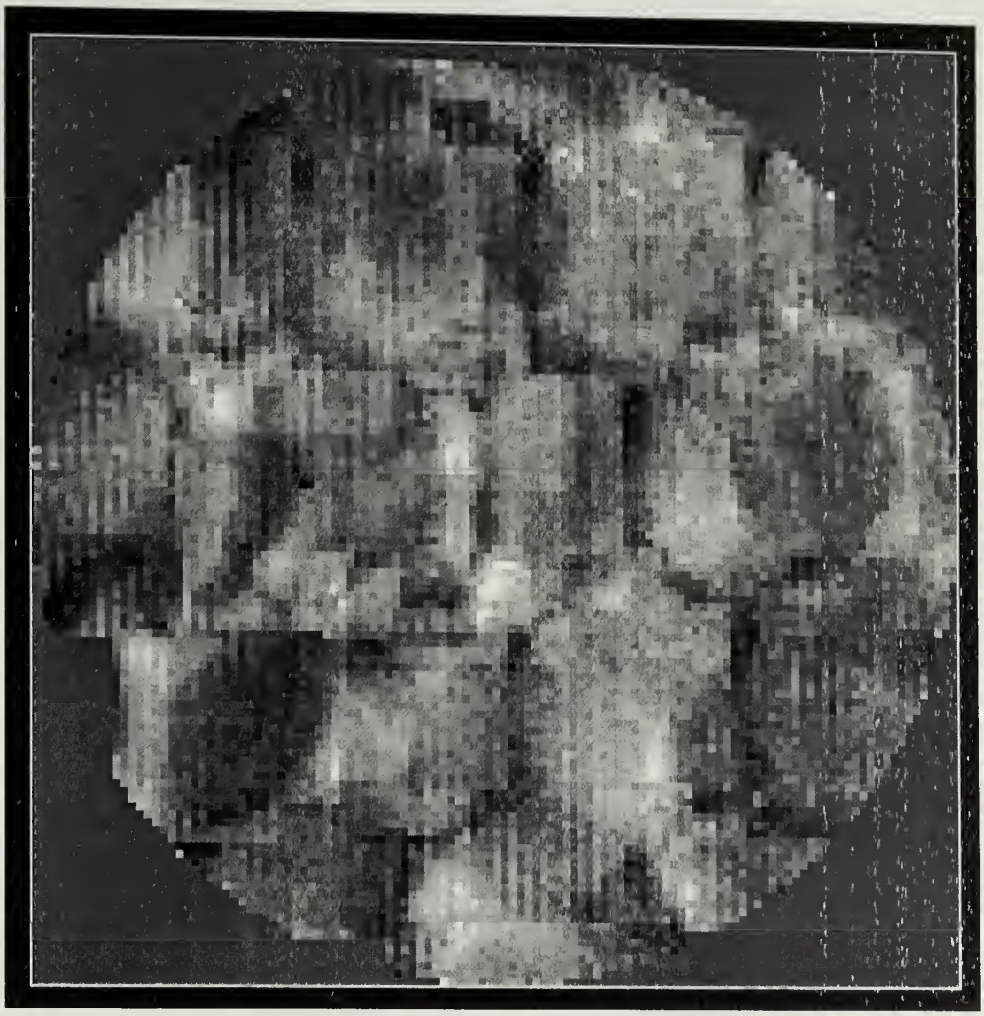

Fig. 4.2.— Mean POSS I - POSS II ξ offsets calculated in 10×10 arcmin boxes in a 10° radius around the Pleiades nominal center. East is on the left. The intensity of each pixel represents the mean offset for a box. The image has been stretched such that black regions correspond to roughly -0.2" and white regions to 0.7".

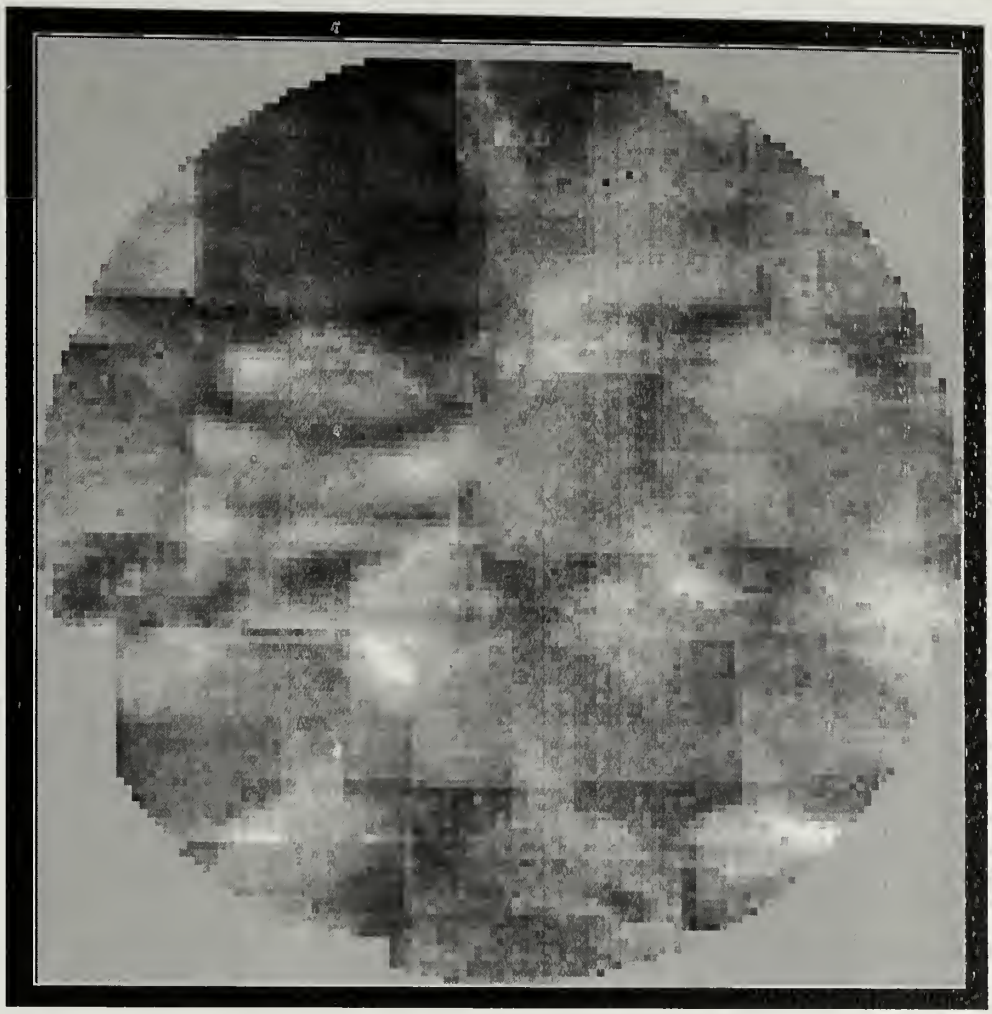

Fig. 4.3.— Analogous to Figure 4.2 for η offsets. The image has been stretched such that black regions correspond to roughly -0.2" and white regions to 0.7".

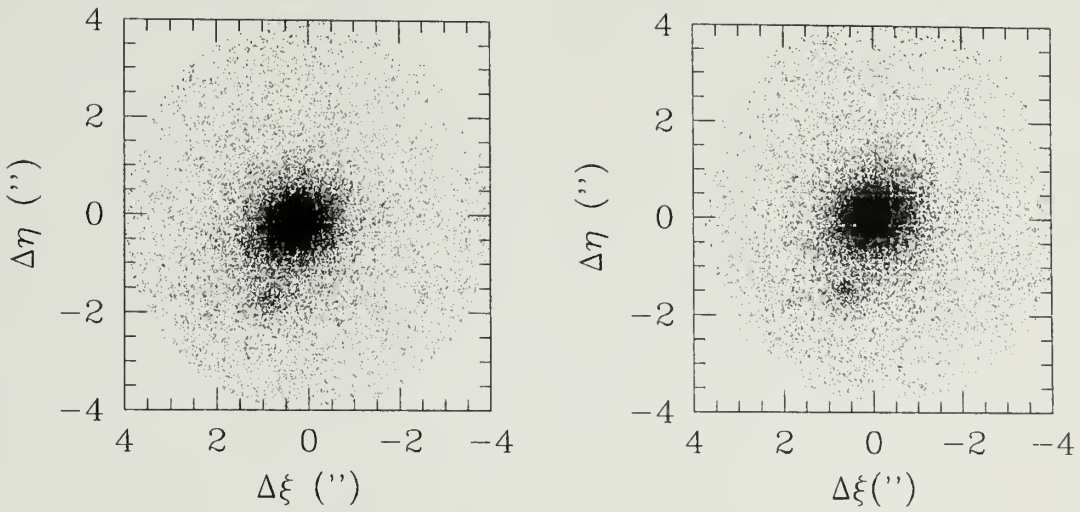

Fig. 4.4.— VPDs for 30000 stars in a few square degrees of the Pleiades field: comparison of raw offsets (left) and first order corrected offsets using the box means depicted in Figures 4.2 and 4.3. Note that the cluster, located near (0.8,-1.8) ", and field have been tightened and that the bulk of the field has been shifted closer to (0,0) ".

suspicious), similar JHK_s magnitudes, and equivalent POSS proper motions and magnitudes. In this case one detection of arbitrary choice (eg. the western detection) was kept in the sample and the others were eliminated. The total number of both duplicate types was less than 10% of the overall sample.

4.2.3 Magnitude and color cuts

Even in proper motion space the large area of the Pleiades search introduces a substantial amount of field star contamination. Figure 4.5, a $K_s : J - K_s$ Hess diagram (density of sources modelled as individual gaussian functions with individual uncertainties), shows that the color locus of Pleiades M dwarfs in the CfA Open Cluster Database[1] and the HHJ sample is heavily contaminated by field M dwarfs with $J - K_s \approx 0.9$. The field contamination increases at fainter magnitudes.

The 2MASS photometry is more precise than the POSS magnitudes, thus it is more appropriate to use eg. K_s photometry to define a magnitude cut. The mass range of interest is $\sim 1 - 0.08$ $M_\odot$, corresponding to roughly $10 \leq K_s \leq 14$ at the distance and age of the Pleiades. However, the faintest stars lie outside the best dynamic range of measurement. Figure 4.6 compares a POSS VPD of the HHJ stars against a VPD for just the faintest stars. The result is that faint stars will have a distribution that is difficult to characterize apart from the field at the cluster motion. Hence it is best to first derive a sample in a magnitude range where the method is most reliable.

To minimize this contamination, a broad color selection retained only sources with colors similar to known Pleiades members. Sources in the range $8.0 \leq K_s \leq 14.75$ were chosen based on the dynamic range of the PMM extractions at the bright end and by the sensitivity of the POSS plates at the faint end. The color selections are designed to include the faint portion of the Pleiades locus, in the range $10 \leq K_s \leq 14$.

[1]Provided by C.F. Prosser (deceased) and J.R. Stauffer, and which currently may be accessed at http://cfa-ftp.harvard.edu/ stauffer/, or by anonymous ftp to cfa-ftp.harvard.edu, cd /pub/stauffer/clusters/

I extended the faint end of the magnitude range beyond $K_s = 14$ to try to include objects near the hydrogen burning limit at $K_s \approx 14.5$. Sources near the locus of known members in K_s *vs.* $J - K_s$ and $R_E - K_s$ color-magnitude diagrams were selected. Figures 4.7 and 4.8 show the specific regions in the K_s *vs.* $J - K_s$ and $R_E - K_s$ color-magnitude diagrams respectively in which sources were selected. I deliberately chose broad regions to account for dispersion due to photometric error at faint magnitudes as well as binarity. For sources fainter than $K_s = 14$, those 2MASS sources that have a POSS I detection on the E plates only were included, increasing sensitivity to faint, red stars with respect to the USNO-A catalog (Monet & Corbin 1997). The sample consists predominately of K and M dwarfs after color selection. In total ~ 38000 sources to $K_s = 14$ and ~ 5700 sources fainter than $K_s = 14$ survived the color selection. In Figure 4.9, the density of points in the VPD for these color-selected stars reveals the cluster in proper motion space as well as the still-dominant field star population. The VPD shows that a bivariate gaussian function sufficiently represents the cluster distribution and proper motion membership probabilities can be computed.

4.3 Results

4.3.1 Distribution fitting and membership probabilities

Eqs. 2.4, 2.5, and 2.8 determine the relative cluster membership probabilities of individual sources. A rotation of proper motion vectors aligned the x-axis with the mean cluster motion. Note that Jones & Stauffer (1991) included a term in the distribution function to account for the decrease in membership probability at large radial distaces from the center of the cluster due to the exponential decrease in cluster surface density. One goal of this work is to determine the true radial structure of the cluster and thus a radial distance parameter was not included in the distribution function.

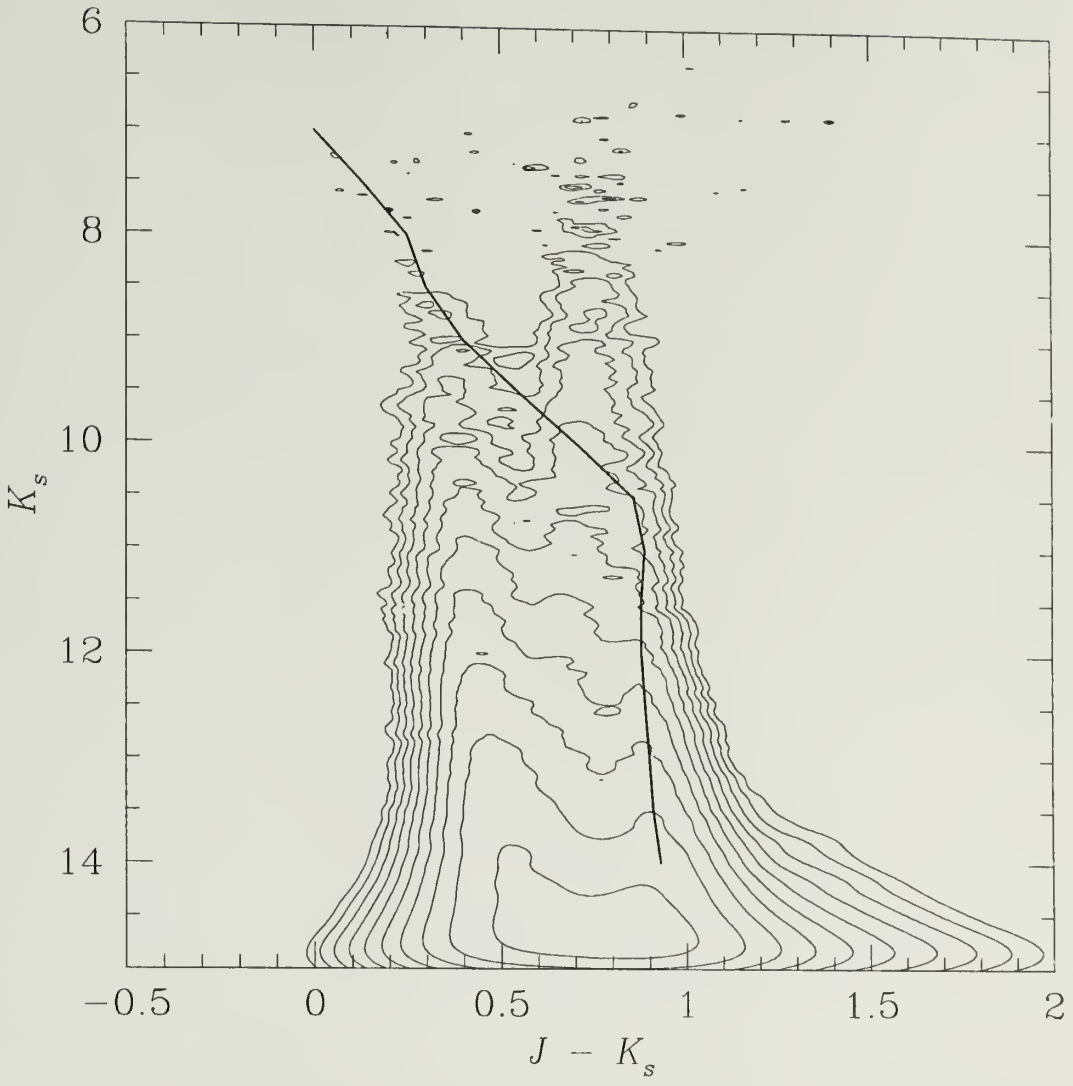

Fig. 4.5.— Contours derived from a $K_s : J - K_s$ Hess diagram for 2MASS JHK_s detections within a 5° radius of the nominal center of the Pleiades. Contour spacing covers about 2 orders of magnitude in logarithmic intervals of 0.2. The solid line represents the approximate 2MASS empirical colors for known members of the Pleiades in the CfA Open Cluster Database and HHJ catalog, drawn by eye. M dwarfs dominate the faint portion of the diagram at $J - K_s \approx 0.9$.

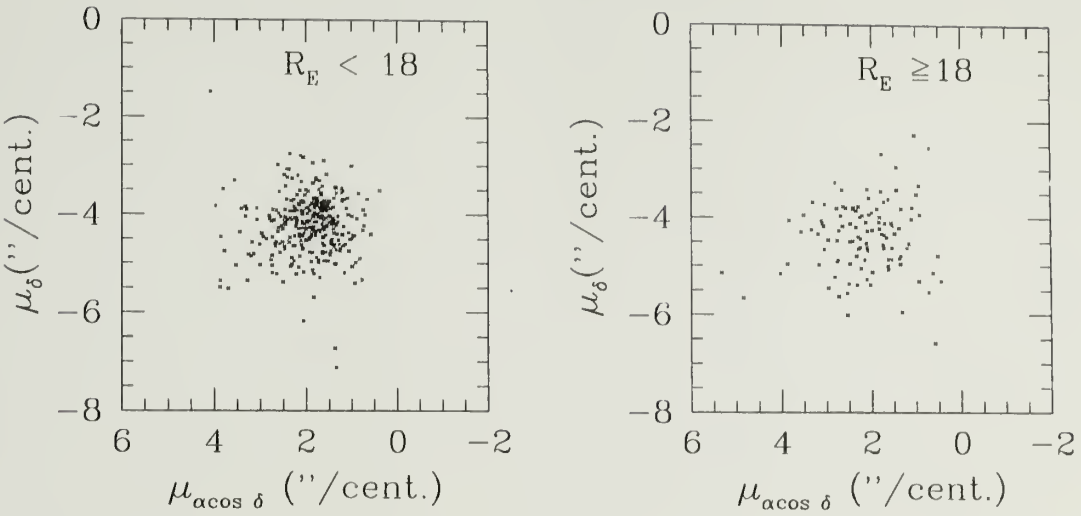

Fig. 4.6.— POSS VPDs for HHJ stars. The fraction brighter than $R_E = 18$ is at left while the fainter portion is at right. The faintest cluster stars are difficult to detect as a distinct gaussian with respect to the field since the cluster gaussian deteriorates and the field density increases at fainter magnitudes.

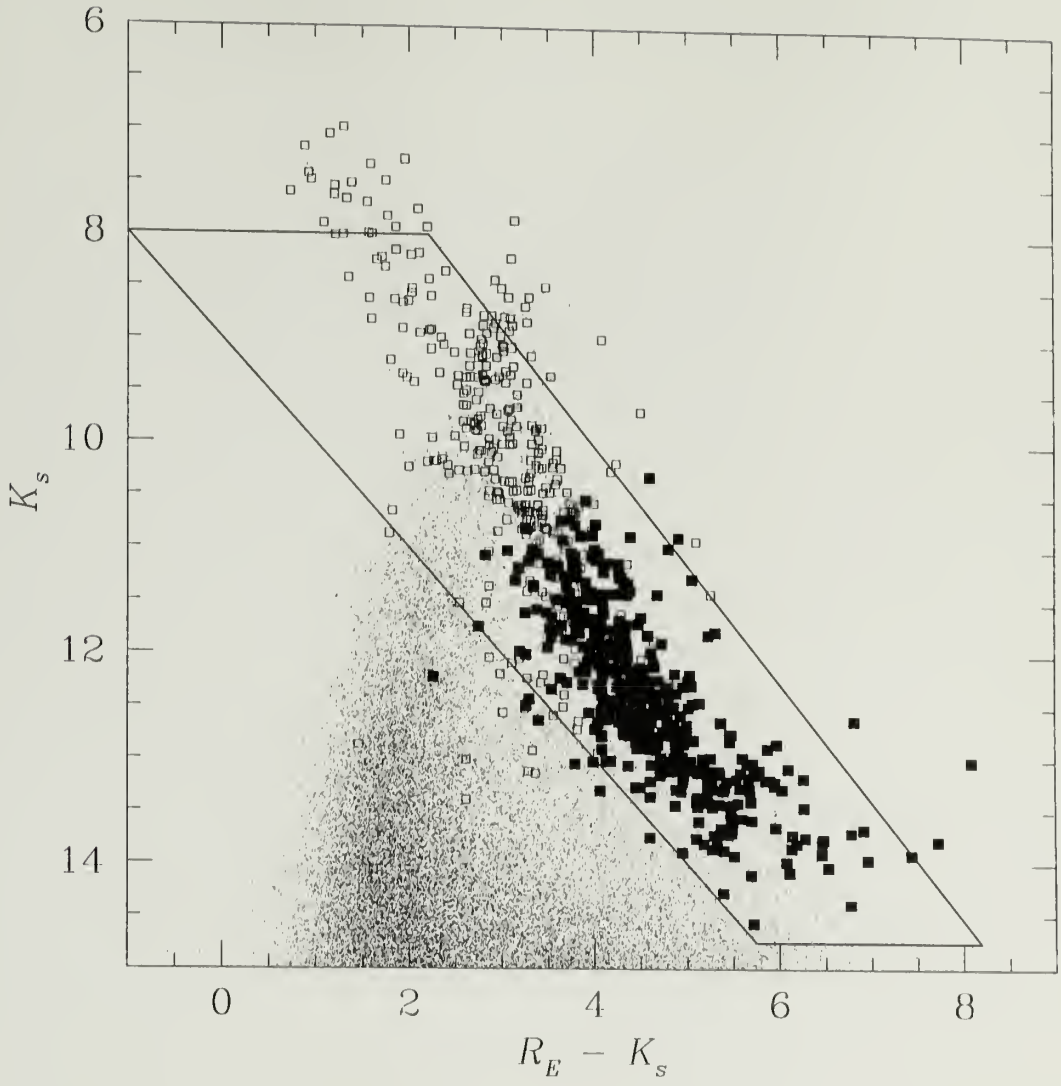

Fig. 4.7.— Color-magnitude diagram using instrumental R_E and 2MASS K_s magnitudes for field stars in a small area ($\sim$ 12 deg^2) around the Pleiades. The open squares represent 2MASS colors for a sample of previously published Pleiades candidates brighter than the HHJ sample while the solid squares represent 2MASS colors for HHJ stars. The boxed region depicts the region of color space selected for further proper motion analysis.

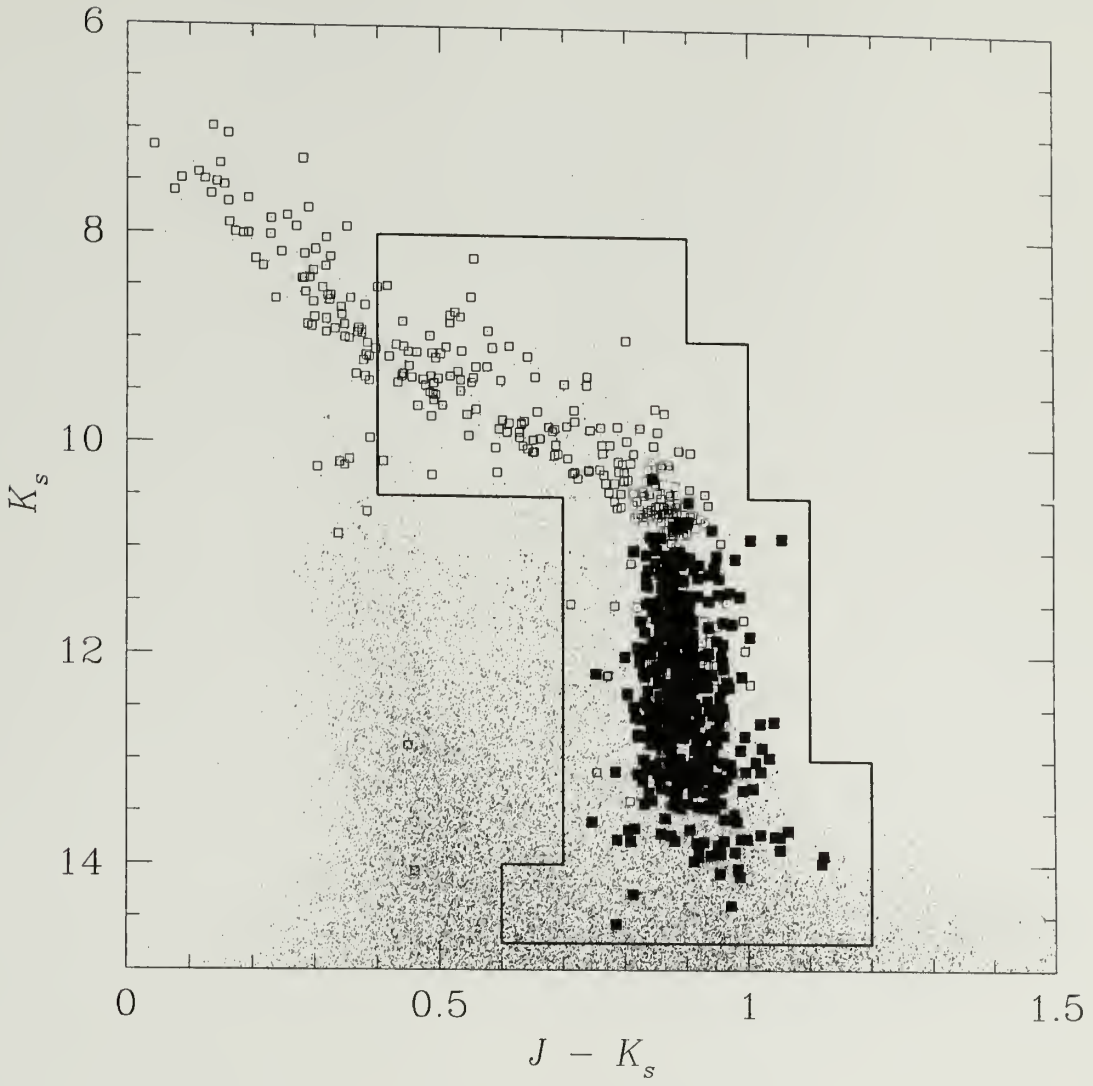

Fig. 4.8.— 2MASS K_s : $J - K_s$ color-magnitude diagram for the sources described in Figure 4.7. Symbols are as in Figure 4.7. The boxed region indicates sources that were color selected.

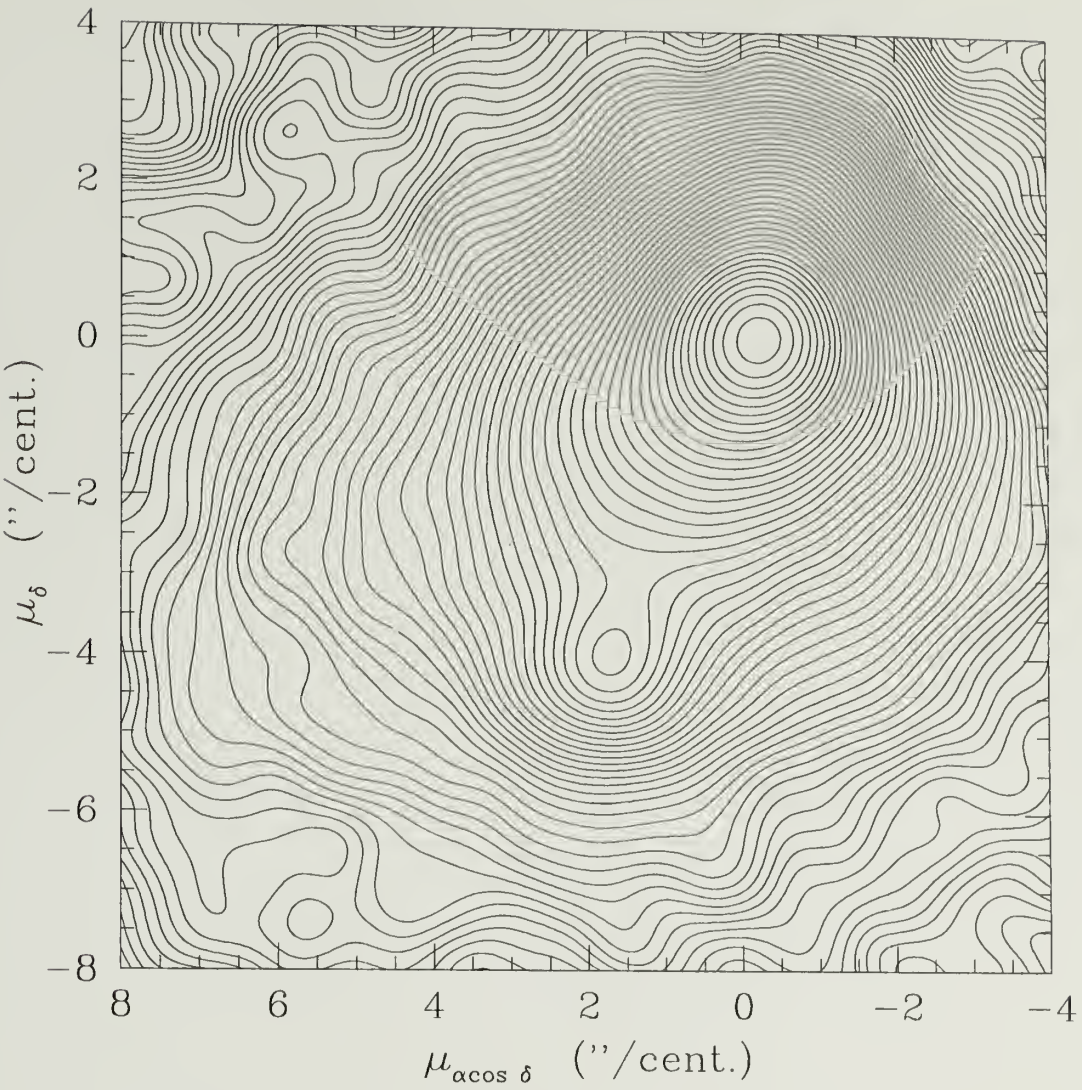

Fig. 4.9.— Contours derived from a Hess diagram of proper motion vectors after color selection for sources brighter than $K_s = 14$. The center of the field star distribution lies near (0,0) "/cent. and the cluster ditribution is visible near (2,-4) "/cent.

Before fitting the distribution parameters, the proper motion vectors were shifted and rotated $-66.3°$ to place the cluster near (0,0) "/cent. and align the x-direction along the cluster's mean vector. A boxed region approximately 5×5 "/cent. around the cluster centroid contained the sources used to fit the distribution function. A total of 5664 sources were found within the fitting region.

Due to the large number of field stars in our database, fitting the distribution function in small magnitude groups was difficult, particularly for faint stars. I fitted the distribution function for the entire database without a magnitude dependence. This will affect the membership probabilities by favoring parameters that best fit the magnitudes with the least field contamination. However, the effect should be small except at the faint end of the sample. Although I included $\sim$ 500 sources fainter than about $K_s = 14$, their membership probabilities are less reliable as those for the relatively brighter stars for two reasons. First, degradation in the PMM astrometry at faint magnitudes causes a larger dispersion in proper motion space which makes modelling their distribution difficult. The faint clusters members will be dispersed to smaller membership probabilities than relatively brighter cluster members. Second, field contamination increases at faint magnitudes. Membership of faint candidates will thus rely more heavily on spectra or other independent observations than the brighter stars.

Table 4.2 lists the parameter values that best characterize the distribution function. It suggests that substantial fraction of the sample are likely to be cluster stars and thus we can expect robust membership probabilities with which to select a smaller sample of high probability candidates. Fits to the distribution of μ_x, μ_y are depicted in Figure 4.10.

Membership probabilities were calculated using the best fit parameters in the distribution function. Figure 4.11 displays a histogram of membership probabilities p. The large area covered by this work results in enough field contamination to

Table 4.2: Best fit parameters for the Pleiades field distribution function. Units are stars for N_f and N_c and "/cent. for the remaining parameters.

N_f	4586
N_c	1078
$\mu_{y,f}$	0.17
$\mu_{x,c}$	0.04
$\mu_{y,c}$	0.06
τ	1.78
$\sigma_{y,f}$	1.20
$\sigma_{x,c}$	0.52
$\sigma_{y,c}$	0.98

numerically dilute the membership probabilities as indicated by the lack of sources with $p > 0.6$. However, Figure 4.11 shows that most sources with $p > 0.3$ are likely to be cluster members based on the overall distribution of probabilities. The spatial distribution of sources according to membership probability depicted in Figure 4.12 shows qualitative statistical consistency of proper motion membership probability with true association with the cluster.

A potential concern in this analysis is astrometric distortion near POSS plate boundaries. Is the sample affected by plate boundaries? Figure 4.13 shows the spatial distribution of candidates compared with the approximate location of the POSS I and POSS II plates. Clearly, plate effects are not *obvious* in the sample. Any hidden or lingering effects from plate boundaries should be identified during followup observations, where any region of a large number of spurious detections or higher than average field contamination may be suspicious.

The proper motions could have been derived by correlating POSS I red detections with 2MASS detections. The additional 8 – 10 years provides a longer baseline with which to measure proper motions. However, Figure 4.14 shows VPDs for both POSS I - POSS II and POSS I - 2MASS proper motions. The cluster region appears to contain

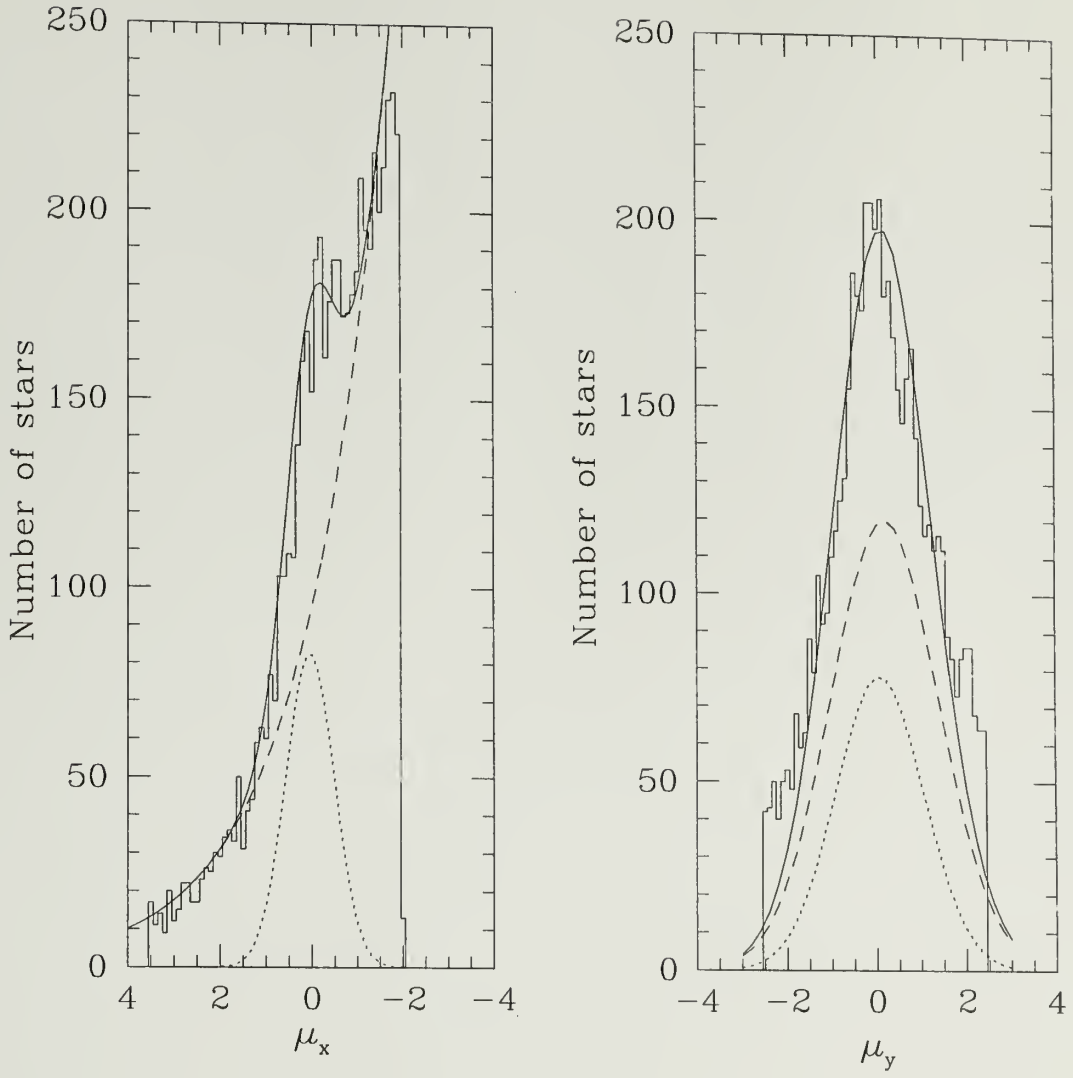

Fig. 4.10.— μ_x and μ_y histograms overlaid with the best distribution function fit (solid line). Also shown are the individual fits for the cluster (dotted line) and field (dashed line) distributions. All fits were vertically adjusted by eye to look consistent with data binning.

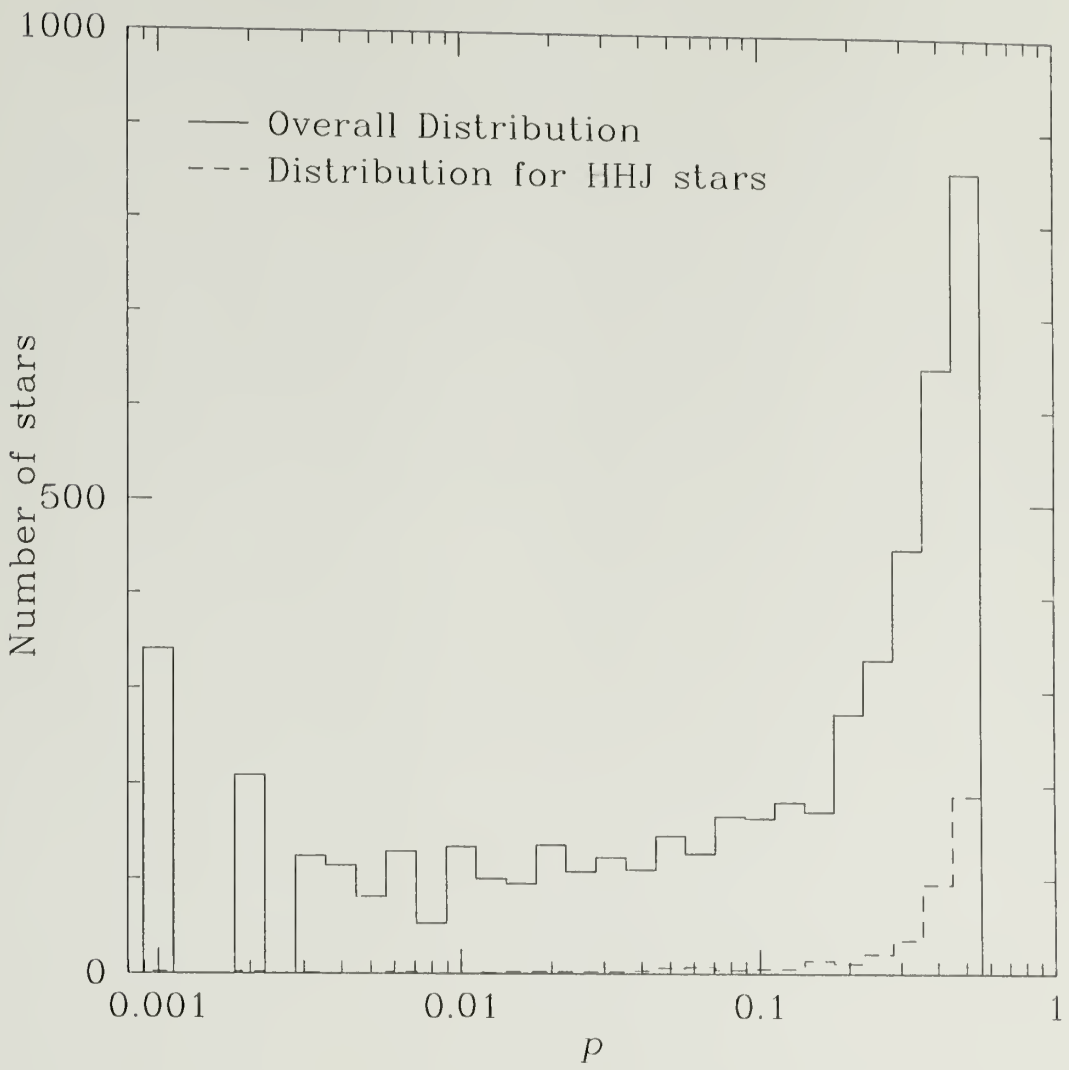

Fig. 4.11.— Distribution of membership probabilities p for Pleiades candidates. The dotted line shows a histogram of probabilities for stars identified with the HHJ sample. The sharp peak near $p \approx 0.5$ suggests that most cluster members have relatively high membership probabilites.

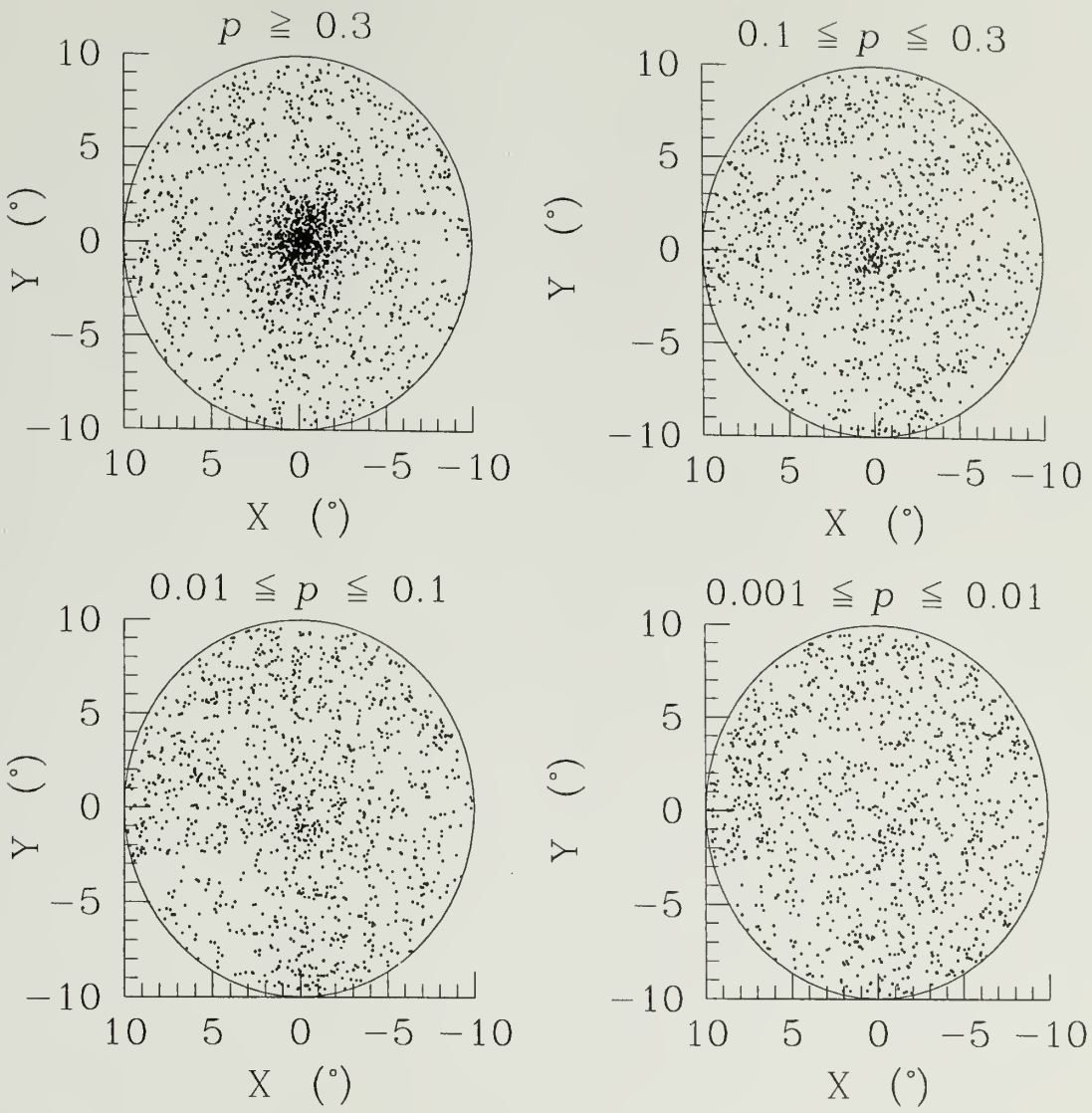

Fig. 4.12.— Spatial distribution of Pleiades candidates in the probability ranges $p > 0.3$; $0.1 \leq p < 0.3$; $0.01 \leq p < 0.1$; and $0.001 \leq p < 0.01$. X increases to the east and Y increases to the north.

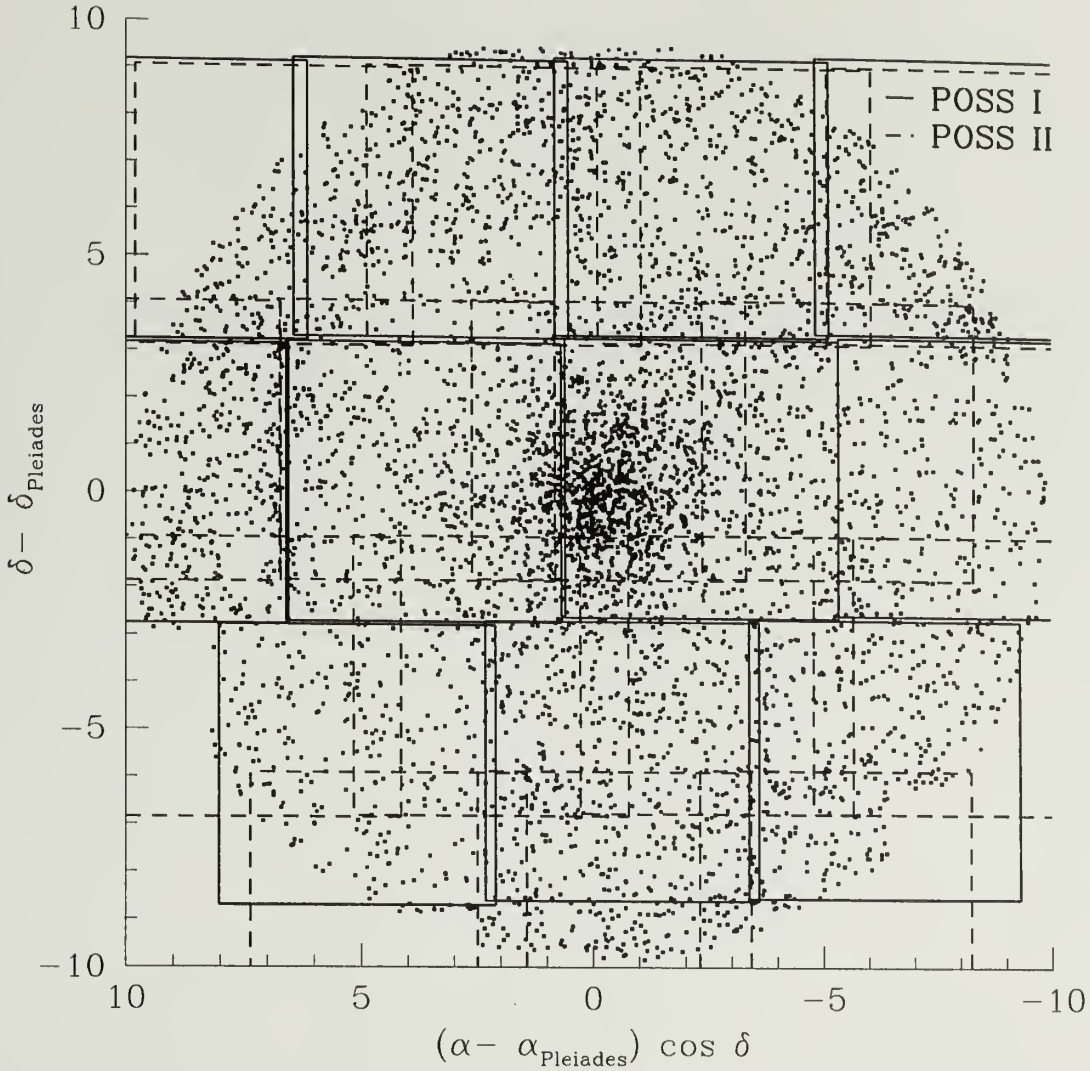

Fig. 4.13.— Approximate POSS I and POSS II plate boundaries superimposed on the spatial distribution of Pleiades candidates with $p \geq 0.001$.

similar field contamination in each case. Note that POSS I - 2MASS positions require systematic alignment between respective coordinate systems. A more careful analysis using POSS I and 2MASS sources may show a more favorable VPD.

4.3.2 Treatment of faint stars

Because proper motions of the faint stars shown in Figure 4.6 cannot be modelled with a distribution function, they cannot be assigned meaningful membership probabilities. Thus any faint star near the cluster mean motion is a candidate member. One first order technique for selecting faint stars as candidate members is to use the distribution function parameters for the brighter stars to form a large enough ellipse on the VPD that would likely contain faint cluster members. Confirming membership depends more heavily on followup observations than the brighter, higher quality sample. A second strategy would be to directly calculate the mean and standard deviation of μ_x and μ_y for faint HHJ stars, and impose a limits on the VPD in terms of the number of standard deviations. This is similar to the first technique and unfortunately equally uncertain.

Faint candidates were identified as those in the VPD within the ellipse at $p \geq 0.001$. The region $K_s = 14 - 14.75$ contined 432 stars within this ellipse near the cluster mean motion. None of the HHJ stars in this brightness range had USNO-A associations since they are presumably too faint and red to be detected on the POSS I O plates. Therefore, I included 2MASS sources that have a POSS I detection on the E plates only, thus increasing the search sensitivity to faint, red stars with respect to the USNO-A catalog. Most of these candidates are likely to be field stars; determining the cluster members will require further observations such as obtaining high precision radial velocities or atomic lithium absorption features.

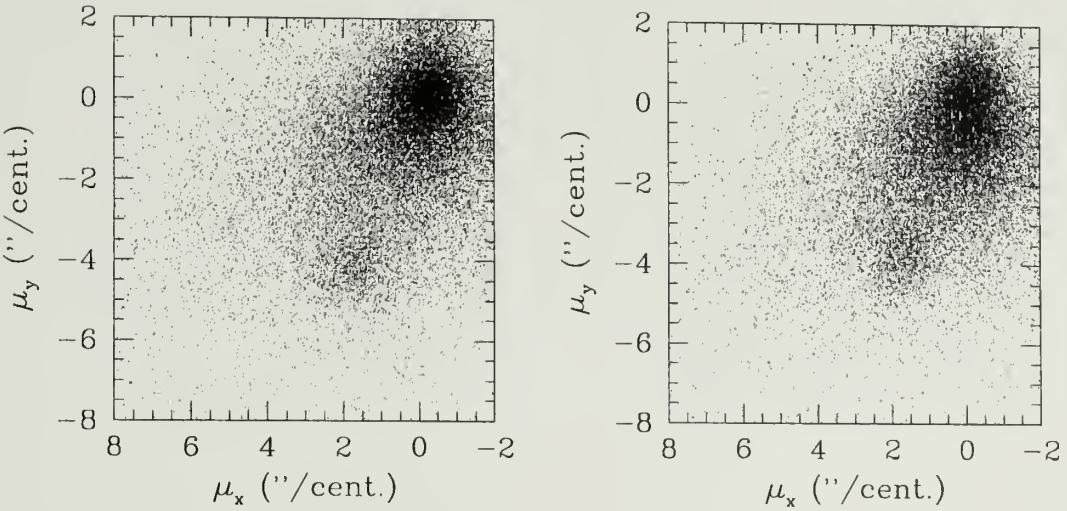

Fig. 4.14.— VPDs for proper motions derived from POSS I and POSS II (left), and POSS I and 2MASS detections for 38000 stars in the Pleiades field. Note that POSS I - 2MASS correlations require systematic alignment between respective coordinate systems.

4.3.3 Completeness and Sensitivity

This proper motion search has identified 4233 possible Pleiades members with $p \geq 0.01$. Roughly 1200 are high probability members with $p \geq 0.3$ within a 6° distance from the cluster center. Many candidates will actually be non-members at large radial distances.

The completeness of this proper motion search at the bright end is limited by the dynamic range of the PMM extractions. Counts for sources with correlated $R_E R_F J H K_s$ detections indicate that the PMM detections are complete up to $R \approx 8$, corresponding to ~ 1.5 $M_\odot$ for Pleiades members. Since our primary goal is to detect low mass stars, incompleteness at the bright end of our sample should not pose a significant problem due to the large amount of published data for bright Pleiades members.

Cross-correlating this sample with the HHJ sample estimates completeness. 92% of the 440 stars in the HHJ sample have been recovered, including several of their faintest objects such as HHJ 3 and HHJ 2 (albeit at relatively low membership probability), indicating that the search is relatively complete to $R = 19$. Most unrecovered HHJ stars had POSS proper motions that lie outside the distribution function fitting region (farther than ~ 2.5"/cent. from the mean cluster motion). The membership of these objects will require independent criteria, such as appropriate radial velocities. The search has also revealed 269 candidates with $p \geq 0.3$ that were in the HHJ survey area but not in their list.

The search has recovered 8 objects from the photometric search of Bouvier et al. (1998) including CFHT-PL-5 and CFHT-PL-10, 3 PPl objects from Stauffer et al. (1989) including PPl 13 and no objects from Zapatero Osorio, Rebolo, & Martín (1997) indicating that it reaches $R = 20$, but is very incomplete at the hydrogen burning limit and below.

4.4 Summary

To provide an extensive basis to measure the mass function and radial structure of the Pleiades, a search for low mass candidates was performed using POSS I and POSS II red band proper motions and 2MASS JHK_s photometry. The search extends to a 10° radius around the Pleiades nominal center, several degrees beyond the presumed edge of the cluster. The POSS red detections reach $R = 20$, a slightly better sensitivity than achieved by 2MASS-USNO-A alone. The search has produced a sample of 4233 candidates with $p \geq 0.01$. Roughly 1200 are highly probable candidates based on their high proper motion membership probability and their spatial proximity to the cluster. Several hundred are newly detected Pleiades candidates. Most of these candidates have USNO-A associations in the 2MASS database. The sample is relatively complete to $R = 19$ and recovered 92% of the HHJ catalog. The poor POSS photometry and astrometry for sources fainter than $K_s \approx 14$ make the distribution function fit impractical. Faint candidates were selected with similar proper motion to the cluster mean proper motion but meaningful membership probabilities cannot be assigned. The faint list contains recovered known members but is very incomplete near the Pleiades hydrogen burning limit. Further observations are required to assess and refine the list, especially the faintest stars.

CHAPTER 5

SPECTROSCOPIC STUDY OF LOW MASS PLEIADES CANDIDATES

5.1 Introduction

The purpose of this work is to study the structural properties of the Pleiades using a spatially complete sample of cluster members. Chapter 4 described the initial extraction of Pleiades candidates from a large database containing photometry and proper motions of stars in a large radius around the nominal center of the Pleiades. As Figure 4.12 shows, even after proper motion selection background stars contaminate the Pleiades sample due to the measurement dispersion in the POSS astrometry. The success of the proper motion search and degree of field contamination must be properly gauged using independent observations that further distinguish field stars from Pleiades members.

Although the Pleiades cluster is likely to be dynamically evolved, on a stellar age scale its members are relatively young. As such, young stars in clusters exhibit characteristics which differ from older stars in the Galactic disk. Due to their relative youth Pleiades members are expected to be rotating more rapidly than field stars of similar type, generating chromospheric activity via a magnetic dynamo mechanism whereby excitation collisions from magnetic heating ionize certain atoms in the chromosphere (see eg. Hawley 1993). Energy escapes through radiation during recombination, such as hydrogen emission including the distinct Balmer line at 6563 Å. Strong chromospheric activity can differentiate Pleiades members from older, less chromospherically active field stars (Prosser, Stauffer, & Kraft 1991; Steele & Jameson 1995; Hawley,

Gizis, & Reid 1996). In addition, the absorption of both Na I and K I doublets will distinguish Pleiades M dwarfs from field giants (Kirkpatrick, Henry & McCarthy 1991).

This chapter describes the use of optical spectroscopy as a tool to discriminate between obvious field stars and cluster members, and discusses the relevant spectral features with regards to the success of the Pleiades proper motion search.

5.2 Observations and Data Reduction

This section describes the observational program to measure the optical spectra of Pleiades candidates using the Hydra fiber-fed spectrograph on the 3.5 m WIYN telescope[1] (Barden et al. 1994) at Kitt Peak National Observatory.

5.2.1 Hardware setup

Since spectra for a large number of candidates were needed to accurately assess the field star contamination in the Pleiades sample, I chose an optimal combination of resolution, exposure time, and wavelength coverage to obtain spectra of several hundred candidates. A suitable wavelength region for accomplishing the goals of the spectroscopic study is 6000 – 9000 Å which covers both Hα and Na I spectral regions as well as several molecular absorption bands such as TiO, VO, and CaOH useful for classifying M dwarf spectra (Kirkpatrick, Henry & McCarthy 1991). I chose to observe faint stars in the sample since field contamination is worst at the faint end, $R \sim 16 - 20$ ($K_s \sim 11 - 14$). At this resolution, WIYN can image stars in this brightness range at SNR ≥ 10 using an exposure time on the order of 1 hour. The probable members in the spectroscopic survey generally are expected to be dwarf spectral types M2 – M6.

[1]The WIYN Observatory is a joint facility of the University of Wisconsin-Madison, Indiana University, Yale University, and the National Optical Astronomy Observatories.

Observations were taken on the nights of November 25 – 28, 1999. The weather was photometric or otherwise generally clear enough for spectroscopy. Less than 2 hours were lost due to weather. The Hydra spectrograph was configured with the red cable and 600@13.9 grating yielding a dispersion of 1.4 Å/pixel over a wavelength region $\sim$ 6100 – 8900 Å. The imaging camera contained the T2KC 2048 $\times$ 2048 CCD array detector configured to read out the portion of the chip that detected the spectra, resulting in images that were 1200 $\times$ 2048 pixels in size. The electron gain was 1.7 e^-/ADU and the RMS read noise was $\sim$ 5 e^-.

5.2.2 Selection of fields and targets

The Hydra spectrograph on WIYN is capable of imaging $\sim$ 100 spectra of sources spanning a circular field approximately 1° in diameter. I selected a number of fields close to the cluster center in order to obtain many spectra of probable members as well as observe a sample of spectroscopic standard reference Pleiades stars with known spectral types (Steele & Jameson 1995). Several fields outside the cluster core were targeted in order to cover the gap in the HHJ search and to measure the success of my proper motion search at large radial distances. Additionally, a field in the Praesepe cluster was observed to obtain several spectral standards from Allen & Strom (1995).

Several field stars formed a control sample. The field stars were selected as having similar colors to the Pleiades candidates with large proper motion, but in a different direction than the cluster, greater than 3"/cent. from the cluster in the VPD depicted in Figure 4.9. Unused fibers were assigned to blank sky positions or parked altogether. At least 10 – 20 sky spectra were taken in each exposure.

Table 5.1 lists the WIYN fields that were ultimately observed, along with the number of candidates and control stars observed and total exposure time used in each field. Individual objects were prioritized in the following order: standards, high probability candidates, low probability candidates, and field stars. Specific fiber assignment was done by the NOAO Hydra simulation software which optimized fiber

placement. All or most high probability candidates and control stars within the suitable dynamic range of brightness in each field were in fact observed. The location of these fields compared to the positions of high probability Pleiades candidates is displayed in Figure 5.1. Note that 128 candidates were observed more than once in fields that overlap. In total the program observed 528 Pleiades candidates and 120 control stars.

In a typical night, 9 "zero" exposures for bias subtraction were taken. For each field setup, about 5 comparison spectra from a CuAr lamp were taken to calibrate the wavelength scale on the CCD detector as well as about 5 dome flat field exposures. The telescope typically observed 4 – 7 fields per night depending on exposure time. Most fields were observed using 3 exposures to minimize contamination from cosmic rays.

5.2.3 Image reduction

The CCD images were processed and analyzed using the Image Reduction and Analysis Facility[2] (IRAF). Standard bias subtraction was employed using a median bias frame for each night. After bias subtraction of all images, a median comparison spectra frame and median flat field image were computed for each field setup.

A sample Hydra image is displayed in Figure 5.2 showing the spectroscopic dispersion for several stars and sky emission lines. The IRAF software tool package DOHYDRA extracted the spectra from the CCD images. The procedure usually went as follows. The flat field apertures were identified, the dispersion axes were traced, and the apertures were fit using polynomial functions. DOHYDRA integrated the photon counts over the apertures and extracted the flat field spectra. Using the fits for the flat field apertures, spectra for the wavelength comparison images and object images were extracted by aperture sums, and divided by the flat field spectra. Sky emission

[2]IRAF is distributed by the National Optical Astronomy Observatories, which is operated by the Association of Universities for Research in Astronomy, Inc., under contract with the National Science Foundation.

Table 5.1: Coordinates for WIYN Hydra spectrograph fields with the number of Pleiades candidates, field control sources, and exposure time. The field in Praesepe is also listed.

Mid-exposure (2000 UT)	RA (J2000)	DEC	Candidates	Control	Exp. time (min.)
Nov 26 02:48	03 44 50	+24 32 47	43	0	90
Nov 26 05:23	03 44 54	+23 36 20	33	4	90
Nov 26 08:14	03 47 00	+24 06 00	49	3	90
Nov 26 10:34	03 49 01	+23 39 56	23	3	90
Nov 26 12:38	08 40 31	+19 43 38	...	...	30
Nov 27 02:42	03 42 53	+24 03 53	48	4	90
Nov 27 04:47	03 47 07	+23 11 31	37	6	90
Nov 27 07:44	03 51 09	+24 09 15	20	1	90
Nov 27 09:49	03 48 50	+24 37 33	37	2	90
Nov 27 11:56	04 00 04	+23 49 00	17	6	30
Nov 28 02:38	03 50 49	+25 05 01	18	2	90
Nov 28 04:40	03 51 08	+23 11 37	13	6	90
Nov 28 07:13	03 43 06	+23 07 36	35	6	60
Nov 28 08:44	03 44 26	+25 29 21	31	6	60
Nov 28 10:54	03 58 24	+21 42 00	12	5	60
Nov 29 02:39	03 31 40	+26 12 00	10	5	45
Nov 29 03:56	03 34 48	+25 24 00	12	12	45
Nov 29 05:47	03 40 24	+25 27 33	31	9	45
Nov 29 07:00	03 49 24	+21 47 05	13	9	45
Nov 29 08:54	03 54 00	+19 42 00	7	9	30
Nov 29 09:54	03 38 47	+23 59 57	31	11	45
Nov 29 11:45	03 56 24	+26 42 00	8	4	45

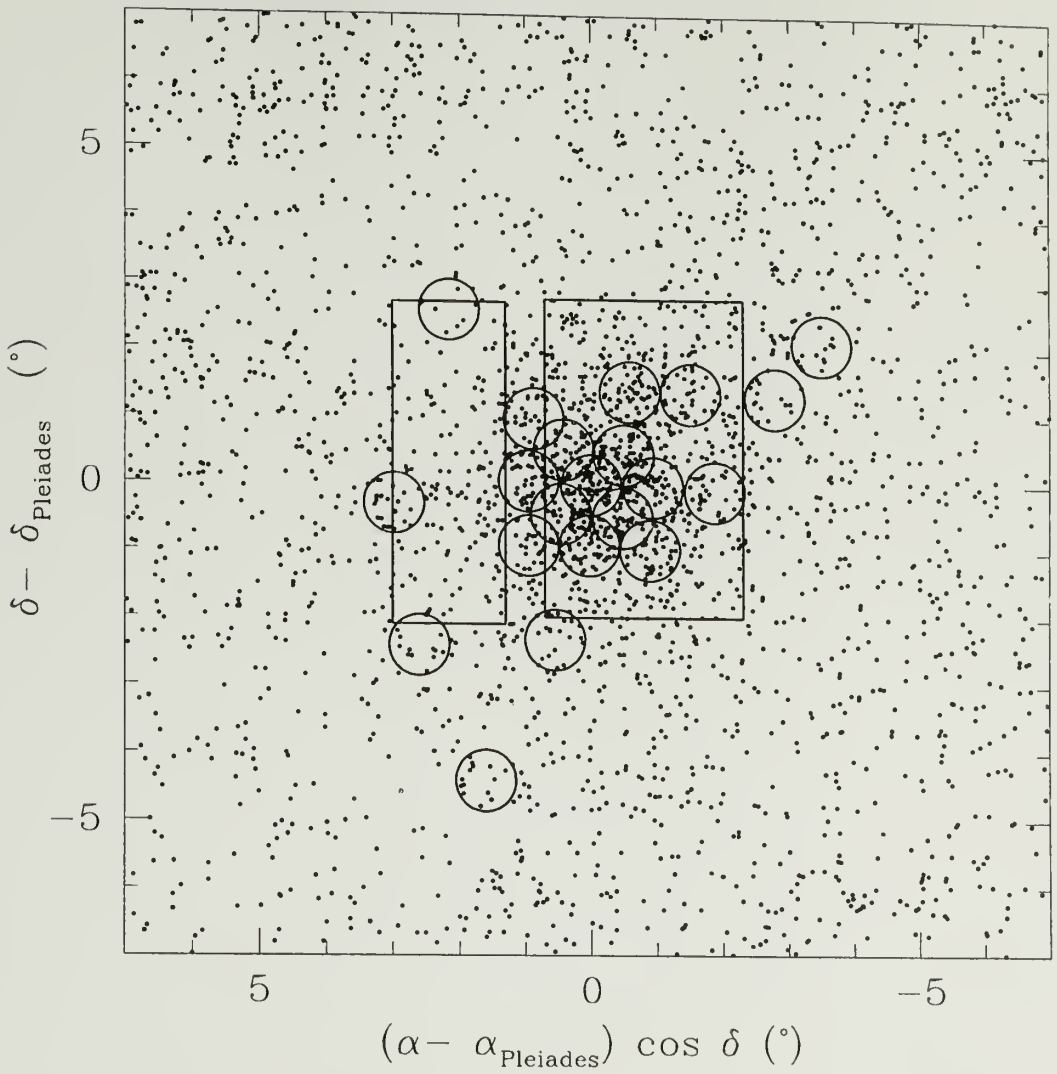

Fig. 5.1.— WIYN fields (circles) in the Pleiades chosen for multi-object spectroscopic observations. The number of high probability Pleiades candidates in each field varied from 60 or more near the cluster to 10 or less in the outer parts. The boxed regions indicate the area covered by the HHJ proper motion search (Hambly, Hawkins, & Jameson 1993).

lines were subtracted from the object spectra. The comparison spectra were calibrated by iterating on the location of identifiable emission lines using a list of highly precise line wavelengths for the CuAr lamp. Finally, the wavelength calibration was applied to the object spectra.

5.3 Results

Figure 5.3 displays several extracted spectra of new low mass Pleiades candidates. Several features in the spectra are identified, including the Hα emission line at 6563 Å, several TiO absorption bands, and the Na I absorption doublet at 8190 Å. These features are extremely useful in classifying the spectra and determining their likelihood of cluster membership.

5.3.1 Distribution of Ha EW strength

Figure 5.4 displays the Hα emission found in several new Pleiades candidates. I use the equivalent width (EW) of the line as a measure of Hα emission strength. Physically, the EW depends on the temperature and pressure of the emitting gas, doppler broading, and the number of atoms in the particular state of transition. The EW can be measured by fitting the line profile with a function, such as a gaussian or lorentzian. The FITPROFS tool in IRAF fit the profiles with a gaussian function in automated fashion over a fitting region 6555 – 6569 Å. I then later manually checked many of the spectra using the SPLOT tool which will fit the EW for individual spectra.

Figure 5.5 shows the distribution of Hα EW ($W_{\mathrm{H}\alpha}$) for the 528 Pleiades candidates as well as the 121 control sources in the spectroscopic survey. The shaded region indicates the $W_{\mathrm{H}\alpha}$ measurements for probable members identified by previous studies that were recovered in this study. The difference between the cluster and field

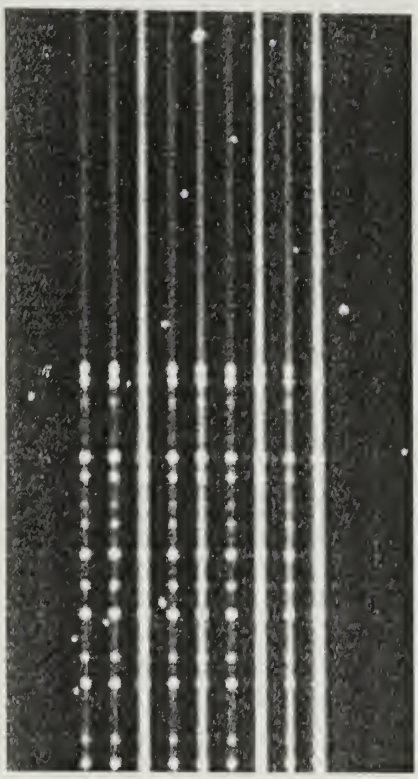

Fig. 5.2.— Sample CCD image taken through the Hydra spectrograph for several apertures. The spectral dispersion (vertical) is 1.4 Å/pixel.

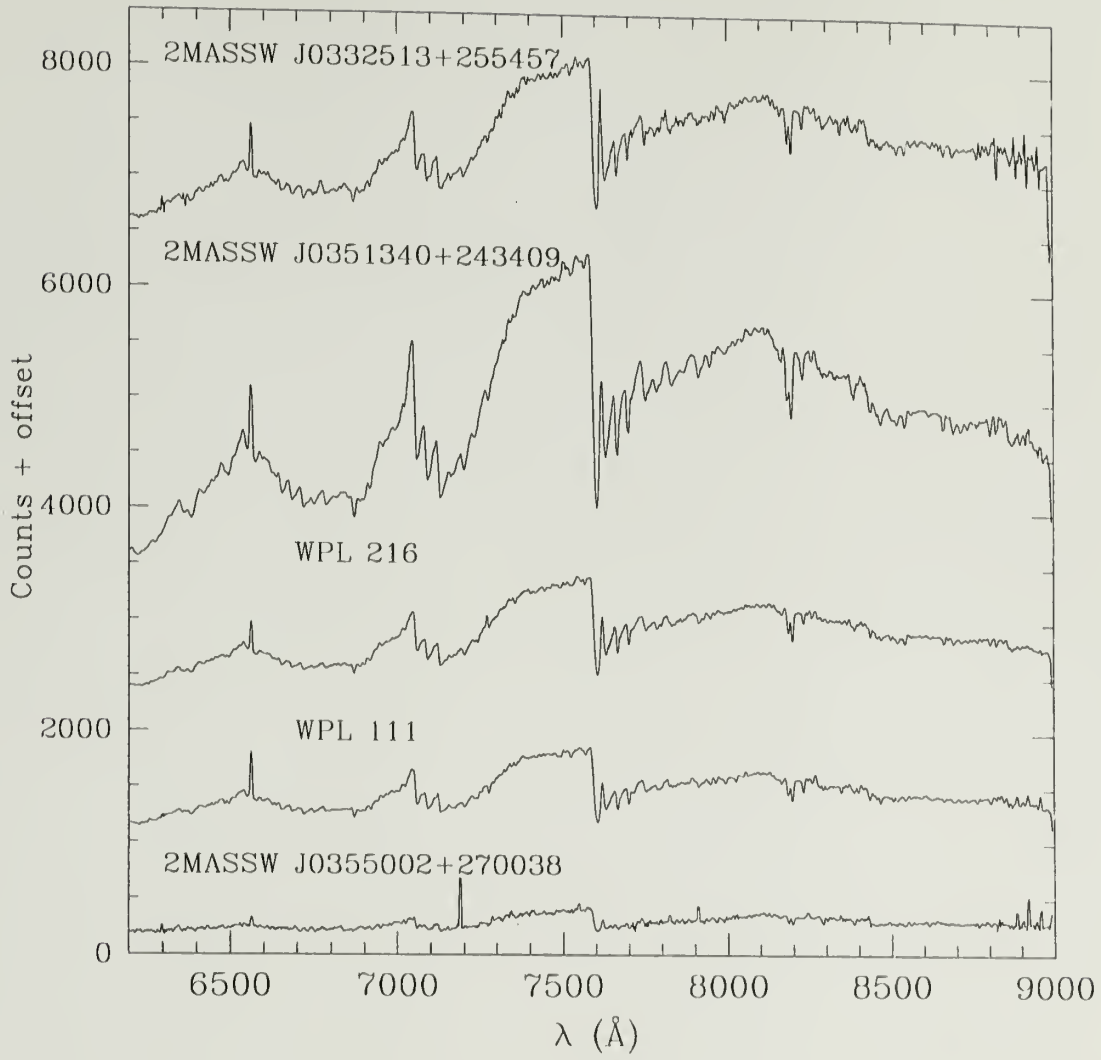

Fig. 5.3.— Spectra for a few new Pleiades candidates extracted from the WIYN Hydra images. Hα emission is clearly evident at 6563 Å, as well as the Na I doublet at 8183/8195 Å. TiO and CaH absorption bands, characteristically strong for stars of these types, are obvious in the regions near $\sim$ 6700, 7200, and 7700 Å.

distributions was assessed using a χ^2 test for two sets of binned data of total points R and S (*Numerical Recipies*, p. 623)

$$\chi^2 = \sum_i \frac{(\sqrt{S/R}R_i - \sqrt{R/S}S_i)^2}{R_i + S_i}$$

where

$$R \equiv \sum_i R_i \quad S \equiv \sum_i S_i$$

The number of degrees of freedom for this problem is the number of bins minus one, or 18. A value $\chi^2 = 227.1$ indicates that there is less than a 0.5% chance that the candidate sample and the control sample are derived from the same distribution function. However, about 75 Pleiades candidates in the spectroscopic sample do not show Hα emission, indicating that a fraction of our overall sample contains field stars.

Table 5.2 shows the statistical dependence of $W_{\rm H\alpha}$ with respect to proper motion membership probability, K_s magnitude, and radial distance. As expected the contamination is worst at large radial distance and at faint magnitudes. For sources with $p \geq 0.01$ in the magnitude range $11 \leq K_s \leq 14$ within 5° of the cluster center I estimate the overall contamination to be about 13%. One should expect lower a contamination level for brighter stars due to their relatively lower surface density in the field. Outside a 5° radius one can expect the contamination to dominate the sample.

The sample of 121 field stars contained 104 M dwarfs that had spectral types similar to the Pleiades candidates, M2 – M6. 29 of the 104 objects had $W_{\rm H\alpha} >$ 1 Å, and 18 had $W_{\rm H\alpha} > 3$ Å. Although our sample is too small to determine the dMe fraction (fields stars that show Hα emission due to chromospheric activity) as a function of spectral type, and assuming that stars with $W_{\rm H\alpha} > 1$ Å are indeed dMe stars, we note that our 28% dMe rate in the M2 – M6 range agrees well with the data given in Hawley, Gizis, & Reid (1996). Thus from the 70 Pleiades candidates in the

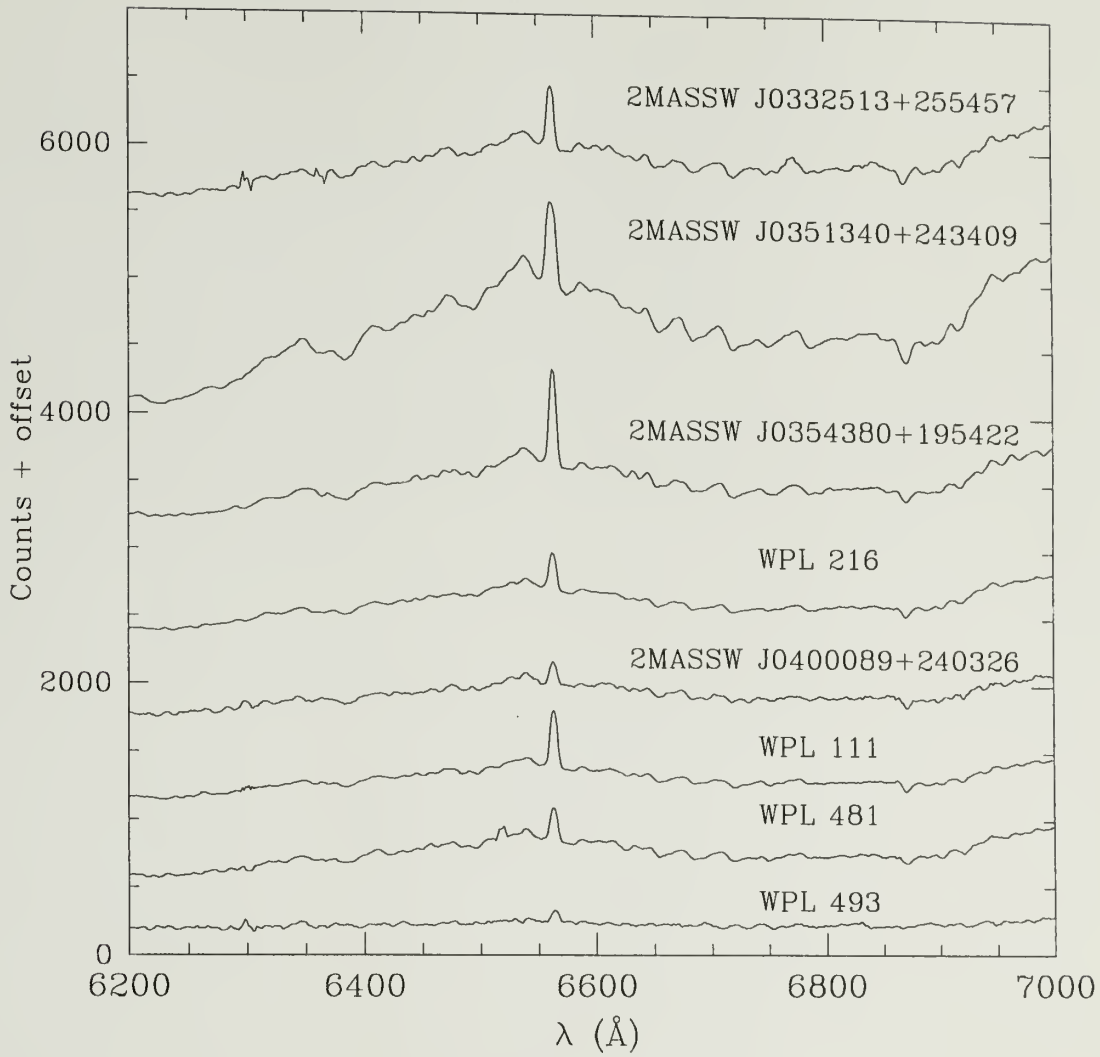

Fig. 5.4.— The Hα spectral region for a small sample of emitters in the Pleiades spectroscopic study. These spectra have been smoothed for this plot.

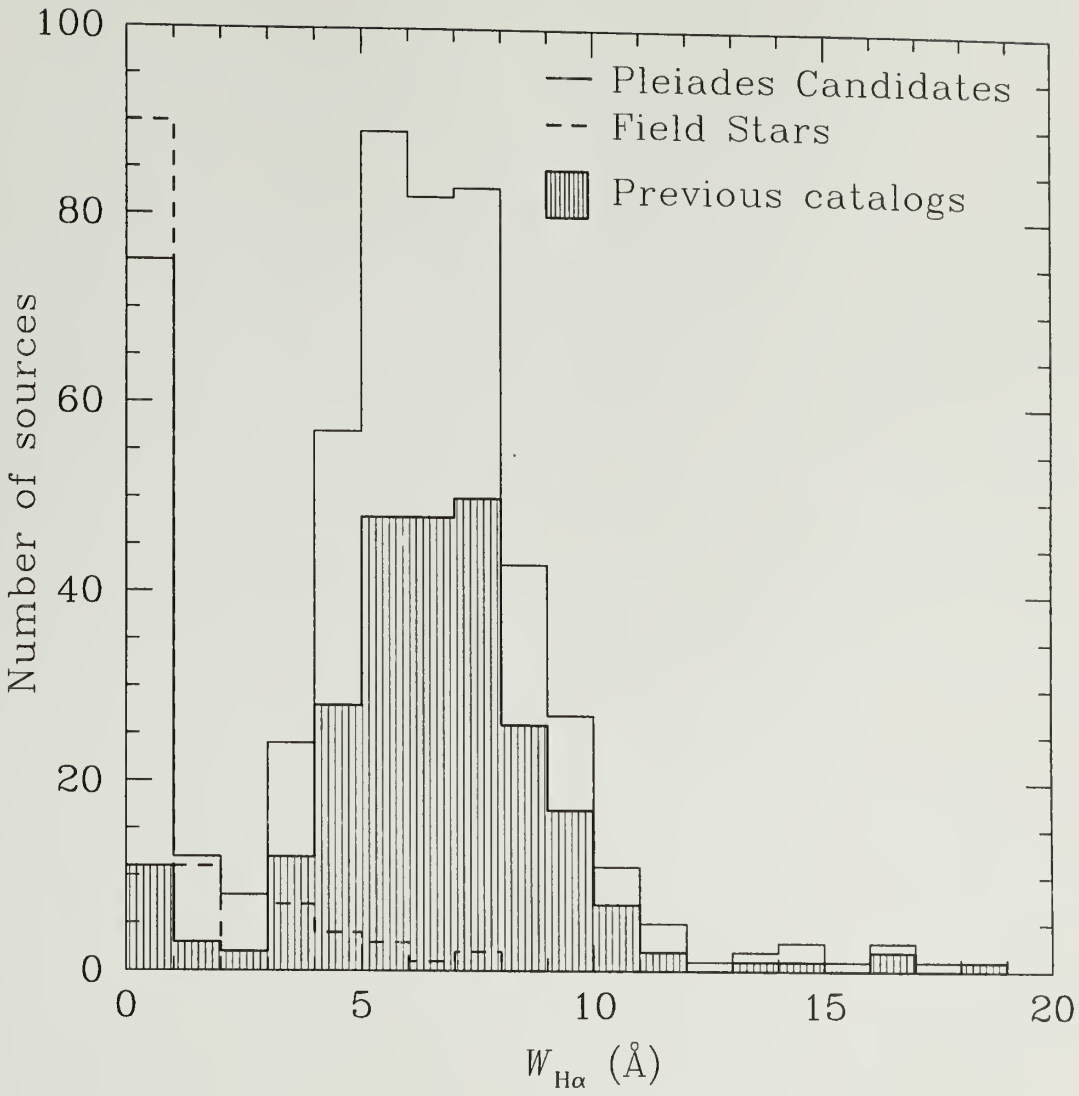

Fig. 5.5.— Histogram of Hα equivalent widths $W_{H\alpha}$ for all sources in the Pleiades spectroscopic study. The shaded region indicates the fraction of our sample identified by previous Pleiades studies. The distribution for the control sample is given by the dashed line.

range M2 – M6 that presumably are not members ($W_{\rm H\alpha} < 1$ Å) we can infer roughly 27 dMe stars in the sample of 434 with $W_{\rm H\alpha} > 1$ Å, or a contamination of 6%.

The Pleiades proper motion search described in Chapter 4 has recovered over 92% of the HHJ sample. The search has also discovered 269 candidates with $p \geq 0.3$ that were in the HHJ survey area but not in their list. The spectra for 109 of these candidates show that 83% have Hα emission consistent with cluster membership ($W_{\rm H\alpha}$ = 3 – 14), while 94% of HHJ stars in our list have Hα emission consistent with cluster membership. Thus while this survey appears to be more complete than HHJ, it is also more contaminated. If 83% of the 269 new objects in the HHJ region are in fact Pleiades members, then the HHJ survey is 66% complete relative to a total 663 objects in their sensitivity range, in good agreement with their completeness estimation of 70%.

5.3.2 Near-infrared colors of the Pleiades lower main sequence

As evident in Figure 5.3, the relatively cool temperatures of M dwarfs cause the condensation of molecules and dust in their atmospheres. Optical spectra of the Pleiades M dwarfs show a plethora of molecular absorption regions, mainly due to TiO and CaH. VO absorption becomes prominent for later M types (Kirkpatrick, Henry & McCarthy 1991). In the near-infrared, H_2O and H_2 produce heavy absorption features. These features cause broad-band colors to deviate from the predicted colors of a simple thermal blackbody spectrum. Thus modelling the colors of M dwarfs is complex. Current models include recently determined molecular line lists, non-grey atmospheres, and dust. The input physics to these models requires good empirical data for calibration. A star cluster such as the Pleiades represents an ideal laboratory for stellar physics since presumably the stars share a common age, distance, and chemical composition.

Figure 5.6 shows a $K_s : J - K_s$ color-magnitude diagram for selected probable Pleiades members with $p > 0.3$ and $W_{\rm H\alpha} = 3$ – 14 Å, and the remainder of the 1087

Pleiades candidates with $p > 0.3$ within 5° of the cluster center. Note the apparent shift blueward in the $J - K_s$ colors in the $K_s = 12 - 13$ range due to collisional-induced absoprtion of molecular hydrogen (Baraffe et al. 1997). Below $K_s = 13$, the colors appear to become redder again. For comparison, a 120 Myr solar metallicity isochrone from Baraffe et al. (1998), transformed into the 2MASS photometric filter system using a 2MASS-CIT transformation (J. Carpenter, priv. comm.), is overlaid and adjusted to the distance and reddening of the Pleiades. I used a distance modulus of 5.5 and reddening $E(B-V) = 0.05$ (Lyngå 1987) along with the reddening laws $E(J-H) = 0.37E(B-V)$, $E(H-K) = 0.19E(B-V)$, and $A_K = 0.37E(B-V)$ from Bessell & Brett (1988). The isochrone appears to fit best on bottom of the main sequence, mid-M type dwarfs near $K_s = 14$, and appears slightly blue for brighter, early M type dwarfs stars. Part of the poor fit may be attributed to the metallicity of the Pleiades, which could be slightly higher than solar metallicity.

Figure 5.7 displays the $J-H : H-K_s$ colors for the sample described in Figure 5.6 and provides a diagnostic to analyze the Pleiades sample without invoking a distance modulus. The Baraffe et al. (1998) models appear to be slightly bluer that early M dwarf colors, again uncorrected for metallicity. Also drawn are the approximate color for dwarfs and giants from the system of Bessell & Brett (1988), showing that nearly all high probability Pleiades candidates are indeed late type dwarfs by photometric, proper motion, and spectroscopic selection.

5.3.3 Chromospheric activity

Stauffer, Liebert & Giampapa (1995) and Hodgkin, Jameson & Steele (1995) using HHJ stars have detected that $W_{\mathrm{H}\alpha}$ increases with decreasing mass in the Pleiades and eventually peaks at $I \approx 14$, $V - I \approx 3$. I have followed up this observation with a large sample of probable Pleiades members.

Figure 5.8 shows the trend in $W_{\mathrm{H}\alpha}$ with J magnitude for 318 sources with $p > 0.3$ and $W_{\mathrm{H}\alpha} = 3 - 14$ Å. The J magnitude range shown represents a mass range

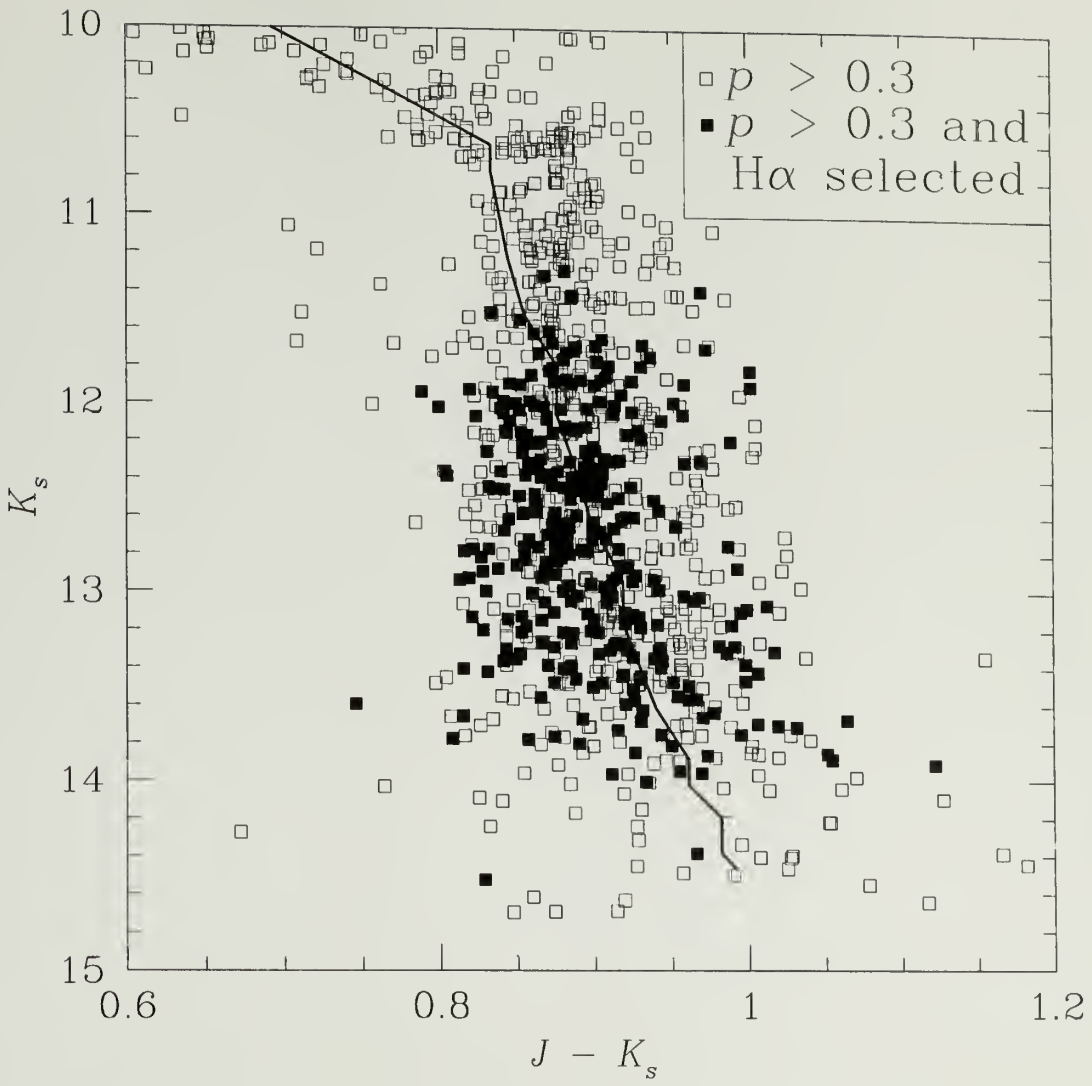

Fig. 5.6.— $K_s : J - K_s$ color magnitude diagram for Pleiades candidates with $p > 0.3$ (open squares) and those with $W_{\mathrm{H}\alpha} = 3$ –14 Å (solid squares). The solid line indicates a 120 Myr solar metallicity isochrone from Baraffe et al. (1998) adjusted to the distance and reddening of the Pleiades.

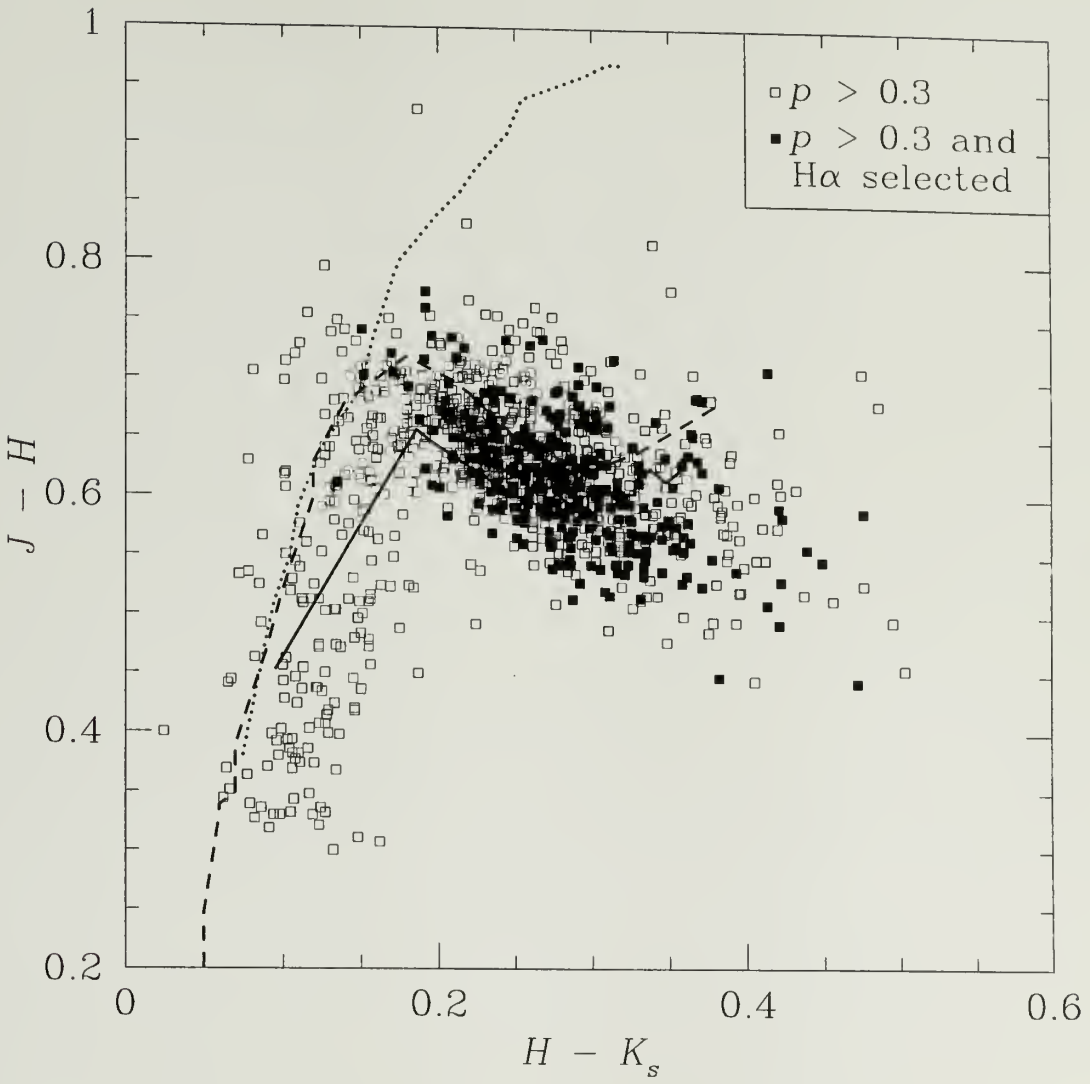

Fig. 5.7.— $J - H : H - K_s$ color-color diagram for Pleiades candidates with $p >$ 0.3 (open squares) and those with $W_{\mathrm{H}\alpha} = 3$ –14 Å (solid squares). The solid line indicates a 120 Myr solar metallicity isochrone from Baraffe et al. (1998) adjusted to the reddening of the Pleiades. Also shown are approximate colors for dwarfs (dashed line) and giants (dotted line) from Bessell & Brett (1988), uncorrected for photometric system.

approximately 0.5 – 0.08 $M_{\odot}$. HHJ stars are distinguished as solid squares. The dispersion is large, presumably due to intrinsic scatter and variability. Figure 5.8 shows no increase in $W_{H\alpha}$ with decreasing mass.

Both Stauffer et al. (1995) and Hodgkin et al. (1995) interpreted this absence of increasing $W_{H\alpha}$ with decreasing mass as possible evidence for reduced magnetic dynamo efficiency due to the fully convective nature of stars below 0.3 $M_{\odot}$. Rotation also contributes to chromospheric activity, since Hyades members massive enough to have undergone evolutionary spindown have in general lower chromospheric activity than Pleiades counterparts of similar mass. However, below the hydrogen burning limit, even some rapidly rotating stars have low chromospheric activity (Tinney & Reid 1998; Hawley 1999) while others have been observed to flare (Liebert et al. 1999). Thus a problem of current interest is to understand the the breakdown of the dynamo mechanism in very low mass objects.

Two objects showed evidence for flaring. WPL 403 (SK 316) showed a change in $W_{H\alpha}$ from 4 to 28 Å and a flux increase of a factor of 10 between 2 successive nights. The successive spectra are plotted in Figure 5.9. The He I emission at 6678 Å and emission at the Ca II triplet at 8498/8542/8662 Å confirms that the increase in Hα emission was indeed due to a flaring event, since Ca II absorption and an absence of He I emission are observed in the quiescent state. Otherwise no obvious flaring was detected in the remainder of the stars with repeat observations. A flare appears to have occurred on WPL 395 (HCG 355) during one observation with $W_{H\alpha} = 20$ Å. This event also produced He I and Ca II emission lines, shown in Figure 5.10. Table 5.3 summarizes the EWs for the chromospheric lines during quiesence and flaring for WPL 403 and WPL 395.

5.3.4 Spectral types, Na I widths, and K I widths

Spectral typing provides a convenient, straightforward stellar classification sequence. Several thorough papers have pioneered the use of spectral indices as a

Table 5.2: Number of Pleiades candidates distributed in $W_{H\alpha}$ bins (in Å) according to membership probability p, K_s magnitude, and radial distance r from the cluster center.

Group	0-1	1-3	3-5	5-7	7-9	9-11	> 11
$0.001 \leq p \leq 0.01$	22	0	3	5	1	0	0
$0.01 \leq p \leq 0.1$	19	3	10	18	10	3	3
$0.1 \leq p \leq 0.3$	11	6	12	17	17	6	4
$0.3 \leq p \leq 1.0$	27	8	56	131	98	29	9
$11 \leq K_s \leq 12$	3	2	14	27	15	1	0
$12 \leq K_s \leq 13$	33	2	17	85	69	23	7
$13 \leq K_s \leq 14$	29	8	46	55	38	14	7
$14 \leq K_s \leq 15$	14	5	4	4	4	0	2
$0° \leq r \leq 1°$	14	5	33	84	62	20	8
$1° \leq r \leq 2°$	35	6	31	61	48	11	6
$2° \leq r \leq 3°$	11	2	11	14	12	5	0
$3° \leq r \leq 4°$	15	3	4	10	3	2	2
$4° \leq r \leq 5°$	3	1	2	2	1	0	0
$5° \leq r \leq 6°$	1	0	0	0	0	0	0

Table 5.3: SPLOT EWs in Å for lines in the WPL 395 and WPL 403 spectra. Note that EWs correspond to emission except the Ca II lines in WPL 403 (quiescent) which were in absorption.

object	Hα	He I	Ca II 8498	Ca II 8542	Ca II 8662
WPL 395 (flaring)	20.1	2.0	2.0	1.7	1.2
WPL 403 (flaring)	28.1	3.3	1.0	1.1	0.5
WPL 403 (quiescent)	4.2	< 1	0.4	0.9	0.7

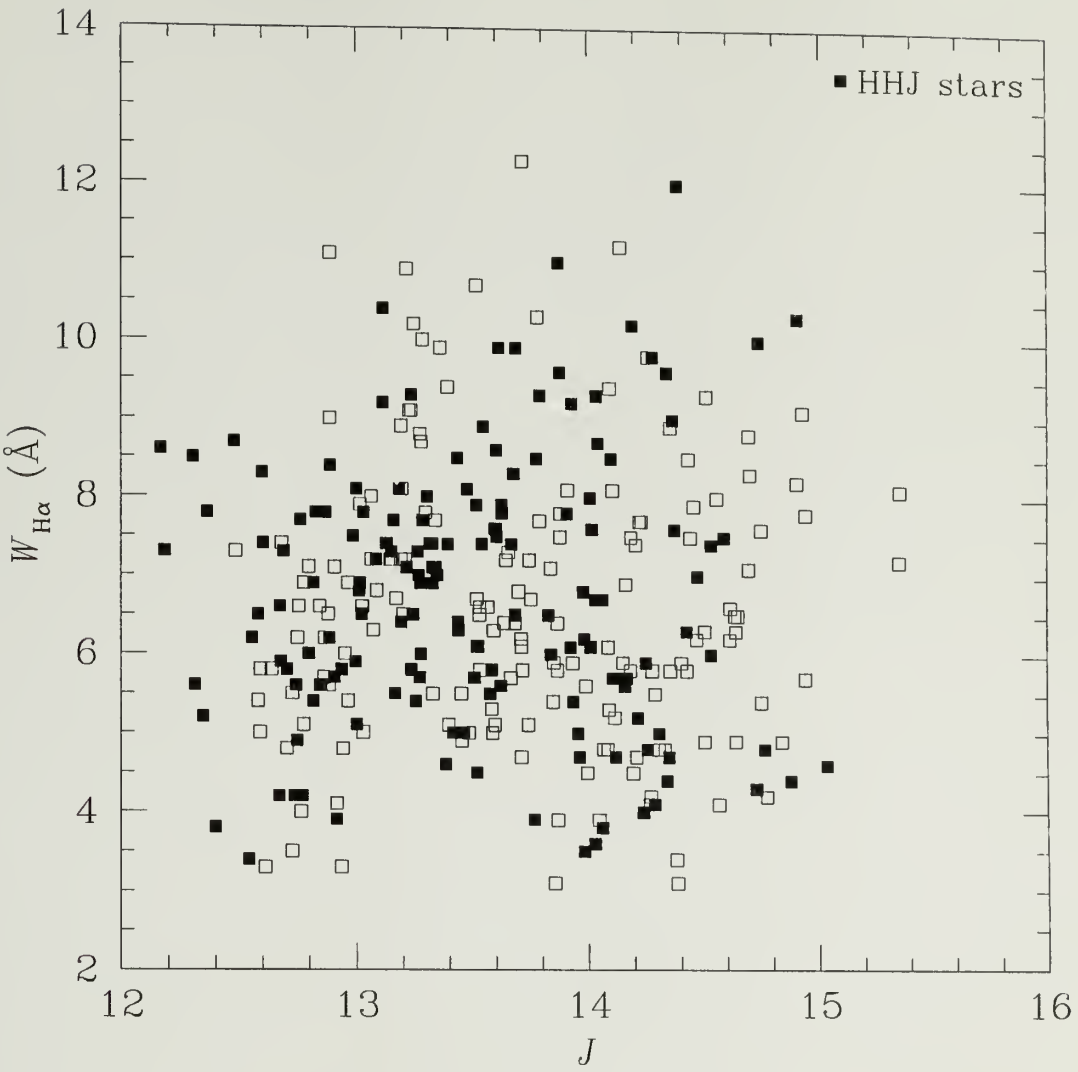

Fig. 5.8.— $W_{H\alpha}$ *vs.* J magnitude for 318 probable Pleiades members with $p > 0.3$ and $W_{H\alpha} = 3 - 14$ Å. The J magnitude range shown represents a mass range approximately $0.5 - 0.08$ $M_{\odot}$. HHJ stars are distinguished as solid squares.

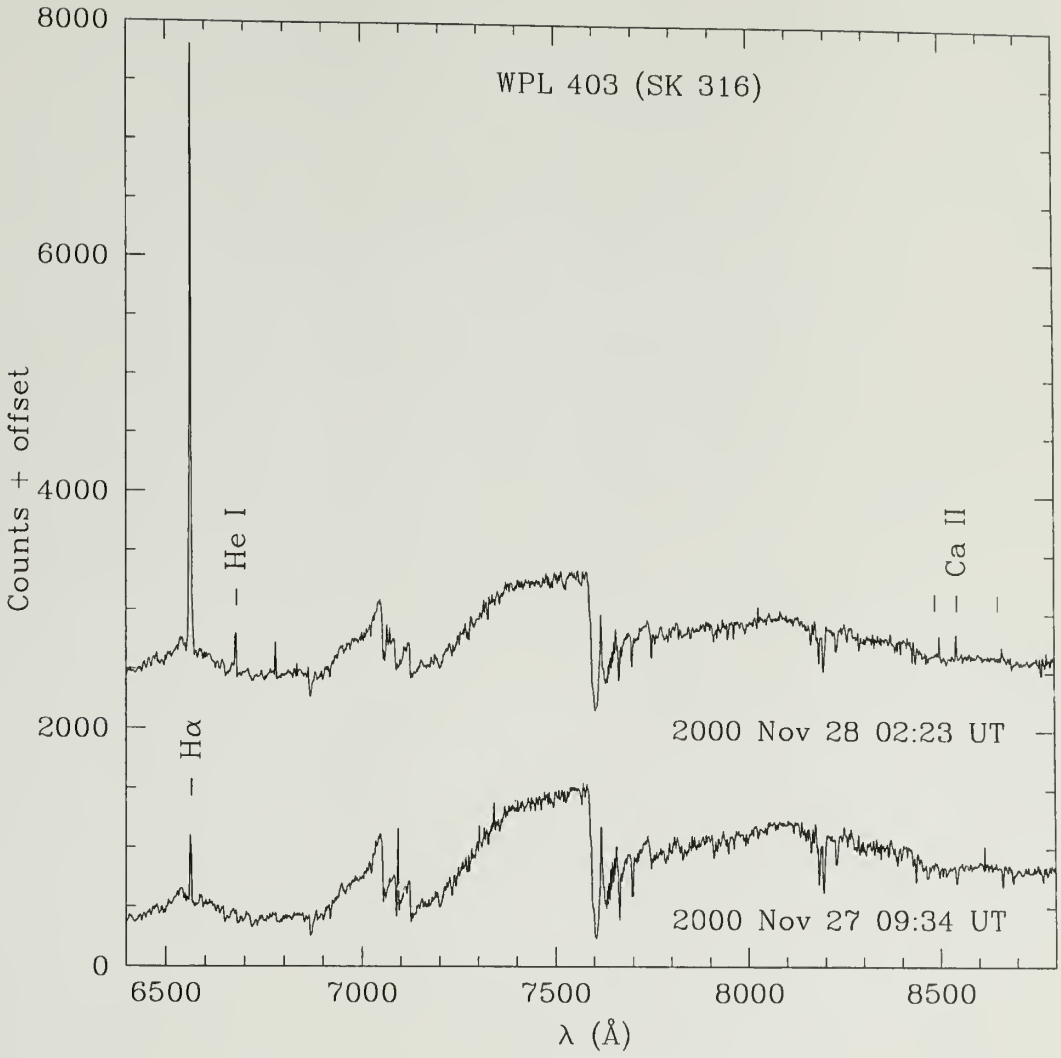

Fig. 5.9.— Spectra for WPL 403 (SK 316) on two successive nights. The tremendous increase in Hα strength and emission lines corresponding to He I and Ca II suggest that the object was undergoing a flare event on 2000 November 28 02:23 UT.

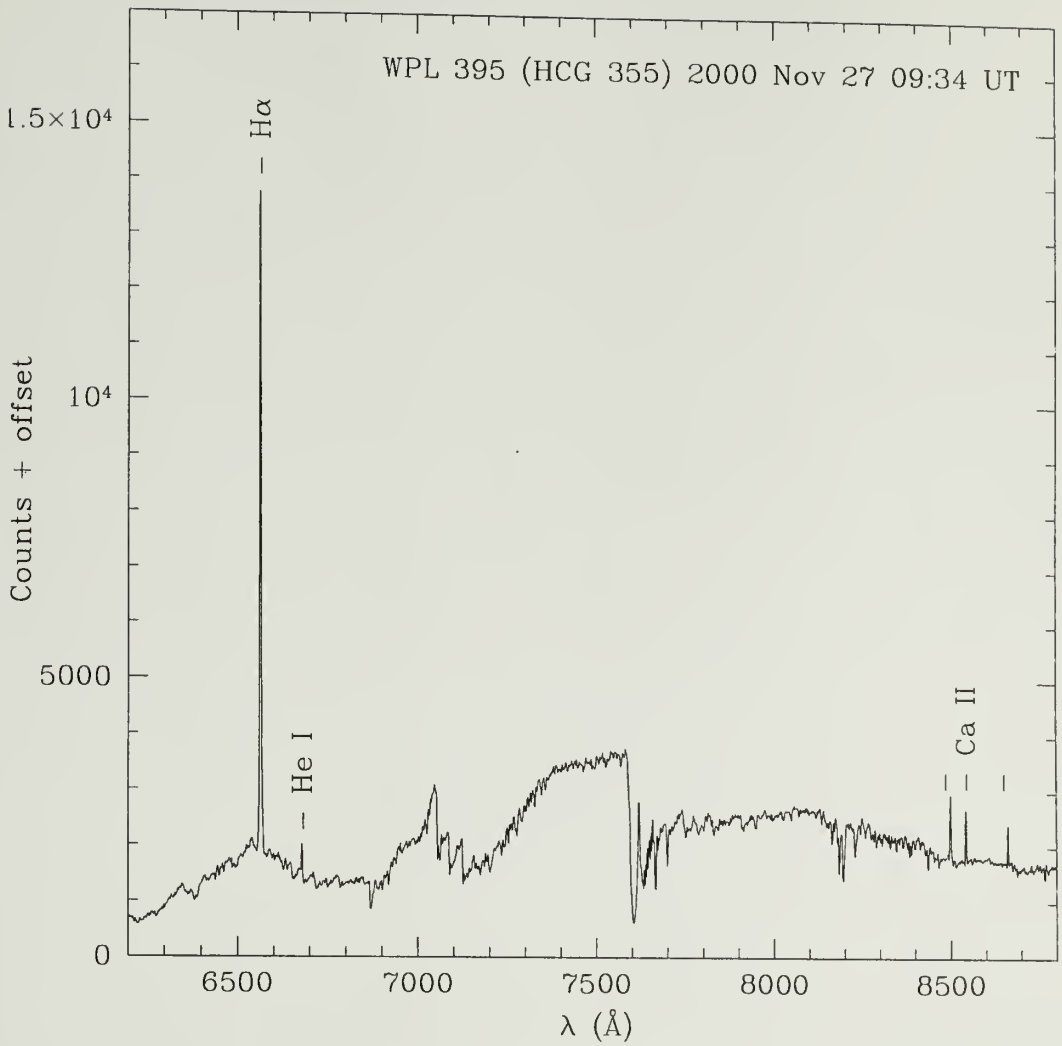

Fig. 5.10.— Spectrum for WPL 395 (HCG 355) during an apparent flare. Note emission lines similar to those produced in the WPL 403 flare (Figure 5.9).

technique to quantify the spectral sequence of M dwarfs in the Pleiades and the field. For example, Kirkpatrick et al. (1991) used the ratio of certain "continuum" points to absorption features, such as CaH, Ti I, Na I , and Ca II. These ratios are sensitive to various types of K and M dwarfs and can therefore can be used to define a sequence of spectral indices for classification. Hamilton & Stauffer (1993) used several TiO and VO features to define spectral indices. Prosser et al. (1991) defined several similar, broad spectral regions to measure the depth of absorption features due to TiO, CaH, and CaOH relative to the "continuum."

In this work, I utilize several of the ratios in Prosser et al. (1991) that are the most sensitive to spectral type in the spectral range of this spectroscopic study, roughly M2 – M6. Spectral index regions were defined as R2 (6507 – 6598 Å); R3 (6635 – 6718 Å); R4 (6750 – 6844 Å); and R7 (7000 – 7068 Å). Since each covers tens of angstroms, it is suitable for the relatively low resolution of the WIYN data (1.4 Å/pixel), allowing a large statistical sampling of pixels in each region.

The total instrumental flux for each region was determined with the Hα line clipped in R2, and the ratios R3/R2, R4/R2, and R4/R7 were computed for all spectral standards observed during the WIYN observations. The 5 highest and lowest pixel values in each region were rejected to elimate spurious emission, such as cosmic rays or errant sky lines. The spectral standards observed, measured indices and fitted spectral types are listed in Table 5.4. Figure 5.11 shows the results with the spectral classes given by Steele & Jameson (1995). Also shown are the best least squares fit to the mean indices and original fits from Prosser et al. (1991). The fits are given as follows:

$$M_{R3/R2} = -14.10 \left(\frac{R3}{R2}\right) + 13.08$$

$$M_{R4/R2} = -20.68 \left(\frac{R4}{R2}\right) + 18.12$$

$$M_{R4/R7} = -10.14 \left(\frac{R4}{R7}\right) + 11.61$$

Note that a negative M class implies spectral class K, such that K7 = -1, K6 = -2, etc. Using these fits, the ratios were computed for all stars in this spectroscopic study. The final spectral class was determined by averaging the types corresponding to the flux ratios and rounding off to the nearest half spectral type. The similarity of the fits from Prosser et al. (1991) indicate that one may extrapolate to earlier types, which should only be necessary for a small number of field stars. In general the fitted spectral types are accurate to within 0.5 – 1 type with a larger error at the faint end, as Table 5.4 shows. Repeated observations taken with different WIYN setups yield an error in the indices of $\sim 0.01 - 0.04$.

Equivalent widths for the Na I 8183/8195 Å and K I 7665/7699 Å resonance doublets were extracted for all object spectra using FITPROFS over a fitting region of 8180 – 8200 Å and 7662 – 7705 Å respectively. M dwarf spectra also contain the Ca II triplet 8498/8542/8662 Å but these lines were generally too weak (< 1 Å) to be very useful. The total EWs were computed by summing the widths of the individual doublet absorption lines. Figure 5.12 shows the relations between luminosity and $W_{\rm NaI}$ and $W_{\rm KI}$ for highly probable Pleiads. Note the increase in $W_{\rm NaI}$ with decreasing luminosity and mass. A complete list of Pleiades candidates with identifications, positions, proper motion membership probabilities, spectral types, and Hα, Na I, and K I EWs is given in Table 5.5. The sources in this table have been cross-correlated with the CfA Open Cluster Database and the HHJ catalog. Cross-identifications are given in Table 5.6.

Table 5.4: Spectral standards in the Pleiades and Praesepe used to calibrate indices. Previous spectral types were published in Allen & Strom (1995), Steele & Jameson (1995) and Stauffer, Schultz, & Kirkpatrick (1998). Index regions were defined in Prosser, Stauffer, & Kraft (1991). Duplicate observations were taken with different WIYN setups, where dates are 2000 UT. Spectral types from this work were determined from fitting the index ratios to the published spectral type (see text for details). IDs adopted from Haro, Chavira, & Gonzalez (1982); Jones & Stauffer (1991); Hambly, Hawkins, & Jameson (1993); and Bouvier et al. (1998).

ID	Pub. M type	R3/R2	R4/R2	R4/R7	M type
JS 313	3.0	0.654	0.731	0.785	3.5
JS 365	3.0	0.695	0.741	0.841	3.0
JS 390	3.0	0.712	0.747	0.871	3.0
HHJ 427	3.0	0.746	0.740	0.886	2.5
HHJ 336 (Nov 26 08:14)	3.5	0.631	0.651	0.729	4.0
HHJ 336 (Nov 26 10:34)	3.5	0.632	0.669	0.751	4.0
HCG 375, HHJ 250 (Nov 27 09:49)	4.5	0.635	0.608	0.818	4.0
HCG 375, HHJ 250 (Nov 27 07:44)	4.5	0.658	0.649	0.801	4.0
HCG 125, HHJ 298	4.5	0.613	0.662	0.730	4.5
HHJ 139	4.5	0.595	0.669	0.688	4.5
HCG 135, HHJ 229 (Nov 27 02:42)	4.5	0.647	0.653	0.766	4.0
HCG 135, HHJ 229 (Nov 26 05:23)	4.5	0.656	0.671	0.737	4.0
HHJ 59	5.0	0.596	0.637	0.686	4.5
HHJ 101	5.0	0.574	0.599	0.657	5.0
HCG 346, HHJ 111	5.0	0.599	0.662	0.672	4.5
HHJ 23	5.0	0.619	0.698	0.643	4.5
HHJ 37	5.0	0.565	0.653	0.609	5.0
HHJ 58	5.0	0.567	0.659	0.645	5.0
HHJ 54	5.0	0.568	0.613	0.663	5.0
HHJ 257	5.0	0.610	0.651	0.687	4.5
HHJ 36	5.0	0.632	0.709	0.735	4.0
HHJ 48	5.0	0.652	0.712	0.614	4.0
HHJ 12	5.5	0.540	0.602	0.566	5.5
HHJ 16 (Nov 27 04:47)	5.5	0.599	0.654	0.619	4.5
HHJ 16 (Nov 26 10:34)	5.5	0.583	0.653	0.660	4.5
HHJ 7	6.0	0.491	0.657	0.487	6.0
HHJ 2	6.5	0.506	0.627	0.574	6.0
CFHT-PL-10	6.5	0.387	0.496	0.428	7.5

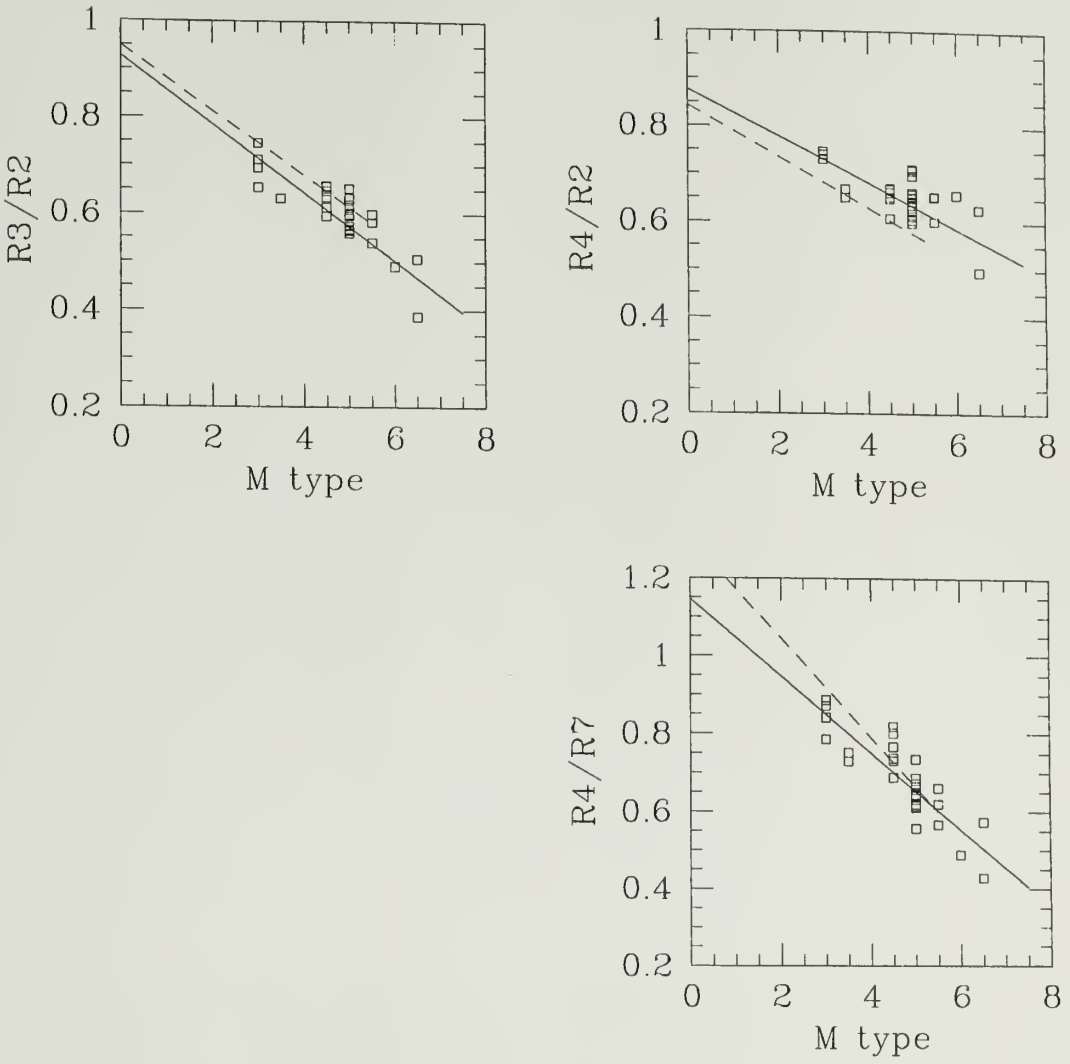

Fig. 5.11.— Calibration of spectral types using Pleiades spectral standards in Table 5.4. Solid lines represent best least squares fits to the mean index at each type. Broken lines illustrate the original relations from Prosser et al. (1991), showing that extrapolation of the fit to earlier types is probably valid.

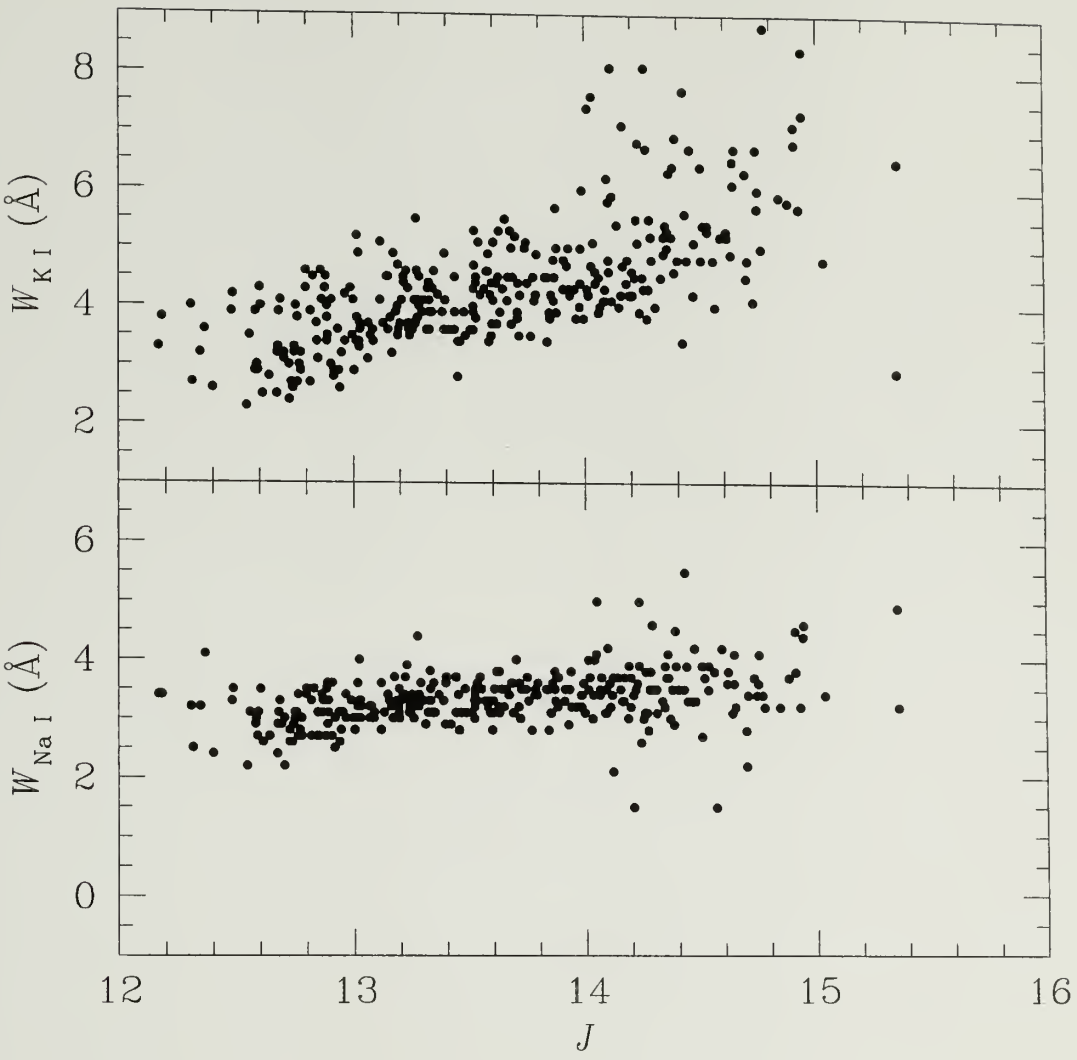

Fig. 5.12.— Na I and K I EWs *vs.* J for 318 Pleiades candidates with $p > 0.3$ and $W_{\rm H\alpha} = 3 - 14$ Å.

Table 5.5: Identifications, preliminary 2MASS positions, membership probabilities, spectral types and EWs (in Å) for all 528 Pleiades candidates in this spectroscopic study. $W_{H\alpha}$ corresponds to emission and W_{NaI} and W_{KI} correspond to absorption. A spectral type of '?' indicated low signal to noise, often with difficulty in measuring spectral lines.

ID (this work)	RA (J2000)	DEC	p	M type	$W_{H\alpha}$	W_{NaI}	W_{KI}
WPL 001	03 30 37.45	+26 20 45.9	0.42	4.5	4.5	3.7	4.2
WPL 002	03 31 09.76	+26 11 13.6	0.32	3.0	< 1	2.4	2.3
WPL 003	03 31 24.20	+25 51 32.8	0.41	4.0	< 1	3.0	2.2
WPL 004	03 31 29.58	+26 30 12.6	0.51	4.0	5.3	3.3	4.9
WPL 005	03 32 42.32	+26 04 38.0	0.26	4.0	1.5	2.6	2.0
WPL 006	03 32 44.29	+25 51 47.6	0.17	3.0	< 1	2.9	2.2
WPL 007	03 32 51.36	+25 54 57.1	0.51	4.0	5.9	3.8	4.3
WPL 008	03 33 35.59	+25 13 55.8	0.41	3.5	3.1	4.5	4.6
WPL 009	03 33 41.89	+26 20 25.8	0.07	3.5	< 1	2.4	2.5
WPL 010	03 33 42.07	+26 06 39.8	0.32	4.5	1.2	3.3	5.5
WPL 011	03 33 43.58	+26 02 54.0	0.01	4.0	5.3	4.6	6.4
WPL 012	03 34 13.46	+25 25 25.7	0.48	4.5	6.1	3.6	4.4
WPL 013	03 34 21.68	+25 02 24.9	< 0.01	4.0	0.0	3.2	2.9
WPL 014	03 35 04.69	+25 50 48.4	0.33	5.0	8.3	3.4	4.8
WPL 015	03 35 08.78	+25 05 54.9	0.44	4.0	5.6	3.1	3.4
WPL 016	03 35 39.79	+25 38 45.7	0.52	3.5	< 1	3.5	2.5
WPL 017	03 35 49.66	+25 04 48.4	0.47	2.5	3.3	2.6	2.5
WPL 018	03 35 50.27	+25 42 21.1	0.47	4.0	9.0	2.9	3.4
WPL 019	03 35 51.21	+25 30 17.6	0.02	4.0	3.1	3.1	4.7
WPL 020	03 36 05.31	+25 21 03.9	0.51	4.0	5.5	3.1	3.6
WPL 021	03 36 16.00	+25 15 21.1	< 0.01	3.5	< 1	2.2	2.1
WPL 022	03 36 42.45	+25 19 26.8	0.49	4.5	8.8	2.2	4.5
WPL 023	03 37 07.19	+23 55 00.2	0.50	4.0	2.6	3.2	3.9
WPL 024	03 37 07.73	+23 42 05.4	0.01	3.5	0.2	2.4	3.3
WPL 025	03 37 31.05	+23 46 07.5	0.33	5.5	5.8	5.5	7.7
WPL 026	03 38 02.02	+24 20 15.4	0.52	4.0	10.4	2.8	4.1
WPL 027	03 38 02.41	+23 54 35.6	0.43	3.5	4.9	2.8	3.4
WPL 028	03 38 06.90	+24 14 56.0	0.22	≥6.5	9.9	4.4	1.8
WPL 029	03 38 13.02	+23 37 21.2	0.06	4.5	10.8	3.1	7.5
WPL 030	03 38 15.34	+23 40 04.7	< 0.01	2.5	< 1	3.0	1.8
WPL 031	03 38 18.34	+24 16 26.2	0.09	≥6.5	< 1	3.9	< 1
WPL 032	03 38 20.25	+23 41 42.2	< 0.01	3.0	< 1	2.4	2.2
WPL 033	03 38 24.22	+25 19 49.5	0.49	4.5	3.1	3.6	4.2
WPL 034	03 38 27.50	+25 30 18.3	0.02	6.0	6.0	2.9	6.6
WPL 035	03 38 34.18	+23 43 07.6	0.44	3.5	3.6	3.0	4.7
WPL 036	03 38 34.47	+23 40 22.7	0.50	4.5	8.0	3.5	4.3
WPL 037	03 38 43.29	+25 22 27.5	0.52	4.0	7.3	3.4	3.8
WPL 038	03 38 45.75	+24 28 04.3	0.38	5.0	7.6	3.7	4.2
WPL 039	03 38 46.08	+25 16 42.7	< 0.01	4.0	0.1	2.1	2.2
WPL 040	03 38 54.79	+24 11 43.3	0.30	3.0	< 1	3.7	< 1
WPL 041	03 39 09.85	+23 58 53.2	0.31	≥6.5	14.7	< 1	7.5
WPL 042	03 39 13.30	+25 43 50.0	0.51	4.5	7.4	3.5	4.0
WPL 043	03 39 22.06	+24 02 39.7	0.22	4.0	< 1	4.2	< 1
WPL 044	03 39 22.64	+25 14 05.5	0.09	3.5	0.2	2.9	2.0

Table 5.5 (continued)

ID (this work)	RA (J2000)	DEC	p	M type	$W_{\mathrm{H}\alpha}$	W_{NaI}	W_{KI}
WPL 045	03 39 28.96	+25 34 56.0	0.21	4.0	4.9	2.9	3.1
WPL 046	03 39 32.32	+24 16 01.6	0.39	4.0	7.2	3.3	3.6
WPL 047	03 39 39.33	+24 14 03.6	0.41	5.0	< 1	2.3	5.4
WPL 048	03 39 42.70	+23 54 27.6	0.52	4.0	7.7	3.3	4.0
WPL 049	03 39 45.41	+23 56 37.3	0.01	4.0	5.0	0.9	1.4
WPL 050	03 39 46.32	+23 58 52.8	0.50	3.0	5.8	3.0	3.1
WPL 051	03 39 47.96	+23 50 56.7	0.43	3.0	7.3	2.9	4.1
WPL 052	03 39 48.49	+23 46 04.0	0.49	4.5	8.7	4.1	4.6
WPL 053	03 39 48.50	+24 10 35.9	< 0.01	0.0	0.0	1.9	1.8
WPL 054	03 39 55.20	+24 12 54.8	0.47	2.0	3.4	2.9	6.4
WPL 055	03 39 57.85	+25 55 30.1	0.46	5.0	7.7	3.9	5.1
WPL 056	03 40 01.83	+25 04 20.1	0.35	5.0	9.2	3.5	5.0
WPL 057	03 40 05.95	+25 40 21.5	0.48	4.5	5.8	3.8	4.1
WPL 058	03 40 07.09	+24 13 03.9	0.52	4.5	9.0	3.0	6.3
WPL 059	03 40 10.68	+25 49 30.5	0.46	4.5	4.8	3.7	4.0
WPL 060	03 40 11.02	+25 23 27.1	0.43	4.5	6.0	3.5	4.5
WPL 061	03 40 11.91	+25 52 32.8	0.03	5.0	5.4	3.8	4.4
WPL 062	03 40 18.81	+23 54 23.9	0.48	4.0	5.7	3.4	4.1
WPL 063	03 40 23.04	+25 29 48.1	0.51	4.0	6.2	3.1	3.5
WPL 064	03 40 25.61	+24 06 00.8	0.47	4.0	16.6	3.5	4.4
WPL 065	03 40 26.40	+24 05 24.3	0.22	2.5	5.3	2.5	2.7
WPL 066	03 40 26.95	+24 14 14.7	0.37	4.5	7.4	3.6	4.9
WPL 067	03 40 31.16	+25 08 53.1	0.37	4.5	8.3	3.5	4.3
WPL 068	03 40 32.58	+25 28 40.9	0.12	5.0	8.0	3.6	4.5
WPL 069	03 40 40.31	+25 50 48.3	0.47	4.0	8.0	3.2	3.1
WPL 070	03 40 54.67	+25 17 50.8	0.10	3.0	0.3	2.4	2.0
WPL 071	03 40 55.73	+24 01 45.4	0.28	3.5	0.0	2.2	2.0
WPL 072	03 40 59.26	+25 11 55.7	0.51	5.5	7.5	4.2	5.2
WPL 073	03 41 00.37	+24 13 35.3	< 0.01	4.5	7.7	3.2	4.3
WPL 074	03 41 05.21	+23 50 15.5	0.32	5.5	6.3	4.1	6.5
WPL 075	03 41 10.25	+25 45 56.5	0.50	4.0	6.6	3.0	3.4
WPL 076	03 41 14.70	+22 53 10.4	< 0.01	4.5	< 1	3.1	3.7
WPL 077	03 41 19.32	+23 51 42.1	0.39	4.5	7.7	3.4	4.2
WPL 078	03 41 19.84	+25 06 49.6	0.26	4.5	4.1	3.1	3.7
WPL 079	03 41 22.42	+24 23 52.1	0.49	5.0	11.2	3.7	5.4
WPL 080	03 41 22.85	+23 55 48.5	0.51	4.0	9.3	3.2	3.6
WPL 081	03 41 24.67	+25 23 06.1	0.45	4.5	4.7	3.2	3.8
WPL 082	03 41 25.96	+23 15 36.2	0.25	4.5	8.8	3.4	4.6
WPL 083	03 41 26.36	+23 08 03.1	0.13	4.0	7.6	4.1	4.4
WPL 084	03 41 26.86	+24 01 02.7	0.49	4.5	7.8	4.1	3.6
WPL 085	03 41 31.18	+24 03 25.2	0.29	5.0	7.5	3.6	5.1
WPL 086	03 41 31.76	+24 18 02.3	< 0.01	3.5	< 1	3.0	2.2
WPL 087	03 41 33.72	+25 06 48.8	0.32	3.5	6.8	3.0	3.4
WPL 088	03 41 33.88	+23 11 45.4	< 0.01	5.5	0.9	3.8	8.5

Table 5.5 (continued)

ID (this work)	RA (J2000)	DEC	p	M type	$W_{\mathrm{H}\alpha}$	W_{NaI}	W_{KI}
WPL 089	03 41 37.26	+25 08 33.0	0.51	4.5	5.6	3.2	3.7
WPL 090	03 41 38.83	+24 23 09.6	0.37	4.5	6.5	3.1	4.9
WPL 091	03 41 43.71	+23 08 00.3	0.23	5.5	3.9	2.5	8.0
WPL 092	03 41 46.64	+23 01 20.0	0.01	4.5	8.3	3.2	3.9
WPL 093	03 41 48.50	+25 34 29.9	0.08	4.0	1.3	4.3	2.8
WPL 094	03 41 48.94	+23 03 23.7	< 0.01	5.0	5.3	3.6	5.0
WPL 095	03 41 52.94	+24 07 25.4	0.52	4.0	5.0	3.1	4.0
WPL 096	03 41 53.31	+25 41 07.6	< 0.01	3.5	0.1	2.9	2.5
WPL 097	03 41 54.19	+25 43 47.0	0.41	3.5	5.6	2.9	2.6
WPL 098	03 41 58.65	+22 57 02.1	0.40	3.5	4.9	3.1	3.2
WPL 099	03 42 02.34	+23 19 37.4	0.16	3.0	< 1	2.7	3.5
WPL 100	03 42 03.41	+25 22 39.3	0.51	4.5	7.4	3.8	4.4
WPL 101	03 42 03.53	+25 19 18.0	0.09	5.0	4.9	2.6	6.0
WPL 102	03 42 08.28	+25 37 00.5	0.50	4.5	6.5	4.0	4.9
WPL 103	03 42 10.98	+25 44 35.5	0.13	5.5	7.6	3.7	6.2
WPL 104	03 42 13.47	+24 18 49.9	0.29	5.0	8.8	3.4	5.6
WPL 105	03 42 15.36	+23 11 31.3	0.06	5.0	8.1	3.5	4.6
WPL 106	03 42 17.86	+24 06 58.0	0.49	4.5	6.5	3.5	4.5
WPL 107	03 42 20.50	+23 18 25.5	0.34	3.5	< 1	2.6	2.5
WPL 108	03 42 26.22	+23 51 39.1	0.48	$\geq$6.5	< 1	2.1	1.8
WPL 109	03 42 26.26	+24 14 08.0	0.35	4.5	8.0	2.9	4.1
WPL 110	03 42 33.61	+22 57 36.5	< 0.01	1.5	< 1	2.5	2.1
WPL 111	03 42 33.94	+24 11 01.0	0.52	5.0	8.9	3.7	5.3
WPL 112	03 42 34.00	+23 24 52.2	0.05	5.5	4.2	3.4	5.8
WPL 113	03 42 36.94	+23 39 14.6	< 0.01	4.5	4.1	3.0	4.7
WPL 114	03 42 36.95	+25 13 57.9	0.49	3.0	< 1	5.8	< 1
WPL 115	03 42 38.36	+25 28 44.4	0.43	5.0	9.3	3.7	5.4
WPL 116	03 42 41.19	+24 01 43.1	0.39	4.0	6.2	3.2	4.4
WPL 117	03 42 41.86	+24 00 15.9	0.50	4.0	5.0	3.1	3.4
WPL 118	03 42 42.12	+25 11 49.0	0.50	5.5	12.0	3.9	6.9
WPL 119	03 42 43.81	+25 32 06.2	0.44	3.5	4.2	2.6	2.7
WPL 120	03 42 44.29	+23 16 24.2	0.45	4.0	1.1	3.5	3.6
WPL 121	03 42 44.34	+23 06 16.6	0.51	4.5	9.6	3.7	5.0
WPL 122	03 42 44.43	+23 58 15.7	0.28	4.5	7.0	3.5	4.4
WPL 123	03 42 45.62	+23 49 23.1	0.31	5.0	9.6	3.9	5.2
WPL 124	03 42 47.78	+25 33 35.0	0.18	4.5	5.7	3.0	3.4
WPL 125	03 42 48.88	+23 34 48.9	0.49	4.5	7.4	3.4	4.5
WPL 126	03 42 49.11	+24 10 15.9	0.46	3.0	5.8	2.7	2.8
WPL 127	03 42 53.30	+23 31 07.7	0.36	4.0	6.8	3.1	3.4
WPL 128	03 42 56.53	+22 51 18.4	0.27	5.0	6.4	1.8	5.2
WPL 129	03 42 56.58	+24 13 45.9	0.50	4.0	8.1	3.5	4.8
WPL 130	03 43 01.27	+24 14 52.7	0.40	4.5	7.7	3.6	5.5
WPL 131	03 43 02.65	+22 52 45.4	0.37	3.5	< 1	2.6	2.4
WPL 132	03 43 04.36	+25 26 12.4	0.49	4.5	9.3	3.6	4.9

Table 5.5 (continued)

ID (this work)	RA (J2000)	DEC	p	M type	$W_{H\alpha}$	W_{NaI}	W_{KI}
WPL 133	03 43 04.40	+22 49 36.4	0.11	3.5	< 1	2.6	2.3
WPL 134	03 43 07.57	+25 34 29.5	0.48	4.0	6.3	3.2	3.5
WPL 135	03 43 11.56	+24 06 52.2	0.51	5.5	8.5	3.6	5.8
WPL 136	03 43 11.57	+25 25 23.3	0.32	4.5	3.3	3.1	3.6
WPL 137	03 43 12.07	+24 44 45.3	0.51	4.5	6.5	3.0	3.9
WPL 138	03 43 13.38	+24 11 00.8	0.49	4.0	4.1	1.5	4.0
WPL 139	03 43 16.59	+23 50 02.1	0.37	4.0	6.9	3.5	4.1
WPL 140	03 43 16.71	+23 12 52.4	< 0.01	4.0	< 1	2.4	2.5
WPL 141	03 43 18.00	+22 59 59.6	< 0.01	3.5	< 1	2.7	3.6
WPL 142	03 43 19.01	+22 47 10.7	0.19	4.5	14.2	3.5	4.8
WPL 143	03 43 20.50	+24 26 34.9	0.33	6.0	2.8	3.9	4.0
WPL 144	03 43 21.02	+24 11 08.8	0.35	6.5	4.0	2.6	3.9
WPL 145	03 43 22.55	+23 00 56.9	0.09	5.5	6.2	3.8	6.8
WPL 146	03 43 25.15	+22 53 44.7	0.02	4.5	5.6	3.2	3.8
WPL 147	03 43 26.44	+22 42 42.8	0.05	4.0	5.5	3.2	3.3
WPL 148	03 43 26.89	+24 27 09.6	0.46	4.0	5.2	3.2	3.2
WPL 149	03 43 27.41	+23 18 07.5	0.05	4.5	7.8	3.8	6.0
WPL 150	03 43 28.15	+24 53 31.2	0.41	4.0	6.6	3.3	3.3
WPL 151	03 43 28.64	+24 09 06.1	0.49	5.5	4.7	2.1	4.1
WPL 152	03 43 29.82	+24 39 23.7	0.44	5.0	5.9	3.0	4.5
WPL 153	03 43 34.14	+25 02 17.0	0.29	5.0	8.4	3.1	5.6
WPL 154	03 43 34.46	+25 36 14.7	0.09	5.0	2.0	3.6	5.0
WPL 155	03 43 35.20	+25 24 31.2	0.50	3.5	4.2	2.8	3.0
WPL 156	03 43 36.57	+23 12 34.4	0.05	4.5	9.7	3.6	4.7
WPL 157	03 43 36.66	+25 47 00.7	0.48	3.5	11.1	3.1	3.5
WPL 158	03 43 37.11	+23 38 32.4	0.35	4.0	7.1	3.5	4.6
WPL 159	03 43 39.04	+23 44 05.6	0.50	4.5	7.2	3.4	4.5
WPL 160	03 43 39.72	+23 41 32.8	0.36	4.0	7.4	3.5	5.3
WPL 161	03 43 42.88	+25 51 37.1	0.45	4.5	5.7	3.2	4.6
WPL 162	03 43 43.13	+24 32 56.4	0.46	4.5	6.1	3.5	4.3
WPL 163	03 43 43.50	+24 12 50.3	0.51	4.0	6.3	3.5	3.4
WPL 164	03 43 44.07	+25 39 49.9	0.22	4.5	4.7	3.4	4.1
WPL 165	03 43 44.96	+23 03 21.3	0.47	3.0	4.2	2.4	2.5
WPL 166	03 43 48.44	+25 02 37.3	0.58	4.5	6.2	3.6	4.0
WPL 167	03 43 51.73	+24 14 16.2	0.38	3.5	8.7	3.4	4.1
WPL 168	03 43 52.78	+25 29 30.9	0.47	4.0	5.7	3.1	3.6
WPL 169	03 43 56.70	+24 59 36.9	0.52	2.5	3.8	2.4	2.6
WPL 170	03 43 56.98	+23 57 06.0	0.60	4.0	7.3	3.3	4.1
WPL 171	03 43 57.26	+24 13 20.5	0.52	4.0	9.1	3.3	4.3
WPL 172	03 44 01.67	+23 51 46.4	0.10	4.0	4.8	3.4	4.2
WPL 173	03 44 05.23	+24 05 51.5	0.06	3.0	< 1	2.9	2.8
WPL 174	03 44 09.32	+23 08 46.9	0.02	4.0	7.5	3.3	3.7
WPL 175	03 44 09.59	+24 35 22.9	0.52	3.0	4.1	2.5	2.8
WPL 176	03 44 10.75	+25 37 38.7	0.45	4.5	7.4	3.3	4.3

Table 5.5 (continued)

ID (this work)	RA (J2000)	DEC	p	M type	$W_{\mathrm{H}\alpha}$	W_{NaI}	W_{KI}
WPL 177	03 44 10.95	+24 48 46.2	0.09	4.0	5.5	3.1	4.4
WPL 178	03 44 11.27	+24 52 34.6	0.37	4.5	4.4	3.2	4.9
WPL 179	03 44 12.12	+23 52 37.6	0.48	4.0	8.9	3.5	4.2
WPL 180	03 44 13.96	+25 32 15.5	0.51	4.5	7.3	3.5	4.2
WPL 181	03 44 16.46	+23 37 04.2	0.35	4.0	7.7	3.4	3.8
WPL 182	03 44 17.17	+23 08 04.0	< 0.01	3.5	< 1	2.3	2.2
WPL 183	03 44 19.05	+24 35 18.8	0.52	3.5	7.1	3.3	3.9
WPL 184	03 44 20.64	+24 15 11.0	0.47	4.5	5.7	3.7	5.9
WPL 185	03 44 20.87	+23 33 39.9	0.46	3.0	3.9	3.0	2.9
WPL 186	03 44 23.39	+25 21 30.3	0.49	4.5	8.7	3.3	3.9
WPL 187	03 44 24.67	+24 51 53.8	0.50	4.5	7.8	3.5	4.5
WPL 188	03 44 25.07	+25 34 04.2	0.34	5.0	6.1	4.0	7.4
WPL 189	03 44 26.52	+24 29 11.7	0.48	4.0	9.2	3.6	5.1
WPL 190	03 44 27.48	+24 14 17.3	0.51	3.5	5.5	3.2	4.6
WPL 191	03 44 27.89	+24 00 00.0	0.46	4.5	7.9	3.3	6.7
WPL 192	03 44 31.73	+23 35 26.2	0.39	3.5	7.2	3.0	3.6
WPL 193	03 44 32.15	+25 08 12.6	0.51	4.5	4.8	3.1	4.3
WPL 194	03 44 32.31	+25 25 18.3	0.28	$\geq$6.5	3.4	4.3	7.9
WPL 195	03 44 33.06	+25 45 09.7	0.46	4.5	9.9	3.4	4.2
WPL 196	03 44 35.89	+23 34 42.2	0.34	5.0	4.6	3.4	4.8
WPL 197	03 44 37.76	+24 25 39.1	0.50	4.5	6.0	3.9	5.4
WPL 198	03 44 38.94	+23 02 25.6	0.52	4.5	4.6	3.3	3.9
WPL 199	03 44 39.61	+24 31 44.5	0.35	3.0	6.2	3.0	3.3
WPL 200	03 44 46.13	+24 23 03.0	0.50	4.0	4.3	3.7	4.1
WPL 201	03 44 46.47	+24 03 21.8	0.02	2.5	4.0	2.8	2.8
WPL 202	03 44 47.32	+24 00 38.0	0.45	3.5	6.4	3.1	3.5
WPL 203	03 44 47.83	+24 12 52.7	0.50	3.5	7.4	3.1	3.6
WPL 204	03 44 51.25	+23 34 20.8	0.20	4.5	3.1	4.4	6.1
WPL 205	03 44 53.20	+24 01 06.8	0.44	4.0	4.8	3.1	4.1
WPL 206	03 44 53.52	+25 36 19.5	0.20	4.5	1.8	3.2	3.1
WPL 207	03 44 54.08	+24 26 46.9	0.04	3.5	4.9	3.4	3.9
WPL 208	03 44 56.00	+23 55 53.8	0.46	4.0	6.0	3.4	4.3
WPL 209	03 44 56.68	+23 36 23.8	0.22	3.5	7.1	3.3	3.8
WPL 210	03 44 57.32	+23 59 32.7	0.06	3.0	6.9	3.1	3.3
WPL 211	03 44 57.89	+23 20 25.2	0.38	4.0	< 1	3.7	3.4
WPL 212	03 44 58.02	+23 24 31.4	0.37	3.5	6.0	3.2	3.8
WPL 213	03 44 58.58	+23 55 41.3	0.23	3.5	6.0	2.9	3.2
WPL 214	03 44 59.47	+23 21 18.6	0.53	5.0	4.1	4.6	5.2
WPL 215	03 45 01.12	+24 46 41.4	0.45	4.5	8.1	3.5	3.9
WPL 216	03 45 01.19	+25 21 05.9	0.52	4.5	4.5	3.1	3.8
WPL 217	03 45 02.87	+25 05 20.0	0.51	4.5	8.5	3.4	4.5
WPL 218	03 45 05.00	+23 46 06.6	0.23	5.0	7.0	3.5	5.1
WPL 219	03 45 06.55	+24 40 43.1	0.50	4.0	9.8	3.8	5.5
WPL 220	03 45 06.80	+23 36 51.8	0.39	4.5	7.5	3.5	5.1

Table 5.5 (continued)

ID (this work)	RA (J2000)	DEC	p	M type	$W_{\mathrm{H}\alpha}$	W_{NaI}	W_{KI}
WPL 221	03 45 06.91	+23 10 06.7	0.05	2.5	< 1	1.9	2.6
WPL 222	03 45 08.41	+23 25 01.3	0.12	5.0	15.4	4.3	6.1
WPL 223	03 45 09.02	+25 22 30.0	0.25	?	1.7	3.2	< 1
WPL 224	03 45 09.03	+25 32 49.3	0.51	4.0	7.6	3.1	4.4
WPL 225	03 45 10.82	+23 02 58.5	0.33	4.0	10.2	3.4	3.7
WPL 226	03 45 12.07	+24 30 18.4	0.43	3.0	5.5	2.8	3.0
WPL 227	03 45 12.15	+23 21 53.3	0.41	3.5	7.7	3.2	3.8
WPL 228	03 45 13.14	+24 15 23.8	0.44	3.5	3.8	3.4	3.9
WPL 229	03 45 13.41	+23 31 01.0	0.49	4.0	7.1	3.6	4.1
WPL 230	03 45 16.41	+23 34 01.9	0.50	4.5	6.2	4.2	4.2
WPL 231	03 45 16.65	+24 34 33.0	0.47	3.0	5.6	2.5	2.7
WPL 232	03 45 18.30	+24 12 41.6	0.03	2.0	< 1	2.0	2.2
WPL 233	03 45 21.67	+24 32 37.8	0.43	3.5	6.9	3.4	3.8
WPL 234	03 45 24.69	+24 38 47.0	0.04	4.5	8.9	3.8	4.3
WPL 235	03 45 24.78	+24 20 45.5	0.39	3.5	8.1	3.0	3.6
WPL 236	03 45 25.21	+24 54 41.9	< 0.01	3.0	< 1	1.9	2.4
WPL 237	03 45 26.97	+24 13 26.6	0.36	2.5	< 1	2.7	2.2
WPL 238	03 45 27.51	+23 37 57.3	0.52	4.5	5.6	3.3	4.2
WPL 239	03 45 27.73	+23 10 13.5	0.43	2.5	< 1	2.6	2.2
WPL 240	03 45 30.68	+23 02 51.1	0.35	4.5	7.7	5.0	6.8
WPL 241	03 45 33.97	+23 11 06.9	0.51	4.5	7.8	3.7	5.0
WPL 242	03 45 36.72	+24 39 07.1	0.51	4.5	8.5	3.2	4.0
WPL 243	03 45 37.53	+23 10 46.5	0.24	6.5	2.3	< 1	< 1
WPL 244	03 45 39.27	+24 08 20.6	0.52	4.0	6.8	3.4	4.0
WPL 245	03 45 42.85	+23 20 12.6	0.44	4.5	14.6	3.4	4.9
WPL 246	03 45 44.62	+25 23 06.7	0.13	5.0	< 1	2.8	5.7
WPL 247	03 45 49.39	+23 57 06.1	0.46	5.0	7.1	2.8	6.3
WPL 248	03 45 49.92	+23 19 45.1	0.29	6.0	8.6	3.2	7.6
WPL 249	03 45 51.09	+24 26 11.6	0.21	3.5	3.6	3.5	4.9
WPL 250	03 45 51.95	+25 10 02.1	0.51	4.5	8.3	3.6	5.3
WPL 251	03 45 52.73	+23 27 54.5	0.34	3.5	7.0	3.2	3.7
WPL 252	03 45 53.30	+23 08 31.2	0.02	3.0	< 1	2.0	3.0
WPL 253	03 45 54.98	+24 13 26.8	0.35	4.0	6.6	3.1	4.0
WPL 254	03 45 56.96	+23 01 29.3	0.24	4.0	6.0	3.8	4.0
WPL 255	03 45 57.68	+24 03 05.8	0.47	5.0	4.8	3.4	5.0
WPL 256	03 45 57.89	+24 08 41.8	0.36	4.0	5.4	4.1	6.0
WPL 257	03 45 59.17	+23 48 47.2	0.36	4.0	5.4	3.2	4.2
WPL 258	03 46 02.95	+24 40 55.9	0.50	5.0	9.4	4.2	6.2
WPL 259	03 46 03.44	+24 20 57.7	0.14	3.5	8.0	3.2	3.8
WPL 260	03 46 04.28	+23 55 41.6	0.50	3.0	5.4	2.7	2.7
WPL 261	03 46 04.55	+24 09 56.8	< 0.01	4.0	6.8	3.1	4.7
WPL 262	03 46 06.45	+25 25 11.7	0.16	3.0	0.0	2.7	2.1
WPL 263	03 46 07.78	+22 59 00.3	0.36	3.0	< 1	3.0	2.8
WPL 264	03 46 08.69	+24 40 33.5	0.52	4.5	6.6	3.3	4.3

Table 5.5 (continued)

ID (this work)	RA (J2000)	DEC	p	M type	$W_{\mathrm{H}\alpha}$	W_{NaI}	W_{KI}
WPL 265	03 46 12.65	+23 35 14.2	0.48	4.5	6.4	3.5	4.8
WPL 266	03 46 17.93	+24 41 09.7	0.52	2.5	3.4	2.2	2.3
WPL 267	03 46 20.63	+23 53 32.2	0.51	0.5	0.6	0.8	1.3
WPL 268	03 46 21.36	+24 33 52.6	0.41	4.0	3.5	3.4	5.0
WPL 269	03 46 21.38	+23 05 09.5	< 0.01	5.0	5.0	3.5	5.2
WPL 270	03 46 21.61	+23 04 01.3	0.03	5.0	6.5	3.4	5.1
WPL 271	03 46 22.45	+23 29 08.5	0.24	3.5	7.4	3.3	4.4
WPL 272	03 46 23.03	+24 36 18.2	0.16	3.0	4.0	3.2	3.0
WPL 273	03 46 24.11	+24 30 13.1	0.46	5.5	4.2	3.2	8.8
WPL 274	03 46 24.63	+24 28 46.5	0.39	3.5	6.4	3.1	3.9
WPL 275	03 46 27.00	+24 27 14.2	0.46	3.0	5.8	2.6	2.9
WPL 276	03 46 28.17	+22 48 58.2	< 0.01	5.0	0.9	3.9	7.2
WPL 277	03 46 31.01	+23 01 35.0	0.06	5.0	6.1	3.4	4.8
WPL 278	03 46 35.52	+24 01 35.6	0.41	5.0	6.5	3.6	5.0
WPL 279	03 46 36.06	+23 04 17.5	0.35	3.5	8.4	3.3	3.8
WPL 280	03 46 40.02	+23 46 58.8	< 0.01	3.0	5.3	3.0	3.2
WPL 281	03 46 40.40	+22 50 39.9	0.03	4.0	6.3	3.3	4.2
WPL 282	03 46 44.78	+24 44 58.6	0.47	3.0	5.2	3.5	4.5
WPL 283	03 46 46.45	+23 24 03.1	0.25	3.5	< 1	2.7	2.4
WPL 284	03 46 50.08	+23 31 56.4	0.44	4.0	6.5	3.1	3.5
WPL 285	03 46 51.43	+24 06 16.3	0.47	4.5	5.8	3.0	4.4
WPL 286	03 46 52.60	+23 38 43.4	0.52	4.0	8.1	3.3	3.9
WPL 287	03 46 53.96	+24 07 57.4	0.48	4.5	8.1	3.6	4.8
WPL 288	03 46 54.88	+24 28 00.1	0.30	6.5	5.7	4.4	7.3
WPL 289	03 46 55.30	+23 22 49.6	0.46	4.5	5.7	3.7	4.7
WPL 290	03 46 55.77	+23 56 24.4	0.57	4.5	7.1	3.4	4.5
WPL 291	03 46 58.16	+23 33 39.2	0.20	4.0	5.2	3.1	3.8
WPL 292	03 46 58.54	+24 27 40.2	0.42	3.5	7.8	3.2	3.6
WPL 293	03 46 59.31	+24 01 42.9	0.51	4.5	8.1	3.0	4.1
WPL 294	03 46 59.48	+24 52 46.4	0.52	5.0	5.7	4.4	5.5
WPL 295	03 47 00.29	+24 28 24.9	0.44	4.5	7.3	3.3	4.5
WPL 296	03 47 00.35	+23 52 48.4	0.39	5.5	5.6	3.6	6.0
WPL 297	03 47 01.84	+24 13 28.4	0.02	5.5	13.4	3.5	6.7
WPL 298	03 47 02.34	+23 32 36.4	0.40	5.0	4.1	3.1	6.7
WPL 299	03 47 05.78	+23 45 35.1	0.38	6.5	7.8	4.6	8.4
WPL 300	03 47 07.87	+24 23 38.0	0.47	4.0	2.6	3.2	3.9
WPL 301	03 47 08.14	+24 18 24.8	0.51	3.5	6.9	3.0	3.2
WPL 302	03 47 09.17	+24 03 07.8	0.47	3.0	5.8	3.1	2.9
WPL 303	03 47 09.41	+24 15 35.0	0.32	5.0	7.0	3.3	5.1
WPL 304	03 47 09.51	+23 25 56.5	0.20	4.0	5.1	3.4	4.2
WPL 305	03 47 10.20	+24 43 35.7	0.03	4.0	< 1	2.2	2.8
WPL 306	03 47 10.64	+23 58 16.5	0.45	5.5	9.1	3.2	5.7
WPL 307	03 47 11.86	+24 13 54.0	0.52	5.0	6.7	3.4	7.6
WPL 308	03 47 13.16	+24 00 45.4	0.29	5.0	9.0	3.5	4.6

Table 5.5 (continued)

ID (this work)	RA (J2000)	DEC	p	M type	$W_{\mathrm{H}\alpha}$	W_{NaI}	W_{KI}
WPL 309	03 47 15.37	+23 26 06.1	0.50	4.0	6.3	3.7	3.6
WPL 310	03 47 15.44	+24 23 31.2	0.51	2.0	7.3	3.5	5.5
WPL 311	03 47 16.45	+24 44 50.5	0.11	5.0	6.7	3.6	5.3
WPL 312	03 47 18.13	+24 13 51.4	0.52	4.5	6.7	3.7	4.9
WPL 313	03 47 22.02	+23 21 36.6	0.20	4.5	9.7	3.5	4.4
WPL 314	03 47 22.67	+23 44 07.1	0.51	4.5	10.0	3.6	4.5
WPL 315	03 47 22.73	+23 01 58.2	0.04	4.5	< 1	3.7	3.6
WPL 316	03 47 22.97	+24 50 56.3	0.41	4.0	5.9	3.1	3.3
WPL 317	03 47 23.85	+23 08 57.1	0.01	4.0	6.4	3.0	3.3
WPL 318	03 47 25.12	+24 15 17.4	0.08	5.0	4.6	3.1	3.8
WPL 319	03 47 25.34	+24 02 57.0	< 0.01	2.5	3.2	2.2	2.4
WPL 320	03 47 27.27	+24 49 16.5	0.34	2.0	< 1	2.5	2.2
WPL 321	03 47 27.62	+22 49 53.3	0.04	3.5	5.0	2.9	2.9
WPL 322	03 47 28.11	+23 26 53.5	0.43	3.0	5.6	2.7	3.1
WPL 323	03 47 28.43	+24 40 33.4	0.40	4.0	5.8	3.0	3.5
WPL 324	03 47 29.57	+23 52 49.6	0.16	4.5	6.9	3.5	3.7
WPL 325	03 47 29.92	+23 33 15.1	0.39	4.5	10.0	3.4	6.7
WPL 326	03 47 31.62	+23 52 19.3	0.06	4.5	7.9	3.7	4.7
WPL 327	03 47 31.99	+24 10 25.0	0.50	4.0	12.3	3.5	4.2
WPL 328	03 47 34.78	+22 48 04.9	0.52	3.5	5.9	3.0	3.5
WPL 329	03 47 35.85	+24 52 26.9	0.17	4.5	9.8	3.5	4.7
WPL 330	03 47 36.04	+23 28 27.0	0.50	4.0	10.2	3.2	4.2
WPL 331	03 47 37.65	+24 24 23.4	< 0.01	4.5	7.2	3.3	5.1
WPL 332	03 47 38.04	+24 49 11.1	0.26	2.5	3.8	2.5	2.4
WPL 333	03 47 39.26	+23 56 45.2	< 0.01	3.0	< 1	1.8	2.8
WPL 334	03 47 39.35	+24 27 32.3	0.17	4.0	5.4	3.1	3.9
WPL 335	03 47 39.78	+23 00 04.9	0.08	4.0	4.5	2.9	4.4
WPL 336	03 47 40.96	+21 49 05.4	0.32	5.0	4.9	3.6	6.1
WPL 337	03 47 44.65	+23 42 03.4	0.52	4.5	7.4	3.7	5.1
WPL 338	03 47 45.73	+24 05 37.4	0.41	4.0	7.8	3.3	3.9
WPL 339	03 47 45.90	+24 38 01.5	0.36	4.5	8.5	3.7	4.5
WPL 340	03 47 46.37	+24 03 02.6	0.51	2.0	2.6	2.0	2.3
WPL 341	03 47 49.77	+24 25 43.4	0.52	4.5	7.9	3.3	4.0
WPL 342	03 47 50.00	+23 27 53.1	0.02	3.0	< 1	2.9	2.5
WPL 343	03 47 51.95	+23 39 48.2	0.49	4.5	7.8	3.3	4.3
WPL 344	03 47 52.86	+22 59 34.2	0.36	4.0	7.5	3.3	4.3
WPL 345	03 47 55.26	+23 19 06.1	0.45	3.5	5.1	2.8	2.9
WPL 346	03 47 56.62	+24 15 32.1	0.47	5.0	7.5	3.9	4.8
WPL 347	03 47 59.36	+24 35 37.3	0.06	3.5	7.0	3.7	4.4
WPL 348	03 48 00.80	+21 44 46.2	< 0.01	4.0	< 1	2.8	2.8
WPL 349	03 48 04.98	+23 24 13.9	0.48	4.5	4.4	3.7	5.8
WPL 350	03 48 05.84	+23 53 01.3	0.17	5.0	6.7	3.4	5.4
WPL 351	03 48 06.62	+24 00 07.1	0.09	4.0	8.5	3.7	4.5
WPL 352	03 48 07.96	+23 44 23.9	0.51	3.5	6.9	3.2	3.8

Table 5.5 (continued)

ID (this work)	RA (J2000)	DEC	p	M type	$W_{\mathrm{H}\alpha}$	W_{NaI}	W_{KI}
WPL 353	03 48 08.81	+25 01 45.7	0.20	3.0	< 1	2.7	2.3
WPL 354	03 48 08.94	+23 42 23.7	0.47	4.5	8.6	3.5	4.1
WPL 355	03 48 09.19	+23 58 41.1	0.31	4.0	5.0	3.1	3.4
WPL 356	03 48 10.15	+23 59 20.6	0.16	$\geq$6.5	10.5	4.1	5.9
WPL 357	03 48 13.29	+23 58 47.3	0.35	4.0	9.1	3.9	4.6
WPL 358	03 48 15.23	+23 26 05.7	0.47	3.5	5.0	2.9	3.6
WPL 359	03 48 15.25	+23 42 03.7	0.20	4.0	6.2	3.4	3.9
WPL 360	03 48 15.73	+24 19 42.6	< 0.01	3.5	< 1	2.6	2.0
WPL 361	03 48 16.07	+23 35 15.7	0.43	4.5	5.8	3.3	4.6
WPL 362	03 48 17.35	+23 48 23.9	0.34	4.5	9.9	3.1	4.5
WPL 363	03 48 17.61	+22 04 01.3	0.05	4.0	5.9	3.3	3.8
WPL 364	03 48 20.57	+23 31 01.7	0.16	5.0	11.2	3.6	7.3
WPL 365	03 48 21.52	+24 34 43.7	0.32	4.5	6.7	3.3	4.4
WPL 366	03 48 22.69	+23 27 43.1	0.31	4.5	9.9	3.8	4.4
WPL 367	03 48 22.80	+24 48 53.7	0.42	3.5	5.7	2.7	3.0
WPL 368	03 48 23.91	+23 08 08.5	0.16	4.0	5.1	2.9	4.0
WPL 369	03 48 25.23	+24 14 26.3	0.47	4.5	7.8	3.3	4.1
WPL 370	03 48 26.01	+21 49 40.1	0.07	4.0	3.7	3.5	4.9
WPL 371	03 48 26.58	+23 11 30.0	0.46	5.5	8.6	3.4	3.3
WPL 372	03 48 29.73	+23 58 06.1	0.48	4.5	11.0	3.7	5.7
WPL 373	03 48 33.78	+24 01 59.2	0.42	4.0	3.9	2.8	3.5
WPL 374	03 48 34.04	+24 13 59.7	0.32	3.0	< 1	3.3	2.3
WPL 375	03 48 35.48	+24 12 03.4	0.22	4.5	13.1	3.6	4.7
WPL 376	03 48 39.30	+24 50 20.1	0.51	5.0	5.8	4.1	5.0
WPL 377	03 48 40.42	+24 36 34.2	0.52	4.5	7.2	3.4	4.1
WPL 378	03 48 40.98	+23 14 17.6	0.45	4.5	5.7	3.4	4.6
WPL 379	03 48 42.13	+25 00 28.4	0.43	3.0	5.4	2.9	2.9
WPL 380	03 48 42.68	+24 27 19.6	0.31	5.0	4.7	3.7	5.4
WPL 381	03 48 44.03	+25 06 22.6	0.48	4.0	5.0	3.1	3.5
WPL 382	03 48 45.35	+24 37 26.5	0.41	4.5	6.7	3.5	4.5
WPL 383	03 48 46.01	+24 10 12.9	0.42	4.0	6.1	3.0	3.6
WPL 384	03 48 48.23	+21 24 40.9	0.44	4.5	10.7	3.2	3.9
WPL 385	03 48 48.78	+23 24 48.3	0.46	4.5	9.3	4.0	5.1
WPL 386	03 48 50.50	+24 08 27.5	0.40	3.0	8.1	3.2	6.5
WPL 387	03 48 50.66	+23 04 30.3	0.49	4.0	5.0	3.2	4.3
WPL 388	03 48 58.28	+23 05 39.3	0.50	2.5	2.0	2.4	2.5
WPL 389	03 48 59.76	+23 12 07.5	0.41	5.0	6.9	3.3	7.1
WPL 390	03 49 00.98	+24 54 10.2	0.49	3.5	6.6	2.9	3.2
WPL 391	03 49 01.14	+23 38 15.8	0.52	5.5	6.3	3.9	6.4
WPL 392	03 49 01.49	+24 11 38.6	0.48	4.0	7.1	3.6	4.3
WPL 393	03 49 02.97	+21 54 47.2	0.39	5.0	7.4	3.4	4.6
WPL 394	03 49 05.91	+23 06 22.2	0.35	3.5	8.0	3.2	3.7
WPL 395	03 49 11.02	+24 20 51.4	0.51	3.5	20.2	3.0	2.9
WPL 396	03 49 11.41	+24 14 24.8	0.46	4.5	6.2	3.2	3.9

Table 5.5 (continued)

ID (this work)	RA (J2000)	DEC	p	M type	$W_{\mathrm{H}\alpha}$	W_{NaI}	W_{KI}
WPL 397	03 49 13.22	+21 22 01.2	0.36	5.0	7.5	3.3	4.8
WPL 398	03 49 15.61	+23 22 49.6	0.03	4.0	5.0	3.0	4.2
WPL 399	03 49 20.28	+25 25 42.7	0.52	3.5	5.5	3.0	3.2
WPL 400	03 49 20.66	+24 52 35.5	0.25	4.5	2.9	2.4	3.1
WPL 401	03 49 21.24	+24 41 41.2	0.50	4.5	7.6	3.5	5.2
WPL 402	03 49 21.48	+23 39 06.7	0.46	4.0	6.9	3.3	3.9
WPL 403	03 49 21.91	+24 54 43.5	0.02	4.0	16.2	3.0	3.1
WPL 404	03 49 22.50	+21 37 56.3	0.33	4.5	5.8	3.3	4.5
WPL 405	03 49 25.59	+23 02 50.4	0.13	4.5	8.9	3.3	4.5
WPL 406	03 49 27.57	+24 24 13.9	0.36	4.5	6.1	3.5	4.7
WPL 407	03 49 29.79	+23 38 55.6	0.49	4.5	4.5	3.5	5.3
WPL 408	03 49 31.20	+23 41 20.0	0.47	4.5	7.8	3.8	5.3
WPL 409	03 49 32.15	+23 16 18.3	0.32	4.5	5.8	3.5	4.3
WPL 410	03 49 32.52	+23 55 42.7	0.40	3.5	5.8	3.1	3.7
WPL 411	03 49 33.11	+24 13 05.0	0.44	5.5	6.2	3.6	5.3
WPL 412	03 49 36.10	+23 56 23.4	0.40	4.0	7.4	3.1	3.7
WPL 413	03 49 36.52	+24 18 14.3	0.52	4.0	5.4	3.0	3.6
WPL 414	03 49 41.14	+23 14 59.7	0.22	3.5	5.4	3.5	6.3
WPL 415	03 49 41.70	+21 56 19.6	0.48	5.0	7.6	3.6	5.7
WPL 416	03 49 48.43	+22 10 48.7	0.35	3.5	4.8	2.8	2.6
WPL 417	03 49 52.42	+24 03 43.3	0.24	?	5.3	3.7	6.4
WPL 418	03 49 55.48	+24 06 05.3	0.03	4.5	9.8	3.5	4.0
WPL 419	03 49 56.75	+25 22 23.0	0.47	3.5	< 1	2.8	2.8
WPL 420	03 49 56.79	+21 57 42.9	0.05	3.0	4.6	2.8	2.6
WPL 421	03 49 57.63	+23 43 28.3	0.52	$\geq$6.5	9.8	3.8	8.1
WPL 422	03 49 59.54	+24 11 46.1	0.47	4.5	8.5	3.9	5.6
WPL 423	03 50 01.85	+25 12 41.1	0.36	4.0	6.5	3.3	3.7
WPL 424	03 50 02.17	+23 51 44.7	0.49	3.5	6.6	2.7	3.7
WPL 425	03 50 04.24	+23 10 44.8	0.34	1.5	< 1	2.1	2.0
WPL 426	03 50 05.00	+23 18 17.6	0.51	2.5	4.2	2.8	3.8
WPL 427	03 50 06.55	+24 59 46.8	0.51	4.0	5.6	3.5	4.5
WPL 428	03 50 08.41	+25 32 56.2	0.27	4.0	7.6	3.1	3.3
WPL 429	03 50 08.62	+24 40 18.0	0.22	4.5	4.1	3.2	4.4
WPL 430	03 50 09.05	+23 07 51.6	0.06	3.5	< 1	3.4	2.0
WPL 431	03 50 10.76	+24 28 41.6	0.50	4.5	7.2	3.7	5.1
WPL 432	03 50 12.44	+23 55 36.2	0.47	4.5	7.9	3.6	5.2
WPL 433	03 50 14.74	+25 25 30.4	0.43	4.5	10.3	3.5	4.1
WPL 434	03 50 15.26	+24 13 36.2	0.45	4.0	7.2	3.2	4.0
WPL 435	03 50 17.58	+22 55 59.2	0.34	4.5	5.5	3.5	4.8
WPL 436	03 50 27.32	+21 24 35.8	0.02	4.5	5.7	3.4	4.0
WPL 437	03 50 27.34	+23 22 45.3	0.46	4.5	9.4	2.9	3.6
WPL 438	03 50 27.82	+23 03 55.3	0.46	4.0	7.1	2.8	3.4
WPL 439	03 50 29.29	+24 56 35.0	0.15	3.5	0.9	3.2	2.7
WPL 440	03 50 31.94	+22 08 47.8	0.35	3.5	5.0	3.0	3.7

Table 5.5 (continued)

ID (this work)	RA (J2000)	DEC	p	M type	$W_{\mathrm{H}\alpha}$	W_{NaI}	W_{KI}
WPL 441	03 50 33.07	+24 20 22.0	< 0.01	4.0	5.4	3.2	3.6
WPL 442	03 50 40.82	+24 40 02.9	0.52	4.5	4.8	3.3	4.5
WPL 443	03 50 42.14	+23 29 33.5	0.47	4.5	5.9	3.5	4.8
WPL 444	03 50 42.42	+24 12 55.6	0.50	4.0	3.9	5.0	4.4
WPL 445	03 50 43.06	+23 19 56.1	0.30	5.5	4.9	3.2	5.9
WPL 446	03 50 44.33	+25 07 05.3	0.10	5.5	6.8	3.9	5.8
WPL 447	03 50 50.94	+23 58 44.2	0.33	4.5	10.9	3.7	4.4
WPL 448	03 50 54.63	+24 21 56.0	0.44	4.0	7.6	3.3	3.7
WPL 449	03 50 54.97	+24 33 03.8	0.12	4.0	7.1	3.3	3.8
WPL 450	03 50 58.15	+23 55 42.7	0.48	4.0	6.3	3.3	4.2
WPL 451	03 51 03.27	+23 35 00.5	0.46	4.0	4.7	1.5	4.2
WPL 452	03 51 03.60	+24 32 35.5	0.51	4.0	8.8	3.3	4.6
WPL 453	03 51 07.10	+23 20 57.9	0.45	4.0	6.4	3.1	3.7
WPL 454	03 51 11.89	+23 44 43.5	0.16	4.5	4.1	3.2	3.9
WPL 455	03 51 13.49	+25 24 38.2	0.26	5.0	6.8	3.5	4.9
WPL 456	03 51 13.85	+25 23 11.4	0.20	3.5	7.3	2.9	3.0
WPL 457	03 51 19.48	+23 09 49.8	0.45	3.5	7.2	3.0	3.1
WPL 458	03 51 19.76	+23 04 04.4	0.11	5.0	7.3	3.8	5.0
WPL 459	03 51 24.94	+25 00 10.8	0.03	2.5	< 1	2.4	2.1
WPL 460	03 51 34.02	+24 34 09.1	0.52	4.0	5.1	3.7	4.1
WPL 461	03 51 34.25	+23 47 50.1	0.48	4.5	5.4	3.1	3.9
WPL 462	03 51 36.41	+25 13 40.9	0.32	4.5	6.9	3.4	4.2
WPL 463	03 51 39.10	+24 35 29.7	0.39	4.0	6.7	3.4	4.3
WPL 464	03 51 39.18	+23 51 18.5	0.38	5.0	5.1	3.5	5.0
WPL 465	03 51 42.30	+24 21 41.7	0.40	4.0	5.1	2.8	3.5
WPL 466	03 51 50.57	+22 53 44.6	0.50	3.5	5.4	3.0	3.4
WPL 467	03 51 51.53	+23 34 49.4	0.30	4.5	4.8	3.5	4.0
WPL 468	03 51 54.50	+23 33 31.7	0.52	4.5	7.4	3.3	3.9
WPL 469	03 51 55.03	+23 57 42.3	0.52	4.5	6.5	3.3	4.4
WPL 470	03 51 58.33	+23 58 19.6	0.48	4.5	6.4	3.5	3.9
WPL 471	03 51 59.31	+24 39 59.4	0.41	4.0	6.0	3.1	3.2
WPL 472	03 52 02.63	+25 06 15.3	0.49	4.0	7.2	3.2	4.3
WPL 473	03 52 03.57	+25 01 14.2	0.50	4.0	7.5	3.2	3.9
WPL 474	03 52 07.95	+25 27 54.8	0.52	4.5	5.9	3.5	4.0
WPL 475	03 52 17.44	+25 06 12.2	< 0.01	3.5	< 1	2.7	2.7
WPL 476	03 52 17.55	+24 27 19.9	0.40	4.5	7.7	3.1	3.9
WPL 477	03 52 31.37	+25 15 08.0	0.52	4.0	5.1	2.7	2.9
WPL 478	03 52 33.33	+23 51 07.0	0.43	4.0	5.5	3.4	2.8
WPL 479	03 52 35.30	+25 01 05.1	0.09	4.5	6.4	4.2	5.2
WPL 480	03 52 42.18	+25 10 42.6	0.49	5.0	4.9	2.7	4.8
WPL 481	03 52 43.22	+24 27 58.9	0.52	4.5	4.7	3.2	3.8
WPL 482	03 52 44.27	+23 54 15.2	0.52	5.0	6.6	3.8	5.2
WPL 483	03 52 44.47	+24 20 59.7	0.38	4.5	5.3	3.1	4.1
WPL 484	03 53 01.62	+22 58 48.6	< 0.01	4.0	6.2	3.3	4.0

Table 5.5 (continued)

ID (this work)	RA (J2000)	DEC	p	M type	$W_{\mathrm{H}\alpha}$	W_{NaI}	W_{KI}
WPL 485	03 53 13.98	+19 42 59.9	0.51	4.5	1.4	2.9	2.5
WPL 486	03 53 30.74	+19 54 24.5	0.43	3.0	4.0	2.7	2.7
WPL 487	03 54 06.95	+19 19 14.7	0.48	4.0	0.5	1.7	9.0
WPL 488	03 54 21.83	+26 50 24.8	0.41	3.0	< 1	2.1	1.8
WPL 489	03 54 38.00	+19 54 22.9	0.51	4.5	8.9	3.5	4.7
WPL 490	03 54 41.31	+19 57 15.2	0.39	3.0	< 1	2.6	2.8
WPL 491	03 54 42.19	+26 26 31.2	< 0.01	4.5	< 1	3.7	3.3
WPL 492	03 54 49.91	+19 50 45.5	0.01	4.0	< 1	2.7	2.6
WPL 493	03 55 00.28	+27 00 38.3	0.52	$\geq$6.5	7.2	4.9	2.9
WPL 494	03 55 13.63	+19 30 17.1	0.45	3.5	5.0	2.7	3.0
WPL 495	03 55 59.92	+27 00 00.0	0.51	4.5	5.9	3.1	3.8
WPL 496	03 56 00.43	+26 26 29.1	0.37	5.5	< 1	< 1	< 1
WPL 497	03 56 38.74	+21 35 08.6	0.28	5.5	9.3	2.9	5.2
WPL 498	03 56 46.58	+26 21 00.7	0.45	5.0	1.0	2.9	< 1
WPL 499	03 57 09.80	+21 36 27.6	0.50	4.5	6.6	3.6	3.8
WPL 500	03 57 18.17	+21 37 47.8	0.08	0.0	< 1	1.5	2.2
WPL 501	03 57 41.59	+21 18 16.1	0.06	$\geq$6.5	17.3	3.8	4.1
WPL 502	03 57 46.70	+22 08 23.4	0.40	$\geq$6.5	< 1	4.8	6.4
WPL 503	03 57 49.34	+22 08 31.4	0.44	6.0	10.3	3.8	6.8
WPL 504	03 58 01.94	+23 53 54.8	0.47	4.5	6.1	2.9	4.7
WPL 505	03 58 21.75	+26 48 41.4	0.02	3.0	1.3	< 1	< 1
WPL 506	03 58 25.14	+24 00 59.0	0.51	3.5	7.0	3.1	4.6
WPL 507	03 58 31.87	+26 47 05.3	0.32	0.0	< 1	< 1	< 1
WPL 508	03 58 41.22	+21 32 03.0	0.39	4.5	< 1	2.8	3.9
WPL 509	03 58 50.04	+21 36 53.5	0.43	5.5	5.2	3.4	8.1
WPL 510	03 59 18.96	+23 31 24.4	0.50	4.5	7.9	3.1	4.5
WPL 511	03 59 23.53	+23 57 10.3	0.03	4.5	< 1	3.5	3.2
WPL 512	03 59 26.89	+21 48 19.0	0.52	4.5	16.4	3.2	4.7
WPL 513	03 59 27.73	+21 52 44.0	< 0.01	3.5	< 1	3.4	2.6
WPL 514	03 59 29.29	+21 39 56.4	0.37	4.5	8.0	3.8	4.8
WPL 515	03 59 39.81	+21 54 28.1	0.52	3.0	3.5	2.6	2.4
WPL 516	03 59 42.11	+23 38 33.8	< 0.01	6.0	< 1	4.0	< 1
WPL 517	03 59 46.90	+23 49 15.1	0.09	4.5	8.9	3.1	3.4
WPL 518	03 59 56.48	+23 40 15.5	0.49	5.0	8.2	4.5	7.1
WPL 519	03 59 59.15	+23 41 04.8	0.18	2.5	1.7	2.3	5.3
WPL 520	04 00 09.00	+24 03 26.0	0.52	4.0	3.9	3.3	4.5
WPL 521	04 00 16.92	+23 26 23.0	0.02	3.0	0.9	1.8	2.4
WPL 522	04 00 26.14	+23 26 17.9	0.46	4.5	6.2	3.1	4.1
WPL 523	04 00 28.17	+23 51 24.8	0.32	3.5	6.5	2.7	4.3
WPL 524	04 00 40.24	+23 26 54.4	0.49	4.5	6.8	4.0	5.2
WPL 525	04 01 05.79	+23 34 44.3	0.36	3.5	< 1	3.1	0.7
WPL 526	04 01 07.73	+24 08 23.1	0.02	2.5	< 1	2.2	2.9
WPL 527	04 01 12.05	+23 54 13.3	0.51	4.0	4.8	2.2	3.2
WPL 528	04 01 12.62	+23 50 20.8	0.37	3.5	6.5	3.2	6.7

Table 5.6: Cross identifications for Pleiades candidates in the spectroscopic study. Abbreviations are given in §4.1.1.

ID	Cross-ID
WPL 026	HHJ 248
WPL 029	HHJ 32
WPL 034	HHJ 2
WPL 035	HHJ 98
WPL 036	HHJ 97
WPL 037	HCG 11, HHJ 378
WPL 038	HHJ 91
WPL 042	HHJ 349
WPL 045	HHJ 359
WPL 048	HCG 22,HHJ 230
WPL 050	HHJ 324
WPL 051	HHJ 291
WPL 052	HHJ 74
WPL 056	HHJ 102
WPL 058	HHJ 38
WPL 060	HHJ 147
WPL 061	HHJ 29
WPL 063	HCG 33, SK 772, HHJ 343
WPL 064	HHJ 135
WPL 065	SK 778, HHJ 338
WPL 066	HHJ 169
WPL 067	HCG 36, SK 766, HHJ 329
WPL 068	HHJ 101
WPL 070	SK 750
WPL 072	HHJ 41
WPL 075	SK 733
WPL 077	HCG 48
WPL 078	HHJ 191
WPL 080	HCG 49, SK 730, HHJ 233
WPL 081	HHJ 117
WPL 084	SK 729, HHJ 340
WPL 085	HHJ 90
WPL 087	HCG 50, SK 725, HHJ 285
WPL 088	HHJ 12
WPL 089	HHJ 148
WPL 094	HHJ 58
WPL 095	HHJ 108
WPL 097	HCG 55, SK 705, HHJ 342
WPL 098	HCG 66, HHJ 312
WPL 100	HHJ 212
WPL 102	HHJ 270
WPL 104	HHJ 34
WPL 105	HHJ 109
WPL 106	HHJ 129

Table 5.6 (continued)

ID	Cross-ID
WPL 108	HHJ 49
WPL 109	HCG 73, SK 680, HHJ 262
WPL 110	SK 677
WPL 116	HCG 82, HHJ 115
WPL 118	HHJ 45
WPL 119	SK 665, HHJ 341
WPL 121	HHJ 119
WPL 123	HHJ 52
WPL 125	HHJ 153
WPL 126	SK 663
WPL 127	HCG 90, SK 661
WPL 129	HCG 92
WPL 132	HHJ 107
WPL 134	HCG 96
WPL 135	HHJ 71
WPL 136	SK 650
WPL 137	HCG 102, SK 653, HHJ 328
WPL 139	SK 651, HHJ 206
WPL 142	HCG 110, HHJ 143
WPL 143	HCG 106, HHJ 88
WPL 144	HHJ 65
WPL 146	HHJ 134
WPL 147	HCG 114, SK 644, HHJ 261
WPL 148	SK 638, HHJ 368
WPL 150	HCG 109, SK 635
WPL 151	HHJ 76
WPL 152	HHJ 50
WPL 155	SK 622, HHJ 337
WPL 156	HCG 122, HHJ 205
WPL 157	SK 619
WPL 158	SK 630
WPL 159	HCG 124, SK 624
WPL 160	HHJ 40
WPL 161	HHJ 77
WPL 163	HHJ 43
WPL 165	SK 618, HHJ 321
WPL 166	HCG 125, HHJ 298
WPL 167	HCG 128
WPL 168	HHJ 218
WPL 169	HCG 129, SK 598, HHJ 382
WPL 170	HCG 135, HHJ 229
WPL 171	HCG 133, SK 601
WPL 174	HHJ 186
WPL 175	SK 586

Table 5.6 (continued)

ID	Cross-ID
WPL 176	HHJ 235
WPL 178	HHJ 59
WPL 179	HHJ 217
WPL 180	HCG 138, SK 579
WPL 181	HCG 144, SK 580, HHJ 301
WPL 183	HCG 146, HHJ 228
WPL 184	HHJ 57
WPL 185	HCG 155, SK 575, HHJ 300
WPL 186	HCG 143, SK 568, HHJ 348
WPL 187	HCG 148, SK 569, HHJ 307
WPL 188	HHJ 100
WPL 189	HHJ 243
WPL 190	HHJ 190
WPL 192	SK 564, HHJ 265
WPL 193	HHJ 68
WPL 195	HCG 157
WPL 196	HHJ 5
WPL 197	HHJ 46
WPL 198	HHJ 189
WPL 199	HCG 160
WPL 200	HHJ 24
WPL 202	HCG 167, HHJ 276
WPL 203	HCG 166, HHJ 239
WPL 207	HHJ 183
WPL 208	HCG 171, HHJ 304
WPL 209	HHJ 269
WPL 212	HHJ 223
WPL 213	HHJ 274
WPL 214	HHJ 54
WPL 215	HCG 172, SK 538, HHJ 216
WPL 217	HHJ 139
WPL 218	HHJ 113
WPL 219	HHJ 48
WPL 220	HCG 176, HHJ 136
WPL 223	HHJ 81
WPL 224	HHJ 164
WPL 225	HCG 186, SK 535
WPL 226	HCG 177
WPL 227	HCG 185, SK 532, HHJ 255
WPL 228	HCG 180, HHJ 118
WPL 229	HCG 184, SK 531
WPL 231	HCG 181, HHJ 405
WPL 233	HHJ 273
WPL 237	HHJ 99

Table 5.6 (continued)

ID	Cross-ID
WPL 238	HHJ 106
WPL 239	SK 520
WPL 242	HCG 194, HHJ 380
WPL 244	HHJ 130
WPL 249	HHJ 25
WPL 250	HHJ 166
WPL 251	HCG 202, SK 504, HHJ 227
WPL 254	HCG 205, HHJ 199
WPL 255	HHJ 27
WPL 257	HHJ 127
WPL 259	HCG 206
WPL 260	HHJ 363
WPL 262	HHJ 194
WPL 264	HCG 209
WPL 266	HHJ 367
WPL 268	HHJ 105
WPL 269	HHJ 33
WPL 274	HHJ 249
WPL 275	HHJ 326
WPL 276	HHJ 87
WPL 277	HHJ 30
WPL 278	HHJ 140
WPL 279	SK 465, HHJ 282
WPL 280	HCG 234
WPL 282	HHJ 75
WPL 283	HHJ 159
WPL 284	HCG 240, HHJ 253
WPL 286	HHJ 247
WPL 289	HHJ 95
WPL 290	HHJ 257
WPL 291	HHJ 174
WPL 292	HCG 246, HHJ 296
WPL 293	HHJ 299
WPL 294	HHJ 222
WPL 295	HHJ 252
WPL 301	HCG 253, SK440
WPL 303	HHJ 37
WPL 307	HHJ 92
WPL 309	HHJ 203
WPL 314	HCG 266
WPL 315	HHJ 23
WPL 316	HCG 261, SK 425, HHJ 335
WPL 317	HCG 270, SK 427, HHJ 275
WPL 318	HHJ 198

Table 5.6 (continued)

ID	Cross-ID
WPL 319	HHJ 427
WPL 322	SK 417, HHJ 315
WPL 325	HHJ 16
WPL 328	HCG 284, HHJ 278
WPL 329	HCG 279, HHJ 157
WPL 330	HHJ 73
WPL 332	SK 409, HHJ 360
WPL 334	HCG 282, HHJ 272
WPL 335	HHJ 94
WPL 337	HHJ 152
WPL 339	HCG 287, HHJ 168
WPL 340	HHJ 438
WPL 341	HCG 292, HHJ 202
WPL 343	HHJ 122
WPL 344	SK 394, HHJ 258
WPL 345	HCG 302, SK 392, HHJ 289
WPL 349	HHJ 21
WPL 351	HHJ 240
WPL 352	HCG 307, HHJ 288
WPL 354	HHJ 156
WPL 355	HHJ 225
WPL 357	HCG 311
WPL 358	HHJ 232
WPL 359	HHJ 336
WPL 361	HHJ 151
WPL 362	HHJ 188
WPL 363	HHJ 187
WPL 366	HHJ 171
WPL 367	SK 368, HHJ 309
WPL 369	HCG 322, SK 363, HHJ 314
WPL 371	HCG 332, SK 362, HHJ 339
WPL 372	HCG 328, HHJ 132
WPL 373	HHJ 184
WPL 375	HHJ 96
WPL 377	HCG 333, SK 351
WPL 378	HCG 343, SK 352
WPL 379	HCG 339, SK 349
WPL 380	HHJ 44
WPL 382	HCG 346, HHJ 111
WPL 383	HHJ 207
WPL 385	HHJ 86
WPL 387	HHJ 116
WPL 388	HHJ 353
WPL 390	HCG 351, SK 335, HHJ 332

Table 5.6 (continued)

ID	Cross-ID
WPL 392	HHJ 231
WPL 394	HCG 357, SK 332
WPL 395	HCG 355, HHJ 287
WPL 398	HHJ 36
WPL 399	HCG 366, HHJ 251
WPL 401	HHJ 51
WPL 402	HCG 363,SK 319, HHJ 306
WPL 403	SK 316
WPL 405	HHJ 79
WPL 406	HHJ 192
WPL 407	HHJ 158
WPL 408	HHJ 142
WPL 410	HCG 371, SK 310, HHJ 221
WPL 412	HCG 373, SK 307, HHJ 286
WPL 413	HCG 375, HHJ 250
WPL 423	HCG 385, SK 289
WPL 424	HCG 382
WPL 425	SK 287
WPL 428	HCG 386
WPL 432	SK 279
WPL 434	HCG 394, SK 276
WPL 437	SK 273
WPL 440	HCG 401
WPL 450	HCG 414
WPL 456	HCG 425
WPL 462	SK 220
WPL 463	HCG 432
WPL 466	HCG 437, SK 212
WPL 468	HCG 439, SK 210
WPL 469	HCG 440
WPL 471	HCG 445, SK 205
WPL 474	HCG 449
WPL 477	SK 179
WPL 484	HHJ 181
WPL 498	HHJ 64
WPL 503	HHJ 7
WPL 504	HHJ 84
WPL 506	HHJ 220
WPL 510	HHJ 150

5.4 Summary

This chapter presented a spectroscopic study performed for the Pleiades candidates selected in Chapter 4. Spectra were obtain with the Hydra multi-object spectrograph mounted on the WIYN telescope at Kitt Peak. A total of 528 spectra of Pleiades candidates were taken as well as 121 spectra of field stars as a control sample. The spectral results show that the photometric and proper motion selection described in Chapter 4 was extremely effective at detecting Pleiades members.

Since all Pleiades M dwarfs show strong Hα emission lines at 6563 Å, Hα equivalent widths were extracted from the spectra in order to identify obvious field star contamination in the Pleiades sample. The distribution of $W_{\mathrm{H}\alpha}$ indicates that a sample of high probability Pleiades candidates within 5° radius of the nominal center of the cluster contains roughly 13% contamination. The sample of objects fainter than $K_s = 14$ are likely to be substantially more contaminated even near the cluster center. Outside a 5° radius nearly all candidates are expected to be field stars with coincidental colors and proper motions.

Near-infrared colors of a large numbers Pleiades candidates with appropriate Hα emission allow a detailed investigation of the near-infrared properties of M dwarfs with similar age, distance, and metallicity. The colors of these high probability Pleiades candidates were compared to typical theoretical isochrones in the near-infrared. The isochrone colors were slightly bluer than Pleiades early M dwarfs in a $K : J - K_s$ color-magnitude diagram but more accurately fit mid-M dwarf colors. The isochrone was slightly bluer than early to mid-M dwarfs in a $J-H : H-K_s$ color-color diagram, perhaps due to a Pleiades metallicity above the solar value. The $J - H : H - K_s$ color-color diagram shows that high probability candidates are late type dwarfs rather than giants.

$W_{\mathrm{H}\alpha}$ measurement of a large number of stars shows no increase for fainter stars below $J = 13.2$. This observation reveals the beginning of trend towards low chro-

mospheric activity in brown dwarfs, suggesting that additional factors such as dust condensation may suppress the standard dynamo mechanism used to explain magnetic activity in low mass stars. Two confirmed flare stars were identified on the basis of excessive Hα widths and He I and Ca II emission during flaring.

Spectral types were determined using the relative depth of several absorption bands due primarily to TiO, CaH, and CaOH. Equivalent widths for the Na I and K I resonance doublets at 8183/8195 and 7665/7699 Å respectively were extracted for all object spectra. The trend of increasing $W_{\rm NaI}$ for high probability candidates also shows that the spectroscopic sample contains few if any background giants.

CHAPTER 6

THE MASS AND STRUCTURE OF THE PLEIADES

6.1 Introduction

The age distribution of open clusters suggests that they are transient objects which are dissolved by the Galactic tidal field in time scales typically less than ~ 1 Gyr (Wielen 1971). Due to the small number of constituent stars, open clusters have short relaxation times of order 10^8 years or less, comparable to their typical crossing time, and can thus be understood only as collisional systems which evolve more rapidly than larger systems such as globular clusters (King 1980). This rapid evolution produces observable effects, such as mass segregation and the development of a halo which in turn is subjected to Galactic tidal forces causing the dispersal of escaping stars. Despite the theoretical problems associated with collisional systems, the small number densities of stars in open clusters allows the use of direct N body simulation as a practical tool of study (Aarseth 1999; Terlevich 1987; Kroupa 1995). Unfortunately, both the input parameters and output results of N body simulations suffer from a lack of detailed observational guidance.

This thesis uses current sky survey data to study the dynamical structure of the Pleiades cluster as a means towards contributing to the dearth of observations of open cluster structure. This chapter uses the results of the Pleiades proper motion presented in Chapter 4 and its spectroscopic verification in Chapter 5 to map the distribution of mass in the Pleiades as a probe of its dynamical structure. This chapter discusses the radial distribution of low mass stars, the cluster mass function and total mass, and projected structure of the halo. The results of this work are compared

to previous work in the Pleiades and to predictions from published theoretical and numerical work.

6.2 Data and Stellar Masses

The Pleiades list was merged with probable members listed in the CfA Open Cluster Database containing relatively bright Pleiades members from Hertzsprung (1947), Stauffer et al. (1991), Haro, Chavira, & Gonzalez (1982), and HHJ. Other surveys are spatially incomplete and were thus excluded from this analysis.

Approximate masses are suitable for dividing all Pleiades candidates into dynamical mass groups. Figure 6.1 shows the adopted mass-magnitude relations for determining stellar masses. Masses were determined by interpolating the BCAH98 models (Baraffe et al. 1998) in the 0.9–0.07 $M_{\odot}$ range. The magnitudes used were 2MASS J magnitudes or HHJ I magnitudes for the 7 HHJ stars not listed in the POSS-2MASS database. Masses for candidates with 2MASS J magnitudes slightly brighter than $J = 9.8$ were determined by extrapolation. Masses for stars in the CfA Open Cluster Database with V magnitudes were determined using Mass-M_V relations from Henry & McCarthy (1993) up to $M_V \geq 1.45$ and Allen (1973) for $M_V < 1.45$. Absolute magnitudes were estimated for all Pleiades candidates by assuming a distance modulus of 5.5 (Lyngå 1987). Variations between photometric systems of the mass-luminosity relations and the data will not appreciably affect the stellar mass estimates.

For the following discussion I included only Pleiades candidates from this work with membership probability $p \geq 0.3$ in the merged list.

6.3 Mass Segregation

The long term internal evolution of an open cluster is described in terms of energy equipartition from kinetic theory of collisional systems. Briefly, lower mass stars

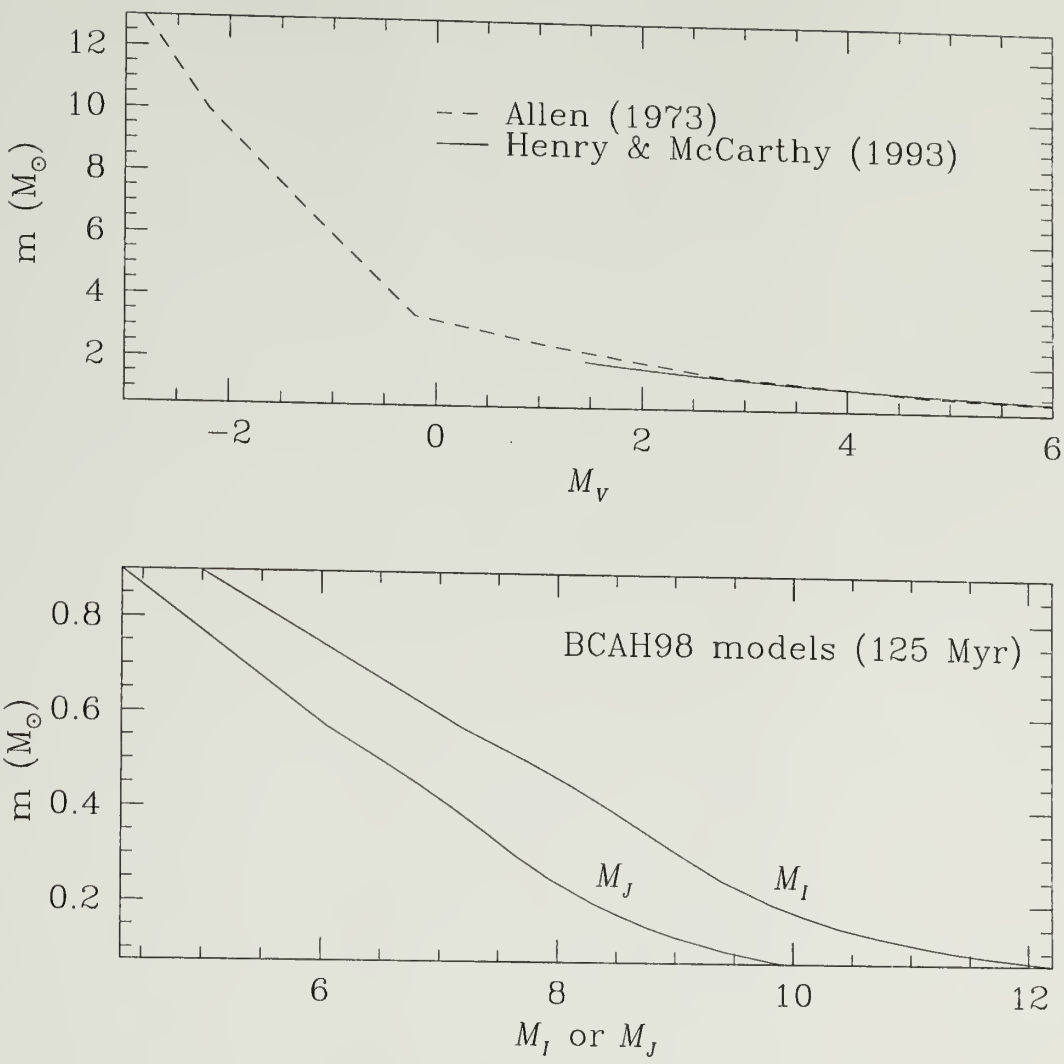

Fig. 6.1.— Mass-luminosity relations used to derive individual masses for the merged Pleiades sample. Top panel shows masses for bright stars from Henry & McCarthy (1993) (solid line) and Allen (1973) (broken line). Bottom panel shows relations from Baraffe et al. (1998) (BCAH98 models) transformed into the Johnson-Cousins I and CIT J system.

through encounters gradually acquire higher velocities resulting in larger, more radial orbits. High mass stars lose velocity and thus preferentially "sink" to the center of the cluster. This segregation of masses has been discussed by Spitzer & Shull (1975) and verified by the N body simulations of Terlevich (1987) and Kroupa (1995). This section discusses mass segregation in the Pleiades.

To estimate the extent of the cluster on the sky, I divided the sample into high, intermediate, and low mass groups and then binned the high mass stars into 0.25° annuli, and the low and intermediate mass stars into 0.5° annuli. I then calculated the surface number density out to a radius $r \approx 10°$ from the cluster center. Figure 6.2 shows the radial distribution for the three mass groups. Using a chi-square minimization, I fitted the low mass group to a standard single-mass King model (King 1962)

$$f_s = k \left[\frac{1}{\sqrt{1+(r/r_c)^2}} - \frac{1}{\sqrt{1+(r_t/r_c)^2}} \right]^2$$

where k is a constant, f_s is the suface density, r_c is the core or half-mass radius, and r_t is the so-called tidal radius where the cluster surface density drops to zero, or in our case where the cluster surface density becomes indistinguishable from the background. Before fitting, I subtracted the background surface number density, determined in the annulus at 7 – 10°, from each annulus. The best fit gave $r_c = 2.2 - 2.9$ pc and $r_t = 12.7 - 15.0$ pc (99% confidence). I superimposed this fit on the mean background surface density in Figure 6.2. These numbers only parameterize the empirical distribution of low mass stars on the sky, and this King tidal radius does not necessarily correspond to the location of the cluster's Lagrangian points along the Galactic X direction. Since the cluster's location is $l = 166°$ and $b = -23°$, the Lagrangian points in the X direction lie nearly along the line of sight, projected somewhere near the dense cluster center.

To reconstruct the spatial density $\phi(r)$, I used the King model (King 1962):

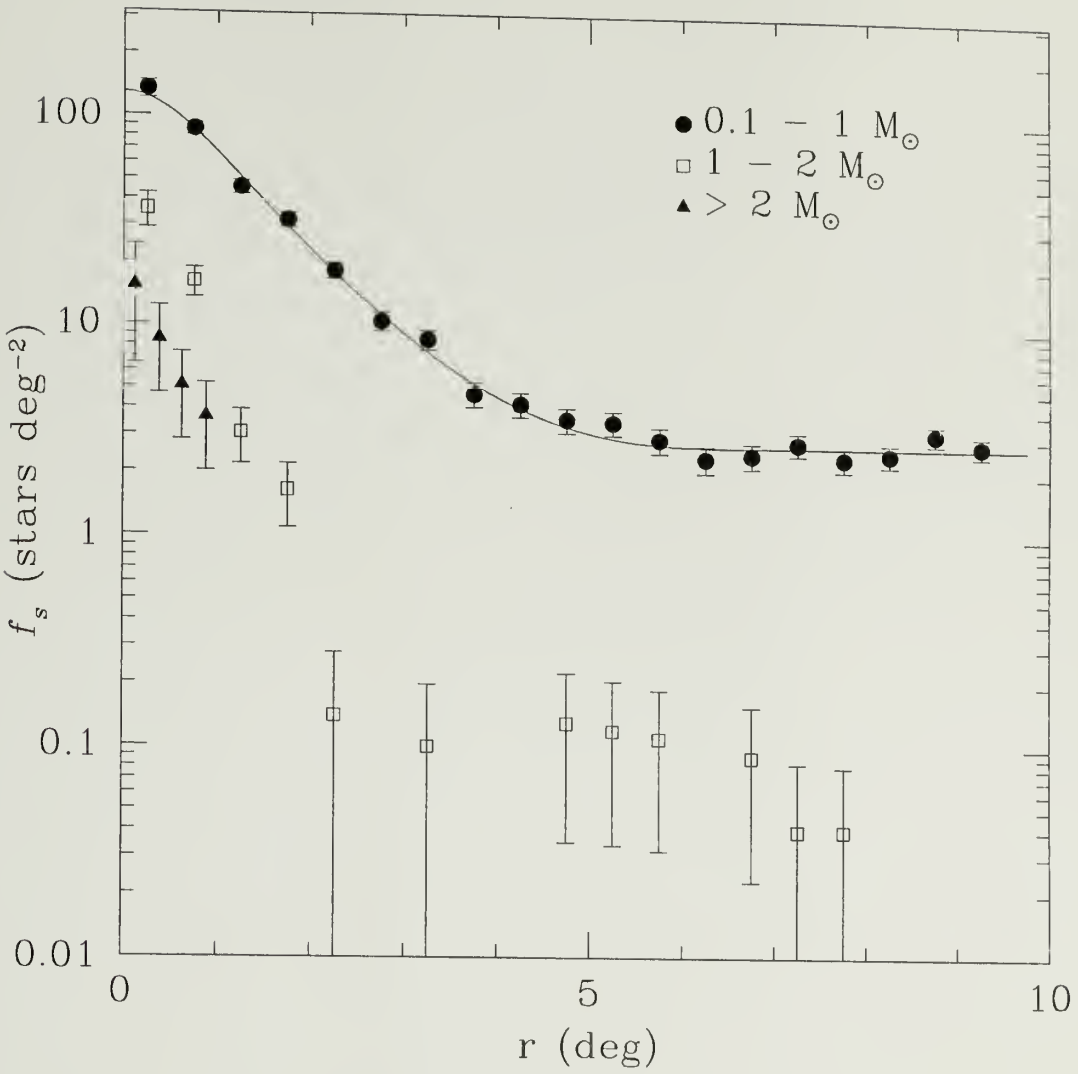

Fig. 6.2.— Surface number density f_s binned into annuli around the nominal center of the Pleiades for three mass groups. The solid line shows the best fit single-mass King profile for the mass group 0.1 – 1 $M_\odot$ superimposed on the mean background surface density. Error bars were derived from Poisson statistics in each bin.

$$\phi(r) = -\frac{1}{\pi}\int_r^{r_t}\left[\frac{d}{dx}f_s(x)\right]\frac{dx}{\sqrt{x^2-r^2}}$$

The surface density was differentiated numerically. Figure 6.3 shows the resulting spatial densities of mass groups with the low mass stars subdivided into finer mass groups. Stars with masses less than 1 $M_\odot$ have similar spatial densities. According to Figure 6.3, the highest mass stars dominate the core in terms of mass density, while stars below 1 $M_\odot$ dominate the halo beyond $\sim$ 5 pc. All stars below 1 $M_\odot$ show similar radial distribution, implying a similar velocity dispersion with respect to the mean cluster velocity.

These results qualitatively agree with Jones (1970) who, using high precision proper motions, concluded that a sample of low mass stars in the Pleiades did not show an increase in velocity dispersion with decreasing mass. The lack of mass segregation among low mass stars is theoretically expected due to their evaporation. While the sinking of the high mass stars occurs over as little as one relaxation time, and may even be primordial in very young clusters such as the Trapezium (Hillenbrand & Hartmann 1998; Bonnell & Davies 1998), segregation among average and below average mass stars takes much longer and results in similar escape rates for those groups even after several relaxation times (Spitzer & Shull 1975; Wielen 1975). Thus, the character of the mass function plays a role in the degree of energy equipartion in a cluster by determining which mass groups are average or less. I discuss the Pleiades mass function further in §6.4. Additionally, the Galactic tidal field facilitates evaporation by imposing an upper limit to the velocity distribution (Mathieu 1985). The latter could in principle be tested by searching for evaporated Pleiads using high precision radial velocities or astrometry along the expected preferred directions of escape, perhaps confined to a small angle with respect to the Galactic plane (Terlevich 1987; Portegies Zwart 2000). Clearly our understanding of the role (if any) of energy equipartition in the dispersal of open clusters could benefit from further wide-field analysis in open clusters of various dynamical ages.

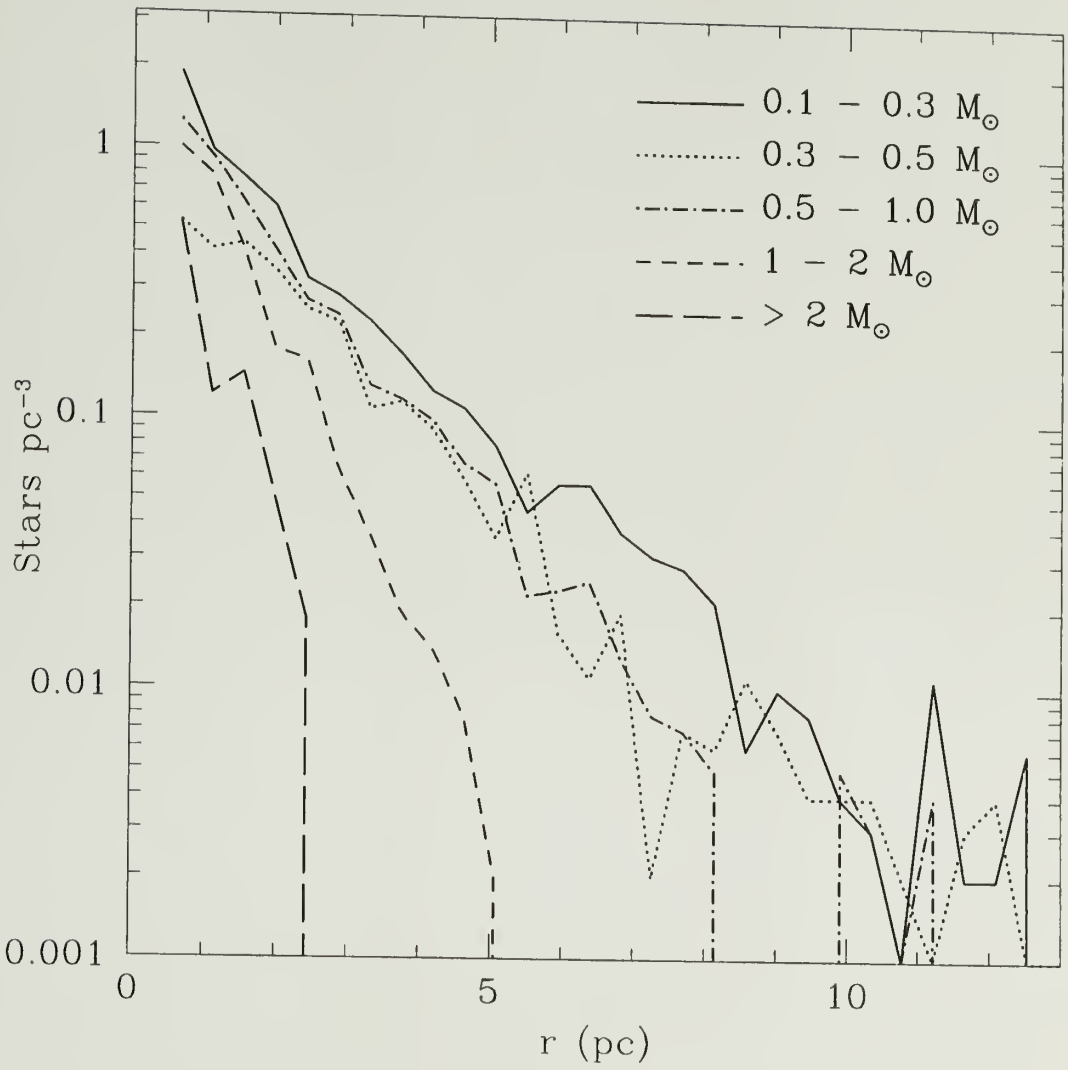

Fig. 6.3.— Approximate spatial density for Pleiades stars of different mass groups derived from a King model. The tidal radius is about 13 pc.

The similar distribution of 1 $M_\odot$ and 0.1 $M_\odot$ stars suggests that brown dwarfs follow the same distribution, and thus a correction for spatially limited brown dwarf surveys such as Bouvier et al. (1998) are legitimate using the distribution of stars. Furthermore, this result indicates that relatively bright stars up to $V \approx 12$ can be used to trace the kinematics of the cluster using upcoming high precision astrometry surveys such as FAME (Horner et al. 1999) or SIM (Unwin 1999) which according to specifications should constrain nearly the entire six-dimensional phase space in nearby clusters such as the Pleiades.

6.4 The Mass Function

The abundance of low mass stars in stellar systems makes them important players in dynamical processes. The character of the mass function (MF) in rich, young clusters such as the Pleiades has important ramifications for the initial mass function in star formation, since most stars are believed to form in clusters (Lada, Strom & Myers 1993). The MF is also a critical ingredient in N body simulations with implications for the internal dynamics of energy equipartition (Inagaki & Saslaw 1985) and expected lifetime of clusters (de la Fuente Marcos 1995). For example, numerical simulations show that the mass function can determine a preferential mass range for escaping stars. In a rich open clusters such as the Pleiades, escape rates for average mass stars are similar to below average mass stars, according to depletion factors found by de la Fuente Marcos (1995). However, Terlevich (1987) using a steep, Salpeter-like mass function in rich clusters finds preferential escape for stars of less than average mass.

6.4.1 Characterizing the mass function

The mass function, expressed as

$$\Psi(m) = \frac{dN}{dm}$$

represents the distribution of mass in terms of the number of stars N in the mass interval $[m, m+dm]$. Table 6.1 shows the distribution of Pleiades masses below 1 $M_\odot$ for stars with $p \geq 0.3$ and radial distance less than 5.5°. These results are plotted in

Table 6.1: Distribution of mass in the Pleiades.

m ($M_\odot$)	N (stars)
0.1 – 0.2	303
0.2 – 0.3	248
0.3 – 0.4	161
0.4 – 0.5	143
0.5 – 0.6	112
0.6 – 0.7	66
0.7 – 0.8	65
0.8 – 0.9	53
0.9 – 1.0	44

Figure 6.4 with error bars from Poisson statistics. The completeness of the sample begins to decrease below $\sim$ 0.15 $M_\odot$. I agree with Hambly et al. (1999) that the Pleiades MF is best fit in $\log dN/dm$ *vs.* $\log m$ space with a log normal (quadratic) function rather than a single exponent power law. The best polynomial fit in the 1 - 0.1 $M_\odot$ region gives

$$\log(N \text{ per } 0.1\ M_\odot \text{ bin}) = -0.93 \pm 0.03(\log m)^2 - 1.86 \pm 0.02 \log m + 1.59 \pm 0.02$$

as delineated in Figure 6.4. According to the results in §5.3.1, the overall field star contamination in this sample is expected to be roughly 10 – 15% (or less for stars above 0.5 $M_\odot$). This amount of field star contamination should have little effect on the coefficients of the fit. The derivative of the form yields the power law index $\alpha = 1.86 \pm 0.06 \log m + 1.86 \pm 0.02$ where $\Psi(m) \propto m^{-\alpha}$. Thus the Pleiades MF appears to be slowly rising below 0.5 $M_\odot$ and relatively flat at 0.1 $M_\odot$. This MF could be considered a lower limit at the faint end due to incompleteness and unresolved binarity.

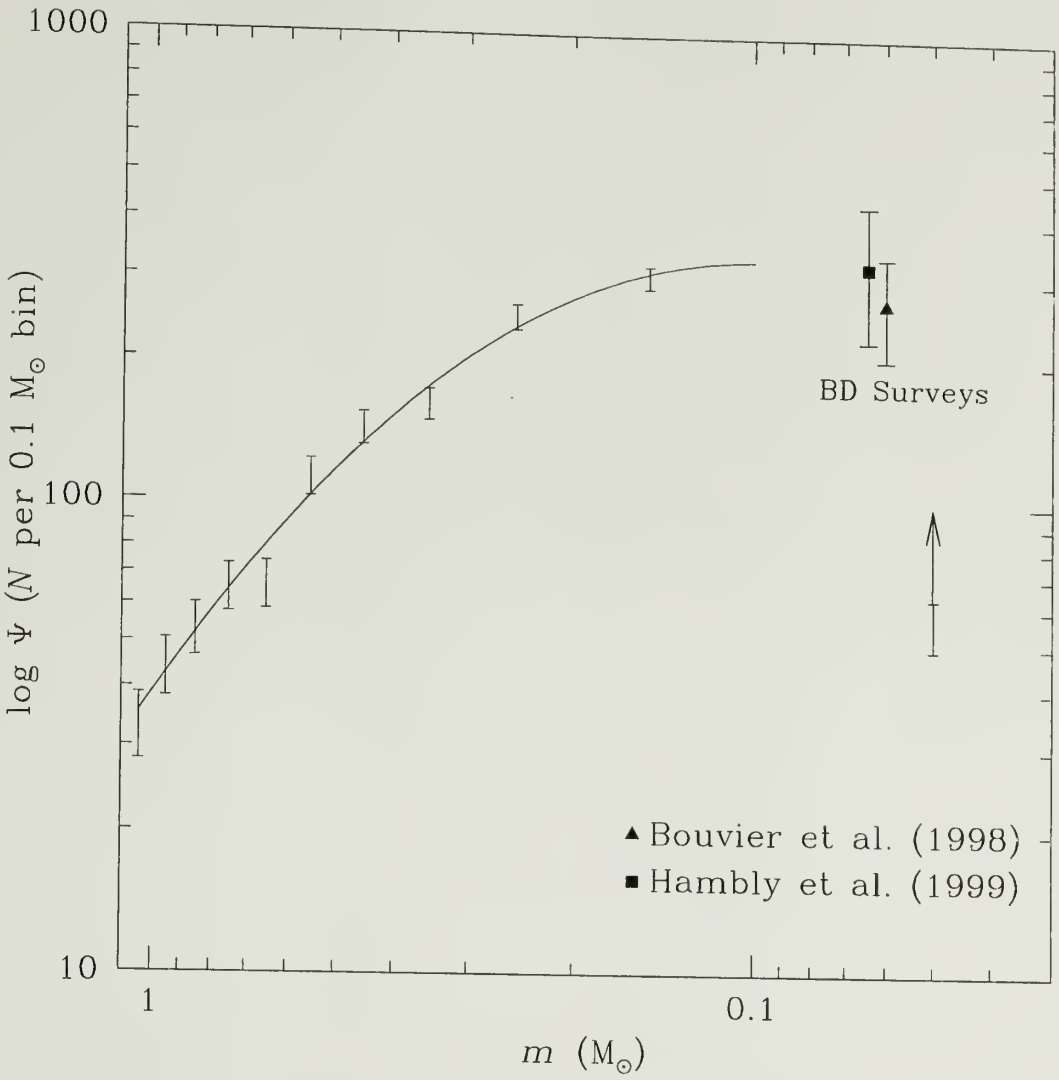

Fig. 6.4.— Pleiades mass function below 1 $M_\odot$. The solid line indicates the best fit polynomial to 0.1 $M_\odot$ where the sample becomes incomplete. Also shown are results from the brown dwarf surveys of Bouvier et al. (1998) (solid triangle) and Hambly et al. (1999) (solid box).

Although less steep in the 0.3 – 0.1 $M_\odot$ region than those inferred by brown dwarf surveys (Bouvier et al. 1998; Hambly et al. 1999; Martín et al. 2000), this MF appears consistent with previous results as shown in Figure 6.4 and suggests a flat or decreasing MF at the hydrogen burning limit. Assuming that this MF continues below 0.04 $M_\odot$, the 303 objects in the lowest 0.1 $M_\odot$ mass bin imply a *crude* lower limit of $\sim$ 200 free-floating objects below the hydrogen burning mass limit at 0.075 $M_\odot$. Additionally, the potentially large numbers of unresolved brown dwarfs companions make a search for low mass Pleiades binaries a useful enterprise for eg. SIRTF observations. Whether or not the mass function begins to rise again below 0.06 $M_\odot$ remains undetermined, but the total brown dwarf mass contribution is likely to be less than 5% of the total Pleiades mass.

The Pleiades MF qualitatively resembles the young mass function in the Orion Nebula Cluster (Hillenbrand & Carpenter 2000) and thus more likely represents initial conditions rather than the depletion of very low mass stars through dynamical evaporation, as in M67 (age = 5 Gyr) (Prata 1971; Montgomery, Marschall & Janes 1993) and possibly the Hyades (age = 600 Myr) (Reid 1992; Reid & Hawley 1999; Gizis, Reid & Monet 1999). While fit with a higher order form, the Pleiades MF also agrees crudely with the field MFs of Reid & Gizis (1997) from nearby star samples which showed a decreasing power law index from above 1 $M_\odot$ to below 0.1 $M_\odot$, although their mass function was fit with a single exponent power law in the 1 – 0.1 $M_\odot$ range. Unresolved binarity may partially account for the more shallow Pleiades MF. Gould, Bahcall & Flynn (1997) using deep photometric *HST* star counts presented a disk MF which appeared to sharply turn over at 0.6 $M_\odot$, in contrast to the Pleiades MF. Several factors may account for the discrepancy between the Pleiades and the disk MF such as large Poisson errors in the field samples, unresolved binarity, Malmquist bias, age effects, and inadequate mass-luminosity conversions (Kroupa, Tout & Gilmore 1993; Méra Chabrier & Baraffe; Reid & Gizis 1997). The MF of the Galactic disk will

better be determined when 2MASS and the Sloan Digital Sky Survey are completed. Overall, these cluster and field MFs agree that (1) a Salpeter index is generally too steep below 1 $M_\odot$, and (2) the mass function is often poorly fit with a single power law over the mass range of dynamical interest, both important results for N body model parameters.

6.4.2 Unresolved Binarity

Many proper motion candidates will be unresolved binaries that will systematically affect measurements of the mass function and total mass in stars. In order to derive a correction factor for unresolved binaries, I performed a simple simulation of the observed masses in a cluster with known primary mass function and frequency and mass distribution of binary companions. The simulation used standard Monte Carlo techniques, such as those described in §2.4, and the same mass-luminosity relations described in §6.2.

A generic log-normal MF (Miller & Scalo 1979) distributed primary masses using the form

$$\frac{dN}{dm} \propto \exp \frac{-(\log m - < \log m >_{\rm peak})^2}{\sigma^2_{\log m}}$$

where $< \log m >_{\rm peak}$ is the gaussian peak of the mass function and $\sigma_{\log m}$ is the gaussian width of the mass function in $\log m$ space. I determined binaries and secondary masses using a binary frequency $f(m)$, and a given distribution of mass ratios $q = m_2/m_1$ where m_1 is the primary mass and m_2 the secondary mass. I divided the hypothetical cluster into mass groups of $m/M_\odot \geq 2$; $1 \leq m/M_\odot < 2$; and $m/M_\odot < 1$.

Realistic values for $f(m)$ are 0.5 for the high and medium mass group and 0.3 for the low mass group (Abt & Levy 1976; Mermilliod et al. 1992). Input parameters for the mass function and q distribution were adopted from Duquennoy & Mayor (1991) and Kroupa, Tout & Gilmore (1990). The primary masses were distributed in N (per unit $\log m$) – $\log m$ space with gaussian peak at $\log m \sim -0.5$ and width of ~ 0.4.

Since they are poorly determined, I varied the parameters of the MF distribution slightly during the simulations, typically by a couple of tenths in central value and width. I used another gaussian distribution for q with peak 0.23 and width 0.42. For stars with mass lower than 1 $M_\odot$, the q distribution was flattened as suggested by data from Mermilliod et al. (1992).

Figure 6.5 shows a typical observed mass function for a given true mass function in $\log dN/dM - \log m$ space for a cluster containing 10000 stars. The observed mass function underestimates the true mass function, particularly at low mass, where the number of stars are underestimated by a factor of 1 – 2 down to 0.1 $M_\odot$. I assumed that all the binaries were unresolved, since 2MASS spatially resolves only the widest binaries ($> 10^5$ AU) at the distance of the Pleiades. The simulations suggest that unresolved binaries at low mass may affect the slope of a mass function α by up to a few tenths below 0.5 $M_\odot$. Repeated simulations determine an overall mass correction factor δ where $M_{true} = (1+\delta)M_{obs}$. Computing the effective apparent magnitude for the binary stars and integrating the true and observed mass functions to about 0.08 $M_\odot$ gave $\delta \sim 0.15$. The simulations were most sensitive to $f(m)$. If $f(m) = 1$ for all masses, δ increases to ~ 0.3. Sliding the peak of the mass function 0.2 $\log m$ units resulted in a change in δ by about 0.02, where a higher peak causes a larger δ. A change the width of the mass function by 0.2 $\log m$ units also resulted in a change in δ by about 0.02, where a wider mass function causes a larger δ. Note that δ was similar for repeated simulations of a cluster of 1000 stars.

6.5 Dynamical Mass

The stellar mass of the Pleiades is best determined by a simple sum of individual members. Candidates in the merged sample with $p \geq 0.3$ within a 5.5° radial distance from the nominal center are the most probable members. Integrating the individual masses to 0.1 $M_\odot$ gives a total mass of 690 $M_\odot$ and a binary-corrected mass of $\sim$

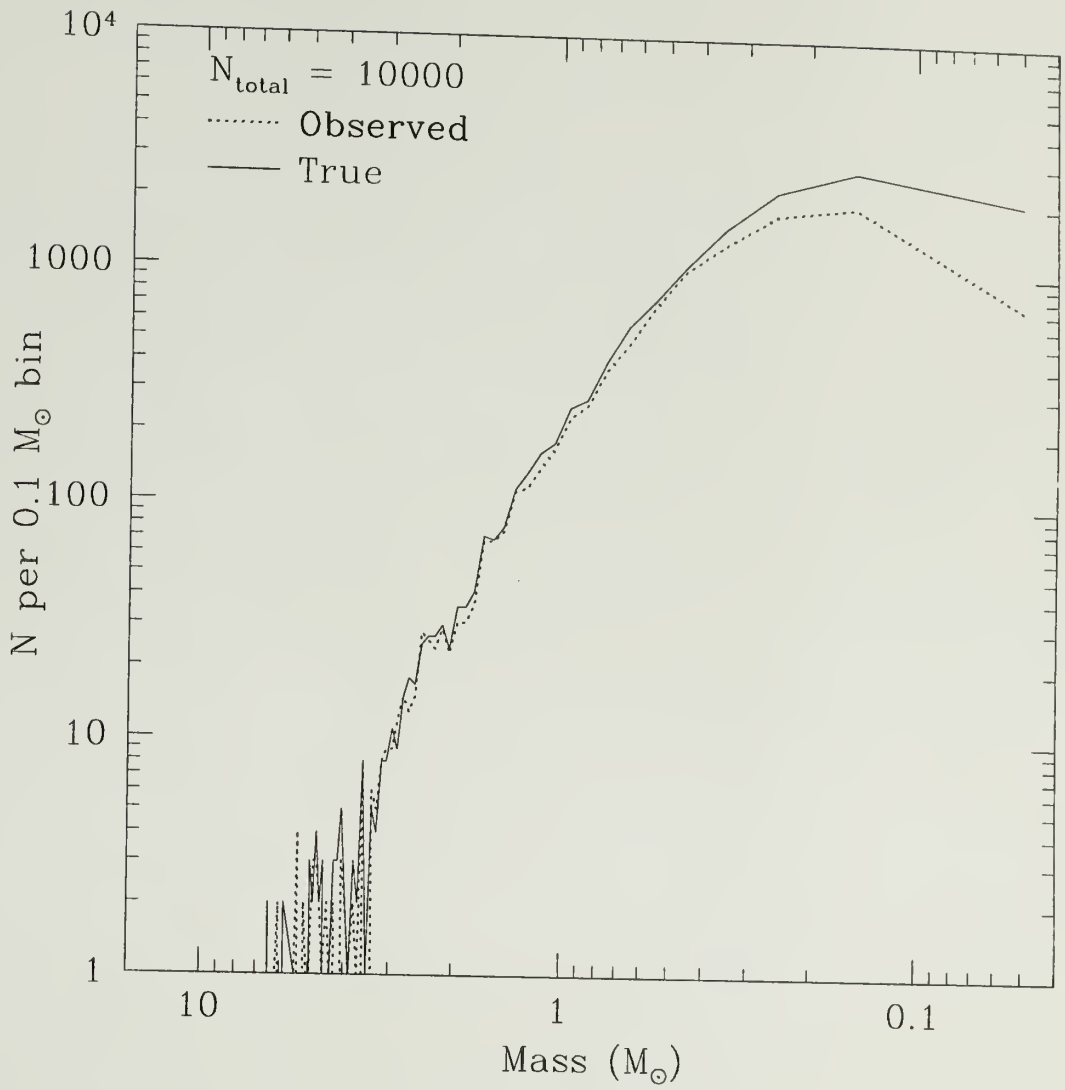

Fig. 6.5.— Simulated mass functions for a cluster of 10000 stars. The observed case was derived from the apparent magnitude of single primaries and effective apparent magnitude of unresolved binary systems.

790 $M_\odot$. This simple sum is replete with systematic and random errors from field contamination, unresolved binaries, Poisson statistics, and completeness. Objects below 0.1 $M_\odot$ are not likely to add more than a few percent to this mass estimate.

For a Galactic cluster in circular orbit, the limiting tidal radius r_{lim} for a test mass along the direction towards or away from the Galactic center can be expressed using a two body approximation as (King 1962)

$$r_{lim} = \left[\frac{GM_c}{4A(A-B)}\right]^{\frac{1}{3}}$$

where M_c is the total cluster mass and A and B are the Oort constants. The values $A = 14.4$ km s^{-1} kpc^{-1} and $B = -12.0$ km s^{-1} kpc^{-1} (Kerr & Lynden-Bell 1986) correspond to a tidal radius of 13.1 pc, a measurement very close to that found by Pinfield, Jameson & Hodgkin (1998) using several different Pleiades catalogs. A projection of this radius is shown in Figure 6.6. Since it overlaps with the confidence interval for the "edge" of the cluster determined from the King profile fit (Figure 6.3), I conclude that the stellar mass composes nearly the entire dynamical mass. Thus no massive population of brown dwarfs or internal dark matter has been detected. Further comparison of r_{lim} given above with the King tidal radius r_t is dangerous as they represent different quantities in this case since the direction of r_{lim} lies along the line of sight.

6.6 Projected Halo Structure

N body models predict an elongation of open clusters in roughly the X-direction and to a slightly lesser extent in the Y-direction, due to heating in the halo by the Galactic tidal field (Terlevich 1987). In canonical N body models that use a static tidal field derived from a circular cluster orbit in the Galactic plane, this flattening yields a nonspherical tidal surface with axial ratios 2:1.4:1 in the X:Y:Z directions respectively (Wielen 1975; Aarseth 1973). Terlevich predicts throughout a cluster

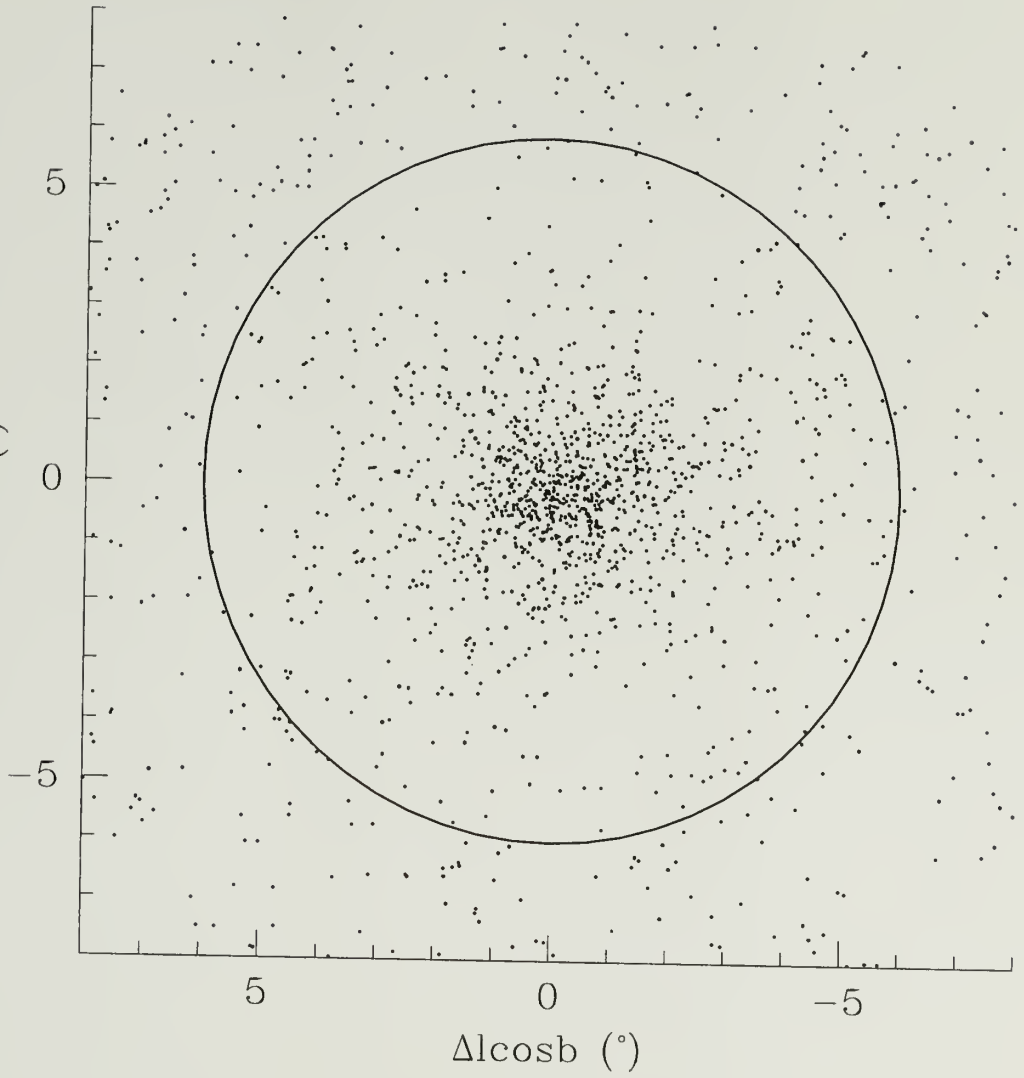

Fig. 6.6.— Spatial distribution in Galactic coordinates for 1 – 0.1 $M_\odot$ stars with $p \geq 0.3$ in the Pleiades field. The circle denotes the projection of the tidal radius derived from a total mass estimate of ~ 790 $M_\odot$.

lifetime a fairly constant number of stars trapped in the halo between 1 and 2 tidal radii in the elongated structure for some period of time before permanently escaping.

At $l = 166°$ and $b = -23$, the projection of the Pleiades onto the sky is most sensitive to structure in the YZ plane. Moment analysis was used to determine the orientation and ellipticity of the spatial distribution. The moments of the distrbution were determined by solving the eigenvalue problem for the covariant matrix of positions S

$$S = \frac{\mathbf{A^T A}}{N-1}$$

where

$$\mathbf{A} = [\mathbf{x} - \bar{x} \quad \mathbf{y} - \bar{y}]$$

$$\mathbf{x} = [(\mathbf{l} - l_{Pleiades}) \cos \mathbf{b}]$$

$$\mathbf{y} = [\mathbf{b} - b_{Pleiades}]$$

N is the total number of stars used in the analysis with Galactic longitude l and latitude b. The ratio of the eigenvalues of S gives axis ratio b_e/a from which I measured the ellipticity $e = (1 - b_e/a)$. The orientation of the eigenvectors yields the directions of maximum variance, ie. the relative angle of the principal components with respect to the longitude of the Pleiades.

To construct S, I used Pleiades candidates with $p \geq 0.3$ and mass 1 - 0.1 $M_\odot$ within various angular distances from the cluster center. Results are tabulated in Table 6.2. While the results agree with those obtained by Raboud & Mermilliod (1998a) at their limiting radius of $\sim 3°$, I detect substantially more elongation at larger radii, at least $e = 0.37$ near the tidal radius. Beyond the tidal radius field stars dilute the ellipticity of the sample. The orientation of the ellipticity is roughly aligned with the projected Y direction, as expected from the static tidal model. If the Pleiades axial ratios are 2:1.4:1, its projected ellipticity should be 0.13 (Raboud

& Mermilliod 1998a). The cluster exhibits more flattening than this value at all radii from just outside the cluster core out to the tidal radius.

I also looked for higher order asymmetry in the halo ellipticity. Figure 6.7 shows star counts for candidates (those with $p \geq 0.3$ within 5.5°) of the center as a function of position angle in the direction Galactic north of Galactic west. Elongation is clearly evident, but not symmetric in the sense that fewer stars appear to lie in the Galactic eastern half. Cluster depth along the line of sight may cause this result, whereby the Galactic southeastern part of the cluster contains stars nearer to the sun. Unfortunately, the precision of our proper motion measurements is not sufficient to discern a convergent point or gradient in proper motion dispersion due to cluster depth. Future space-based astrometric observations would help confirm the nature of this feature.

The Poisson statistics of the background stars place an upper limit of ~ 1.7 stars deg^{-2} that may have escaped the cluster in the projected YZ plane. Unfortunately without individual distance measurements, estimating the escape rate along the X direction where perhaps stars are most likely to escape through the Lagrangian points is difficult. These data do not confirm that the outermost halo stars have become gravitationally unbound. Since the Galactic tidal field is the primary catalyst for the dispersing the cluster, a measurement of the dispersal rates combined with structure and kinematic data in open clusters of various dynamical ages will better test our understanding of the tidal field in open cluster dynamics.

Whether or not other clusters also show flattening that is consistent with the static tidal model is unclear. Substantial flattening has also been found in the Hyades (Oort 1979; Perryman et al. 1998) and Alpha Persei (Prosser 1992). Other clusters, such as Praesepe (Raboud & Mermilliod 1998b) and M67 (Mathieu 1983), have shown little flattening. Better membership surveys are required in most clusters to study any dependence of structure on age or environmental effects, such as collsions with

Table 6.2: Ellipticity e and positional angle ϕ for Pleiades candidates with $p \geq 0.3$ and mass 1 – 0.1 $M_{\odot}$ within radial distance r of the Pleiades nominal center. ϕ is measured Galactic north of Galactic west (counterclockwise in Figure 6.6).

r (°)	e	ϕ (°)
1.0	0.19	-10.0
1.5	0.17	-2.7
2.0	0.13	19.5
2.5	0.17	19.7
3.0	0.20	13.8
3.5	0.24	8.6
4.0	0.27	6.6
4.5	0.32	4.8
5.0	0.37	8.2
5.5	0.32	9.1
6.0	0.29	6.9
6.5	0.27	8.2
7.0	0.14	10.7
7.5	0.08	14.4
8.0	0.07	27.8
8.5	0.07	30.7
9.0	0.08	19.1

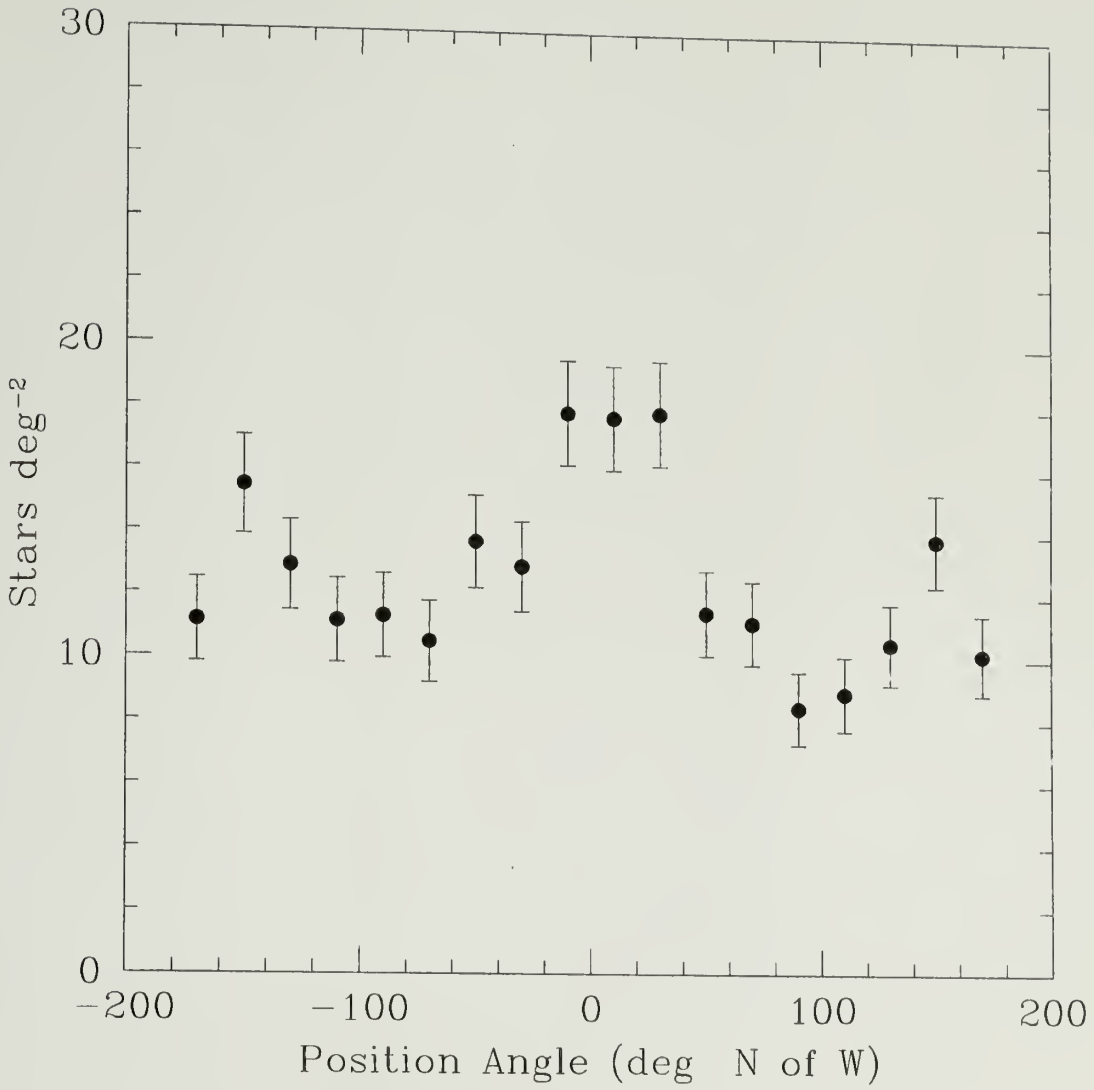

Fig. 6.7.— Star counts out to the tidal radius as a function of position angle around the cluster. The position angle is defined as Galactic north of Galactic west at the longitude of the Pleiades.

interstellar clouds. Comparing the static tidal model results to a more realistic simulation that includes time dependent tidal fields from radial oscillation and vertical disk passage (Murali & Weinberg 1997; Combes, Leon & Maylan 1999) would be a useful exercise to closely examine whether the circular approximation to open cluster orbits is valid enough to warrant our expecting canonical flattening ratios.

6.7 Summary

The results of this chapter are summarized as follows:

1. Pleiades candidates extracted in Chapter 4 with $p > 0.3$ have been merged with source catalogs containing brighter stars and unrecovered HHJ stars. Approximate masses for the overall sample were calculated by interpolating model mass-luminosity relations converted to standard broadband magnitudes and using published empirical mass-magnitude relations for brighter stars.

2. The high mass cluster members are centrally concentrated with respect to low mass members. However, stars below 1 $M_\odot$ share a similar radial distribution indicating that stars in the Pleiades halo have a similar velocity dispersion, a result that generally agrees with theoretical and numerical expectations.

3. The Pleiades mass function rises slowly below 1 $M_\odot$ and appears to become flat at 0.1 $M_\odot$, suggesting a lower limit of ~ 200 brown dwarfs in the cluster. This result is consistent with previous surveys that conclude brown dwarfs contribute little to the dynamical mass. Stars with mass above $\sim 1 - 0.1$ $M_\odot$ dominate the total mass.

4. The total Pleiades mass is ~ 790 $M_\odot$ including a 15% correction for unresolved binaries. The corresponding tidal radius to this mass estimate is 13.1 pc. A massive population of brown dwarfs or dark matter was not detected.

5. The cluster is highly flattened in the YZ plane, substantially more than canonical N body models predict, but with similar orientation. This result confirms that the Galactic tidal field plays the dominant role in open cluster dispersal.

6. Future high precision, space-based astrometry will reveal the internal kinematics as well as any escaping members of the Pleiades, providing a crucial measurement of its dispersal rate.

CHAPTER 7

CONCLUSION

7.1 Summary of Motivation

Open star clusters are fundamentally important astronomical objects for studying the distribution of stellar mass and the dynamics of small stellar systems. Ironically, small number systems are difficult to study theoretically because they rapidly evolve and disperse in the presence of a tidal field. In the past 10 – 20 years, computational power has become sufficient to simulate open clusters by directly integrating the equations of motion. This work has generated specific observable predictions regarding their structure and evolution. In general, mass segregation occurs in open clusters by energy equipartition. Relatively rich clusters form a definitive core-halo structure where the high mass stars dominate the core and the low mass stars occupy the halo on radially elongated orbits. For a circular cluster orbit in the Galactic plane, the effective tidal field elongates halo orbits parallel to the plane. In this case, low mass stars in the halo preferentially escape into the Galactic disk, primarily through the Lagrangian points toward and away from the Galactic center respectively. A model that includes tidal shocking has not yet been simulated for open clusters. Numerical models have in general been able to accurately predict the lifetimes of open clusters. However, the actual dynamics of cluster dispersal into the Galactic disk has not been observationally tested in useful detail.

Observations during the past 20 years have generally lagged the pace of numerical simulations of open clusters. Faint, low mass stars trace the structure of and mass in star clusters. Nearby clusters offer a chance to detect these stars and thereby perform

a detailed study of their dynamics. Nearby clusters are extended over large regions of sky and superimposed on a rich field of background stars. Wide field observations providing uniform photometry and proper motions are required to detect cluster stars and distinguish them from field stars. Modern digital sky surveys have become the best tool for open cluster study and present an opportunity to test theoretical and numerical models of small stellar systems.

The goal of this work was to exploit sky survey data from 2MASS and POSS to perform pioneering measurements of the structure and mass of a key open cluster, the Pleiades, over a spatial area an order of magnitude larger than any previous, faint study in the Pleiades. Specifically, the goals of this work included mapping the distribution of low mass stars in the Pleiades, both statistically and spatially, to study the extent of mass segregation and characterize the mass function to determine the dynamical importance of objects at very low mass. A precise mass estimate yields a reliable measurement of the tidal radius and thus the location of escaping or nearly escaping stars. A major goal was to determine the degree of tidal flattening in the cluster, which can for the first time test the static tidal model against a real cluster.

7.2 Summary of Results

A study of the structure of the Pleiades requires a reliable sample of low mass cluster members. This work used a reliable statistical technique to identify a sample of probable cluster members required to fulfill the scientific goals of this thesis. Pleiades stars exhibit a proper motion distinguishable from field stars. The distribution of proper motions for the cluster and the field was modelled with appropriate function and a proper motion membership probability was computed for each star. The distribution function parameters were determined with a maximum likelihood technique. The method was demonstrated to be feasible using artificial cluster and field data generated from Monte Carlo simulations on pre-determined distribution

functions representing a realistic cluster. This method fails, however, if the concentration of field stars becomes too high or if the astrometric dispersion due to faintness becomes too large for the cluster distribution to resemble a functional form. For the case of the Pleiades, the latter is more prominent.

2MASS data and proper motions from POSS I and POSS II detections were correlated to produce a database of positions, $R_E R_F JHK_s$ magnitudes, and proper motions in a 10° radius around the nominal center of the Pleiades. Initial color selection eliminated a large number of obvious field stars. The distribution of cluster and field stars were fit and membership probabilities calculated. Roughly 1200 candidates are probable Pleiades members based on their high proper motion membership probability and location with respect the cluster. Several hundred are newly detected candidates in both new and previously surveyed regions. The faintest stars in the sample have unreliable membership probabilities due to large uncertainties in their astrometry. The proper motion sample is contaminated with field stars.

In order estimate the field star contamination in the Pleiades extraction, I performed a spectroscopic study using multi-object spectra in the 6000 -- 9000 Å wavelength region for 528 cluster candidates and 121 field stars. The primary goal of the spectroscopic work was to reject stars that have an absence of Hα 6563 Å emission as Pleiades members. The contamination was estimated at 13% for candidates within a tidal radius and brighter than $K_s = 14$. The contamination is worse for stars fainter than $K_s = 14$. Nearly all candidates beyond 6° are expected to be field stars. Additional spectroscopic results show no increase in Hα strength for stars fainter than $J = 13.2$. This trend continues into the brown dwarf regime, suggesting additional factors in very low mass objects may affect chromospheric activity attributed to the solar dynamo model. Two confirmed flare stars were identified on the basis of strong Hα emission and several atomic emission lines usually found absent or in absorption in M dwarfs. Spectral types were determined using molecular absorption band depths.

The list of low mass Pleiades candidates was merged with catalogs of brighter Pleiades members. Masses were determined for probable Pleiads using appropriate mass-luminosity relations and apparent magnitudes. The radial distribution for stars in various mass groups show that the massive stars are found in a core of less than 5 pc, while the low mass stars are distributed out to 13 pc. All low mass stars show similar radial distribution indicating that they have similar velocity dispersion. Objects below 0.1 $M_{\odot}$ probably contribute little to the dynamical mass. The Pleiades contains a mass $\sim$ 790 $M_{\odot}$ with no velocity or structural signature of dark matter. The halo in projection shows an ellipticity of at least 0.3 – 0.4 in YZ plane. This flattening is substantially larger than expected by the standard N body models incorporating a static tidal field, although it does lie parallel to the Galactic plane as predicted. An upper limit was placed of 1.7 stars deg^{-2} outside the tidal radius in the YZ plane.

7.3 Future Prospects

7.3.1 Ground-based work

This thesis represents the beginning of what will likely be a rapid increase in our understanding of open cluster dynamics due to the explosion of digital sky survey data. This work has demonstrated the feasibility of studying the dynamical properties of suitable open clusters using the current generation of sky surveys. The data and techniques exist to extend this work to other clusters of various dynamical ages, such as the Hyades (600 Myr), Praesepe (600 Myr), and Alpha Persei (90 Myr), to further test N body simulations and study open cluster evolution. The Hyades cluster, the nearest stellar cluster to the Sun, exhibits the largest proper motion, but is diffuse and would be extremely difficult to study over its diameter of well over 10°. Alpha Persei exhibits a detectable proper motion but lies near the Galactic plane, where field star contamination makes a proper motion search more difficult than in the Pleiades.

Praesepe is likely to be the most accessible cluster due to its similar galactic latitude to the Pleiades. I have selected Praesepe for a followup study to Pleiades since Praesepe is older than the Pleiades and comparable in proper motion and field star density. Within a 6° radius around the cluster, several hundred Praesepe candidates have been identified in similar fashion to the Pleiades search presented in Chapter 4. The spatial distribution for these candidates is shown in Figure 7.1.

Southern hemisphere clusters are now accessible for proper motion study using the First USNO CCD Astrograph Catalog (Zacharias, Rafferty & Zacharias 2000). For example, IC 2391 and IC2602 lie along the direction of Galactic rotation and offer a unique opportunity to study tidal elongation in the direction of the Galactic center.

7.3.2 Space-based work

Upcoming space astrometry missions will make the most promising contribution to open cluster research. The Full Sky Astrometric Mapping Explorer (FAME), an all sky astrometric survey in optical bands scheduled for launch in 2004, will reach a precision of 50 – 500 μas with sensitivity to $V = 15$ (Horner et al. 1999). This should reach low mass stars in clusters such as the Pleiades. An important result of this dissertation is that the velocity distribution and structure of the Pleiades can be studied with 1 – 0.5 $M_{\odot}$ stars which are relatively bright, and within the sensitivity range of FAME. Not only will FAME produce better membership determinations, it will also measure the transverse velocity dispersion and distances in clusters, constraining nearly the entire phase space. Thus FAME will detect velocity anisotropies and the three-dimensional structure of nearby cluster halos. The Space Interferometry Mission (SIM) will reach a precision of 4 μas to a sensitivity of $V = 20$ (Unwin 1999) and will provide parallax and proper motion data over Galactic kpc scales. Since SIM is not a full sky survey, it will likely determine distances and velocities of stars in a few key clusters. SIM is scheduled for launch in 2005.

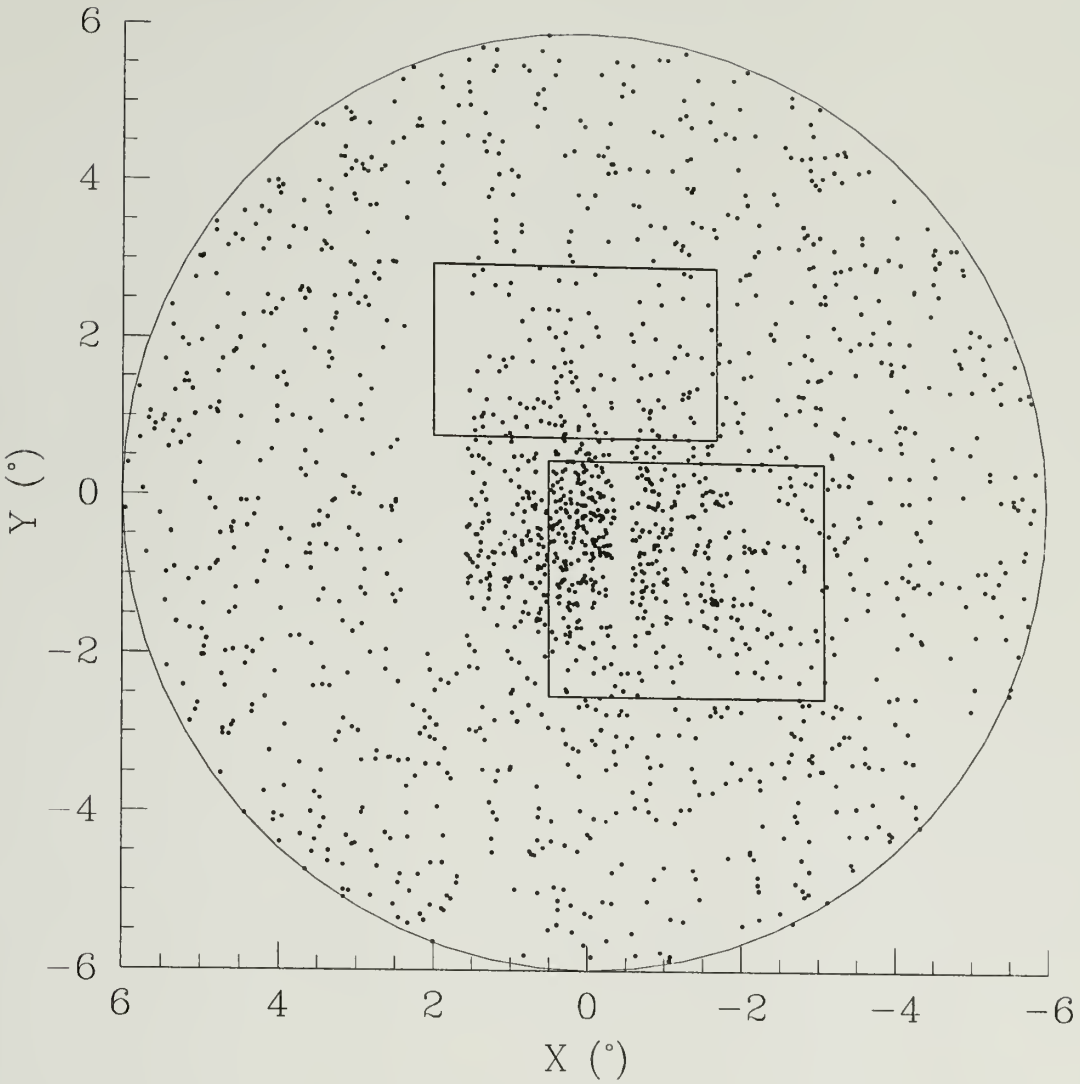

Fig. 7.1.— Spatial distribution of current Praesepe candidates selected from photometric and proper motion properties. The boxed regions outline the region covered by the last faint, proper motion search in Praesepe (Hambly et al. 1995). Blank strips occur where 2MASS data is not yet accessible.

BIBLIOGRAPHY

Aarseth, S. J. 1973, Vistas Astr., 15, 13

Aarseth, S. J. 1999, PASP, 765, 1333

Abt, H. A. & Levy, S. G. 1976, ApJS, 30, 273

Allen, C. W. *Astrophysical Quantities*, London: Athlone Press, 1973

Allen, L. E. & Strom, K. M. 1995, AJ, 109, 1379

Baraffe, I., Chabrier, G., Allard, F. and Hauschildt, P. H. 1997, A&A, 327, 1054

Baraffe, I., Chabrier, G., Allard, F. and Hauschildt, P. H. 1998, A&A, 337, 403

Barbaro, G., Dallaporta, N. & Fabris, G. 1969, Ap&SS, 3, 123

Barden, S. C., Armandroff, T., Muller, G., Rudeen, A. C., Lewis, J., & Groves, L. 1994, SPIE, 2476, 56

Becker, W. & Fenkhart, R. 1971, A&AS, 4, 241

Belikov, A. N., Hirte, S., Meusinger, H., Piskunov, A. E., & Schilbach, E. 1998, A&A, 332, 575

Bessell, M. S. & Brett, J. M. 1988, PASP, 100, 1134

Binney, M. & Tremaine, S. 1987, *Galactic Dynamics*, Princeton: Princeton University Press

Birney, D. S. 1991, *Observational Astronomy*, Cambridge: Cambridge University Press, p. 74

Bonnell, I. A. & Davies, M. B. 1998, MNRAS, 295, 691

Bouvier, J., Stauffer, J. R., Martín, E. L., Barrado y Navascués, Wallace, B., & Bejar, V. J. S. 1998, A&A, 336, 490

Budding, E. 1993, *An Introduction to Astronomical Photometry*, Cambridge: Cambridge University Press

Burgasser, A. J., Kirkpatrick, J. D., Brown, M. E., Reid, I. N., Gizis, J. E., Dahn, C. C., Monet, D. G., Beichman, C. A., Liebert, J., Cutri, R. M. & Skrutskie, M. F. 1999, ApJ, 522L, 65

Burrows, A., Marley, M., Hubbard, W. B., Lunine, J. I., Guillot, T., Saumon, D., Freedman, R., Sudarsky, D., & Sharp, C. 1997, ApJ, 491, 856

Burrows, A & Sharp, C. M. 1999, ApJ, 512, 843

Chabrier, G. & Baraffe, I. 1997, A&A, 327, 1039

Combes, F., Leon, S. & Maylan, G. 1999, A&A, 352, 149

de la Fuente Marcos, R. 1995, A&A, 301, 407

de la Fuente Marcos, R. 1996a, A&A, 308, 141

de la Fuente Marcos, R. 1996b, A&A, 314, 453

Duquennoy, A. & Mayor, M. 1991, A&A, 248, 485

Festin, L. 1998, A&A, 333, 497

Gizis, J. E., Reid, I. N. & Monet, D. G. 1999, AJ, 118, 997

Gould, A., Bahcall, J. N. & Flynn, C. 1997, ApJ, 482, 913

Hambly, N. C., Hawkins, M. R. S., and Jameson, R. F. 1993, A&AS, 100, 607

Hambly, N. C., Steele, I. A., Hawkins, M. R. S., and Jameson, R. F. 1995, MNRAS, 273, 505

Hambly, N. C., Hodgkin, S. T., Cossburn, M. R. & Jameson, R. F. 1999, MNRAS, 303, 835

Hamilton, D. & Stauffer, J. R. 1993, AJ, 105, 1855

Haro, G., Chavira, E., & Gonzalez, G. 1982, Boll. del Instituto de Tonantzintla, 3, 1

Hawley, S. 1993, PASP, 105, 955

Hawley, S., Gizis, J., & Reid, I. N. 1996, AJ, 112, 2799

Hawley, S. 1999, *From Giant Planets to Cool Stars*, ASP Conference Series, in press

Henry, T. J. & McCarthy, D. W. 1993, AJ, 106, 773

Hertzsprung, E. 1947, Annu. Leiden Obs, 19, Part 1A

Hillenbrand, L. A. 1997, AJ, 113, 1733

Hillenbrand, L. A. & Hartmann, L. W. 1998, ApJ, 492, 540

Hillenbrand, L. A. & Carpenter, J. M. 2000, ApJ, in press (astro-ph 0003293)

Hodgkin, S. T., Jameson, R. F. & Steele, I. A. 1995, MNRAS, 274, 869

Horner, S. D., Germain, M. E., Greene, T. P., Harris, F. H., Harris, H. C., Johnson, M. S., Johnston, K. J., Monet, D. G., Murison, M. A., Phillips, J. D., Reasenberg, R. D., Seidelmann, P. K., Urban, S. E. & Vassar, R. H. 1999, BAAS, 195, # 88.01

Hut, P. & Bahcall, J. N. 1983, ApJ, 268, 319

Inagaki, S. & Saslaw, W. C. 1985, ApJ, 292, 339

Jones, B. F. 1970, AJ, 75, 563

Jones, B. F. 1971, AJ, 76, 470

Jones, B. F. 1981, AJ, 86, 290

Jones, B. & Stauffer, J. 1991, AJ, 102, 1080

Kerr, F. J. & Lynden-Bell, D. 1986, MNRAS, 221, 1023

King, I. 1962, AJ, 67, 471

King, I. 1967, Lect. in Appl. Math., 9, 2, 116

King, I. 1980, in ed. Hesser, J., Star Clusters, Dordrecht, Holland, p. 139

Kirkpatrick, J. D., Henry, T. J. & McCarthy, D. W. 1991, ApJS, 77, 417

Kirkpatrick, J. D., Reid, I. N., Liebert, J., Cutri, R. M., Nelson, B., Beichman, C. A., Dahn, C. C., Monet, D. G., Gizis, J. E. & Skrutskie, M. F. 1999, ApJ, 519, 802

Kroupa, P., Tout, C. A. & Gilmore, G. 1990, MNRAS, 244, 76

Kroupa, P., Tout, C. A. & Gilmore, G. 1993, MNRAS, 262, 545

Kroupa, P. 1995, MNRAS, 277, 1522

Lada, E. A., Strom, K. M. & Myers, P. C. 1993, in Levy, E. & Lunine, J. eds. Protostars and Planets III, University of Arizona, p. 245

van Leeuwen, F. 1983, Ph.D. dissertation, Leiden University

Liebert, J., Kirkpatrick, J. D., Reid, I. N. & Fisher, M. D. 1999, ApJ, 519, 345L

Lindoff, U. 1968, Ark. Astr., 5, 1

Lyngä, G. 1987, Catalogue of Open Cluster Data (5th Ed.), Lund Observatory

Martín, E., Brandner, W., Bouvier, J., Luhman, K. L., Stauffer, J. & Basri, G. 2000, ApJ, in press (astro-ph/0004174)

Mathieu, R. D. 1983, Ph.D. Dissertation, University of California Berkeley

Mathieu, R. D. 1984, ApJ, 284, 643

Mathieu, R. D. 1985, in Goodman, J. & Hut, P. eds., Dynamics of Star Clusters, p. 427

Méra, D., Chabrier, G. & Baraffe, I. 1996, ApJ, 459, L87

Mermilliod, J.-C., Rosvick, J. M., Duquennoy, A. & Mayor, M. 1992, A&A, 265, 513

Mihalas, D. & Binney, J. 1981, *Galactic Astronomy.* New York: W. H. Freeman and Company

Miller, G. & Scalo, J. 1979, ApJS, 41, 513

Monet, D. & Corbin, T. 1997, The New International Celestial Reference Frame, 23rd meeting of the IAU, Kyoto, Japan

Monet, D. 1998, Astrophysics and Algorithms: a DIMACS Workshop on Massive Astronomical Data Sets

Montgomery, K. A., Marschall, L. A. & Janes, K. A. 1993, AJ, 106, 181

Murali, C. & Weinberg, M. D. 1997, MNRAS, 291, 717

Oort, J. H. 1979, 78, 312

Oppenheimer, B. R., Kulkarni S. R. & Stauffer, J. R. 1999, in eds. Mannings, V., Boss, A., and Russell, S., Protostars and Planets IV, Tucson: University of Arizona Press

Pels, G., Oort, J. H. & Pels-Kluyver, H. A. 1975, A&A, 43, 243

Perryman, M. A. C., Brown, A. G. A., Lebreton, Y., Gomez, A., Turon, C., Cayrel de Strobel, G.,Mermilliod, J. C., Robichon, N., Kovalesky, J., Crifo, F. 1998, A&A, 331, 81

Pinfield, D. J., Jameson, R. F. & Hodgkin, S. T. 1998, MNRAS, 299, 955

Portegies Zwart, S. F. 2000, MNRAS, in press (astro-ph 0005248)

Prata, S. W. 1971, AJ, 76, 1017

Press, W. H., Teukolsky, S. A., Vetterling, W. T. & Flannery, B. P. 1992, *Numerical Recipes*, Cambridge: Cambridge University Press, p. 118

Prosser, C., Stauffer, J. & Kraft, P. 1991, AJ, 101, 1361

Prosser, C. F. 1992, AJ, 103, 488

Raboud, D. & Mermilliod, J.-C. 1998a, A&A, 329, 101

Raboud, D. & Mermilliod, J.-C. 1998b, A&A, 333, 897

Reid, I. N., Brewer, C., Brucato, R. J., McKinley, W. R., Maury, A., Mendenhall, D., Mould, J. R., Mueller, J., Neugebauer, G., Phinney, J., Sargent, W. L. W., Schombert, J., & Thicksten, R. 1991, PASP, 103, 661

Reid, I. N. 1992, MNRAS, 257, 257

Reid, I. N. & Gizis, J. E. 1997, AJ, 113, 2246

Reid, I. N. & Hawley, S. L. 1999, AJ, 117, 343

Robichon, N., Arenou, F., Mermilliod, J.-C. & Turon, C., A&A, 345, 471

Salpeter, E. E. 1955, ApJ, 121, 161

Sanders, W. L. 1971, A&A, 14, 226

Saumon, D., Bergeron, P., Lunine, J. I., Hubbard, W. B. & Burrows, A. 1994, ApJ, 424, 333

Schilbach, E., Robichon, N., Souchay J., and Guibert, J. 1995, A&A, 299, 696

Shu, F. H. 1977, ApJ, 214, 488

Shu, F. H., Adams, F. C. & Lizano, S. 1987, ARA&A, 25, 23

Spitzer, L. & Hart, M. H. 1971, ApJ, 164, 399

Spitzer, L. & Thuan, T. X. 1972, ApJ, 175, 31

Spitzer, L. & Chevalier, R. A. 1973, ApJ, 183, 565

Spitzer, L. & Shull, J. M. 1975, ApJ, 201, 773

Stauffer, J., Hamilton, D., Probst, R., Rieke, G., & Mateo, M. 1989, ApJ, 344, L21

Stauffer, J., Klemola, A., Prosser, C., & Probst, R. 1991, AJ, 101, 980

Stauffer, J., Hamilton, D., & Probst, R. 1994, AJ, 108, 155

Stauffer, J. R., Liebert, J. & Giampapa, M. 1995, AJ, 109, 298

Stauffer, J. R., Schultz, G., & Kirkpatrick, J. D. 1998, ApJ, 499L, 199

Steele, I. A. & Jameson, R. F. 1995, MNRAS, 272, 630

Tereby, S., Shu, F. H. & Cassen, P. 1984, ApJ, 286, 529

Terlevich, E. 1987, MNRAS, 224, 193

Tinney, C. G. & Reid, I. N. 1998, MNRAS, 301, 1031

Trumpler, R. J. 1921, Lick Obs. Bull., 333, 110

Unwin, S. C. 1999, BAAS, 195, # 46.02

Weilen, R. 1971, A&A, 13, 309

Weilen, R. 1975, in ed. Hayli, Dynamics of Stellar Systems, p. 119

Zacharias, N., Rafferty, T. J. & Zacharias, M. I. 2000, AAS, DDA # 31

Zapatero Osorio, M. R., Rebolo, R., & Martín, E. L. 1997, A&A, 317, 164